Summer 2014

Density Functional Theory Modeling of It-Stacking and Electrophilic Donor-Acceptor Interactions with Application to Therapeutic Targeting of Zinc-Finger Proteins

Patricia Beall Lutz
Old Dominion University

DENSITY FUNCTIONAL THEORY MODELING OF π-STACKING AND ELECTROPHILIC DONOR-ACCEPTOR INTERACTIONS WITH APPLICATION TO THERAPEUTIC TARGETING OF ZINC-FINGER PROTEINS

by

Patricia Beall Lutz
B.S. Science Education May 1977, Virginia Polytechnic Institute and State University

A Dissertation Submitted to the Faculty of
Old Dominion University in Partial Fulfillment of the
Requirements for the Degree of

DOCTOR OF PHILOSOPHY

CHEMISTRY

OLD DOMINION UNIVERSITY
August 2014

Approved by:

Craig A. Bayse (Director)

Patricia Pleban (Member)

Bala Ramjee (Member)

Marie Melzer (Member)

Lepsha Vuskovic (Member)

ABSTRACT

DENSITY FUNCTIONAL THEORY MODELING OF π-STACKING AND ELECTROPHILIC DONOR-ACCEPTOR INTERACTIONS WITH APPLICATION TO THERAPEUTIC TARGETING OF ZINC-FINGER PROTEINS

Patricia Beall Lutz
Old Dominion University, 2014
Director: Dr. Craig A. Bayse

Several viruses, including viruses that cause cancer, contain conserved zinc finger (ZF) proteins that are essential for viral reproduction, making them attractive drug targets for cancer and viral treatment. ZFs are small protein domains that have Zn^{2+} tetrahedrally coordinated to at least 2 Cys and His. They form three classes of ZFs depending on the amino acid ligands, CCHH, CCCH, and CCCC. Zn^{2+} is stable towards redox reactions; however, the Cys thiolates are redox active. Oxidation of the Cys thiolates release Zn^{2+}, and the ZF loses its tertiary structure and can no longer bind DNA or RNA. Understanding the interaction of reducible sulfur and selenium compounds (rS/Se) with ZF proteins is valuable for explaining the beneficial chemoprevention, viruscidal activity and toxicity of these compounds and can guide the production of new chemopreventives and anti-viral agents. DFT was used to investigate the interaction of small r-S/Se compounds with models of three classes of ZF proteins. Density functional theory (DFT) calculations show that increasing the number of thiolate ligands coordinated to Zn^{2+} leads to stronger interactions with r-Se compounds due to the increase in the energy of the ZF HOMO. A high correlation was found between the LUMO energy of the r-S/Se compound the interaction energy, suggesting that the LUMO energy of a potential drug could be used to test its ability to oxidize a ZF protein.

The nucleocapsid protein (NCp7) from the HIV-1 virus is an attractive drug target. Electrophilic compounds can inhibit NCp7 functions, but their lack of specificity has impeded their use as antiviral drugs. Because W37 of NCp7 π-stacks to Gua in the NCp7-DNA binding site, compounds that bind with a higher affinity will be able to specifically inhibit NCp7 binding to DNA. Methylation or metalation is proposed to increase the

stacking interaction between the positively charged base and W37 by lowering the LUMO of the base and bring it closer in energy to the HOMO of W. Small models of methylated and metalated Gua π-stacked to W were investigated with DFT. The interaction energies correlated with experimental K_π values, and with the LUMO energy of the modified MeGua, suggesting that LUMO energies could give a quick estimation of π-stacking energy.

For a more complete understanding of π-stacking interactions, a DFT study of dimers of small aromatic compounds was undertaken. Although dispersion and electrostatics are known to stabilize π-stacking interactions, the preference for parallel displaced (PD) and or twisted (TW) conformations over sandwich (S) geometries in these dimers is not well understood. Orbital analysis showed that PD or TW structures convert one or more π-type dimer MO with out-of-phase or antibonding inter-ring character at the S to in-phase or binding at the PD/TW structure. The change in dimer MO character was described by stack bond order (SBO), a term introduced as an analogy to the bond order in molecular orbital theory. The SBO of a S structure is zero; parallel displacement or twisting result in a non-zero SBO and overall bonding character. The total inter-ring Wiberg bond indices or total Löwdin bond order, which quantify orbital interactions, is maximized at the optimal PD and or TW geometry. As a follow-up study, we investigated using SBO to formulate general principles that could be used to rationalize the preferred geometries of a broad range of π-stacking interactions. The ability to qualitatively predict the preferred geometry of π-stacked dimers using SBO would be beneficial to researchers that study the many systems that involve π-stacking interactions.

This dissertation is dedicated to my parents, Kenneth and Elizabeth Beall

ACKNOWLEDGMENTS

I would like to thank my parents for giving me roots and wings. They gave me a solid Christian home, and encouraged me to follow my dreams. My mother was my inspiration to return to school later in life, as she went back to school to get her Master's degree when she was my age. I would like to thank my husband, George, for all his support. I pray that my ceiling will be my children's floor. My children, Sarah, Tony, Tiffany, Kenny, Hannah and Rachel and my grandchildren, are the joy of my life and I would like to thank them for all their faith in me and for their encouragement.

I would like to thank the Chemistry department at Old Dominion University for giving me the opportunity to earn my degree. The staff at ODU is exceptional and I would like to thank, Alicia, Janice, Tammy and Valerie for all their kindness and friendship. The students that I worked with in Dr. Bayse lab, Sonia, Lenora, and Ashley, will be missed. I wish them well in all they do.

I am grateful for the prayers of my friends, Jennie, Carol and Dolores. Their prayers helped me to carry on when I was discouraged. I want to give glory to God and His son Jesus Christ, who is the solid rock upon whom I stand.

I am thankful to my committee members, Dr. Patricia Pleban, Dr. Bala Ramjee, Dr. Marie Melzer, and Dr. Lepsha Vuskovic. I would especially like to thank my advisor Dr. Craig Bayse, for all his guidance throughout this research project.

TABLE OF CONTENTS

Page

LIST OF TABLES

LIST OF FIGURES

CHAPTER 1

INTRODUCTION

Zinc Finger Proteins

Zinc, which is essential for growth and development,[1] is the most common transition metal incorporated into metalloproteins[2] and is the second most abundant in the human body after iron.[3] Zinc has many advantages over other transition metal ions as a cofactor in proteins: (a) Zn^{2+} has a full d shell, and hence no ligand field splitting energy; (b) Zn^{2+} is not redox active; (c) it has borderline hardness, so it can coordinate with nitrogen from histidine, sulfur from cysteine or oxygen from glutamate, aspartate and water;[4] (d) Zn^{2+} is labile and can exchange ligands rapidly.[5] Zinc metalloproteins are classified as either catalytic, with interchangeable water ligands in the coordination sphere, or structural, where only amino acid residues are coordinated to Zn^{2+}.[6] One type of structural zinc proteins, the zinc fingers (ZF), is the largest class of metalloproteins.[7]

The term ZF[8] was first used for the repeating zinc binding motif of transcription factor IIIA (TFIIIA), a protein necessary for the transcription of 5S ribosomal RNA genes isolated from the African clawed toad *Xenopus*.[9] The name ZF came from the proposed finger-like appearance of the individual motifs, due to the folding of the protein around a central Zn^{2+}, to form a DNA-binding domain.[10] Originally the name ZFs referred to DNA binding domains that coordinated Zn^{2+} with two cysteine (C) and two histidine (H) residues.[11] Today, ZF is a more general term that includes not only the classical CCHH, but also CCCH and CCCC ZFs.[12] (ZF can alternatively be classified into eight fold groups.[13]) The Cys ligands transfer negative charge to the Zn^{2+} and keeps Zn^{+2} from binding a 5th ligand through steric repulsions, preventing it from acting as a Lewis acid as in catalytic proteins.[14] The CCCC binding motif is also found in the zinc storage protein metallothionein (MT) that has 20 Cys that bind 7 Zn^{2+}.[15] ZFs make up 3% of the human genome, with 4500 CCHH ZFs from 564 proteins, and only 17 CCCH from 9 proteins.[16]

This dissertation follows the format of Inorganic Chemistry.

Inside the cell, Zn^{2+} is tightly bound to proteins, with only picomolar to nanomolar concentrations of the free ion.[15,17] If the concentration of Zn^{2+} becomes too high, it can obstruct Ca^{2+} dependent processes or interfere with other proteins.[15] Zn^{2+} is released from one protein and transferred to another site is through the redox activity of the Cys ligand.[15] When the Cys ligands are oxidized from the thiolate to the disulfide, Zn^{+2} is released. Reduction back to the thiolate restores binding.[18] The mechanism of Zn^{+2} release and binding is called a redox zinc switch (Scheme 1).[19] The availability of free Zn^{+2} in the cell is increased in an oxidative environment and decreased in under reducing conditions.[20] There are two types of redox zinc switches: (a) redox sensors and (b) redox transducers. Redox sensor release Zn^{+2} to affect the protein function.[20] For example, transcription factor ZFs are no longer able to bind to DNA when Zn^{2+} is released.[21] Redox transducers release Zn^{+2} that can bind to another protein and affect its function, thus acting as an intercellular zinc signal in biochemical signaling pathways.[22-23] For example, MT releases Zn^{2+} through oxidization of the thiolate ligands by the mild cellular oxidant, glutathione disulfide (GSSG), and is believed to be a transducer of redox signals.[20]

Scheme 1. Example of a zinc switch for a CCHH-type ZF. Y represents His.

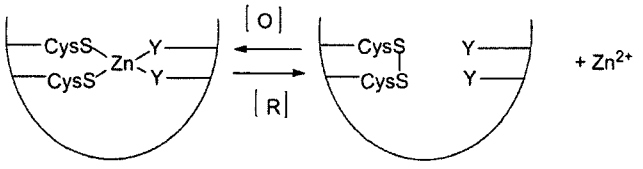

ZF proteins are intrinsically involved in cancer and many viral diseases[24-26], such as HIV-1. As a result there much interest in compounds that react with Zn/S to release Zn^{2+} for therapeutic purposes.[20, 25-27] Releasing Zn^{2+} causes the proteins to unfold and lose their function.[21] Metalloprotein folding varies greatly, for example, in the copper protein plastocyanin, the apo protein structure is very similar that of the holo protein, but apo protein ZF domains exist as random coils with no secondary or tertiary structure[9]. Most antiviral and chemotherapy drugs are non-selective in that they affect all cells, which can

cause unpleasant side effects.[28] Targeting specific ZF proteins is perhaps a more selective way to combat disease. For example, a drug trial found the detergent Nonoxynol-9 to be an ineffective topical vaginal microbicide,[29] leading to a search for drugs with a specific target, such as ZF proteins.[30] Experimental evidence shows that ZF inhibitors are effective topical virucides and safe under *in vivo* conditions.[30] Respiratory syncytial virus[25] (RSV), which strikes children from age 2-8 months, contains M2-1, a CCCH ZF protein that is required for the virus to reproduce.[25] The World Health Organization is searching for a vaccine for RSV. Inactivating RSV with ZF inhibitors could make a safer whole virus vaccine, rather than using formalin, which causes the disease to become more severe.[25]

The two main modes of deactivation we study in this dissertation are release of Zn^{2+} with electrophilic reducible sulfur and selenium compounds and the blocking of the recognition site of the ZF protein with DNA. Reducible sulfur and selenium compounds can release Zn^{2+} from ZF proteins by oxidizing zinc's thiolate ligands, and these compounds have potential use as chemopreventive and anti-viral agents. The reducible sulfur compounds, disulfide-substituted benzamides (DIBAs) are ZF reactive compounds that release Zn^{2+}, and unfold the Zn-CCCH ZF.[31-34] The reducible selenium compound, 1,4-phenylenebis(methylene)selenocyanate (p-XSC) acts as antitumor agent[35-36] by inhibiting DNA binding to the CCHH ZF transcription factors Sp1 and Sp2. Because ZF proteins are integrally involved in viral, cancer, and general body cells, understanding how the sulfur and selenium compounds can deactivate these ZFs is important. The main problem with ZF inhibitors for human therapeutics is the lack of selectively.[37] Chemically modifying ZFs by oxidizing the coordinating Cys residues and releasing Zn^{2+} can also have potential risk to cellular ZFs. For example, the damage to the ZFs in DNA repair proteins like the xeroderma pigmentosum group A (XPA) by oxidizing agents has been identified as a mechanism of carcinogenesis.[38]

The blocking of the interaction site of NCp7 CCCH ZF protein from HIV-1 has been explored as a method for inhibiting ZFs and is perhaps more selective and less likely to interfere with cellular ZFs. The recognition site, which is a π-stacking interaction between MeGua and Trp, is blocked with methylated and metalated MeGua. Like methylation, the

coordination to metal ions enhances the π-stacking interactions between nucleobases and aromatic amino acids.[39] Experiments show that π-stacking interactions to Trp are strengthened when the nucleobase is coordinated to a Pt^{2+} ion.[39-41] The association constants for platinated 9-ethylguanine (9-EtGua) with N-acetyl tryptophan and with the C-terminus of the second ZF (ZF-2) of NCp7 was about twice that of free 9-EtGua.[42] The increased π-stacking interaction of the metalated MeGua should compete with MeGua from DNA in binding to Trp in the NCp7 binding site. The blocking of the interaction site of NCp7 CCCH ZF protein from HIV-1 as a method for inhibiting ZFs is perhaps more selective and less likely to interfere with cellular ZFs.

The investigation of orbital interactions in the electrophilic attack by reducible sulfur and selenium compounds and the enhanced π-stacking interactions between metalated MeGua and Trp is important for understanding how these interactions could be used to target ZF therapeutically. Orbitals interactions can be readily calculated using density functional theory (DFT) to predict interaction strengths before running the actual experiments, allowing for a prescreening of potential drug targets. DFT studies of orbital interactions also give insight into the mechanism of action to assist further rational drug design of therapeutic ZF deactivating compounds.

Theoretical basis for my computational study[43-47]

In this dissertation, density functional theory (DFT) is used to describe and interpret known chemistry and inquire into new chemistry. DFT is a quantum chemical method for the analysis of the structural and electronic properties of molecular systems. The time-independent Schrödinger wave equation developed in 1926 by Erwin Schrödinger is one of the cornerstones of the theory of quantum mechanics. The Schrödinger equation determines the wavefunction Ψ that describes the wavelike properties of subatomic particles. The wavefunction characterizes the motion and all the measureable properties of the particle. $|\Psi^2|$ is the probability density for the electron. The electronic wavefunction describes the most probable positions of the electrons. Operators act upon Ψ and give back the original function called the eigenfunction

multiplied by an eigenvalue which relates to a property of the system.[45] The Schrödinger equation is

$$H\Psi = E\Psi \quad (1)$$

where H is the time-independent non-relativistic Hamiltonian operator, which when acting on the wave function Ψ gives you the energy E of the system.[46] The Hamiltonian operator, in atomic units, contains five terms: the first two are the kinetic energy of the electrons and nucleus, respectively, and the last three are potential energy terms, the attraction between electrons and nuclei, the repulsion between electrons and the repulsion between protons in the nucleus.[43]

$$\mathrm{H} = -\sum_i \frac{1}{2}\nabla_i^2 - \sum_k \frac{1}{2m_k}\nabla_k^2 - \sum_i \sum_k \frac{Z_k}{r_{ik}} + \sum_{i<j} \frac{1}{r_{ij}} + \sum_{k<l} \frac{Z_k Z_l}{r_{lk}} \quad (2)$$

The electronic Hamiltonian uses the Born-Oppenheimer Approximation, which simplifies the solution to the Schrödinger equation by separating the nuclear and electronic motion to calculate the electronic energy as a function of fixed nuclei which as moving more slowly than the electrons.

$$\mathrm{H_{elec}} = -\sum_i \frac{1}{2}\nabla_i^2 - \sum_i \sum_k \frac{Z_k}{r_{ik}} + \sum_{i<j} \frac{1}{r_{ij}} + \sum_{k<l} \frac{Z_k Z_l}{r_{lk}} \quad (3)$$

It is not possible to solve the Schrödinger equation for systems with more than one electron.[47]

The Hartree-Fock (HF) method is used to obtain an approximate solution to the time-independent Schrödinger equation for many electron systems.[47] Constructing electronic wave functions is a difficult many-bodied problem. The largest problem comes from the electron-electron repulsion term. If this term is neglected, the electrons can be treated independently of each other.[48] Hartree's method was to guess a single electron wavefunction ψ, called a molecular orbital, that is made from a linear combination of basis functions ,χ_s, that are often atom-centered Gaussian functions.[47]

$$\psi_j = \sum_{i=1}^{N} c_{si}\chi_s \quad (4)$$

The group of N, χ_s, basis functions is called the basis set. [46] The coefficients c_{si} are the molecular orbital expansion coefficients. When the electrons are treated individually, the Hamiltonian operator is

$$H = \sum_{i=1}^{N} h_i \tag{5}$$

where N is the total number of electrons and h_i is the one electron Hamiltonian.

$$h_i = -\frac{1}{2}\Delta_i^2 - \sum_{k=1}^{M} \frac{Z_k}{r_{ik}} + V_i\{j\} \tag{6}$$

$V_i\{j\}$ is the interaction energy of electron i with all of the other electrons in orbitals j and is equal to,

$$V_i\{j\} = \sum_{j \neq i} \int \frac{\rho_j}{r_{ij}} dr \tag{7}$$

where ρ_j is the electron density probablilty of electron j. The wavefunction can be written as a product of single electron wavefunctions called a Hartree-product wavefunction.

$$\Psi_{HP} = \psi_1 \psi_2 \psi_3 \dots \psi_N \tag{8}$$

The Hartree wavefunctions are spatial orbitals and do not take into account electron spin and are not antisymmetric functions of the electron coordinates. The Pauli Exclusion Principle requires that the wavefunction be antisymmetric with respect to exchange of the particles. The Hartree-Fock approximation represents the antisymmetric wave function with a single Slater determinant. The wavefunctions are products of spin orbitals, which contain a spatial orbital and a spin function α and β, which have only one eigenvalue +1/2 or -1/2 respectively.

$$\Psi = \frac{1}{\sqrt{(2n)!}} \begin{vmatrix} \psi_1(1)\alpha(1) & \psi_1(1)\beta(1) & \psi_2(1)\alpha(1) & \psi_2(1)\beta(1) & \dots & \psi_n(1)\beta(1) \\ \psi_1(2)\alpha(2) & \psi_1(2)\beta(2) & \psi_2(2)\alpha(2) & \psi_2(2)\beta(2) & \dots & \psi_n(2)\beta(2) \\ \vdots & \vdots & \vdots & \vdots & \ddots & \vdots \\ \psi_1(2n)\alpha(2n) & \psi_1(2n)\beta(2n) & \psi_2(2n)\alpha(2n) & \psi_2(2n)\beta(2n) & \dots & \psi_n(2n)\beta(2n) \end{vmatrix} \tag{9}$$

The Slater determinant for the entire wavefunction Ψ has 2n rows for the 2n electrons and 2n columns for the 2n spin orbitals. The $\frac{1}{\sqrt{(2n)!}}$ factor normalizes the function so that $|\Psi|^2$ integrated over all space =1.

Quantum theory does not predict the result of individual measurements, but only their statistical means called the expectation value. The expectation value of the Hamiltonian is the variational energy. The variational theorem states that when a guess wave function is placed in Schrödinger's equation the results will always be higher than the true energy

of the system. The coefficients that give the lowest energy are considered a better approximation to the true wave function. The coefficients c_i are found by minimizing the energy.[46]

$$E = \frac{\int \Psi^* \hat{H} \Psi d\tau}{\int \Psi^* \Psi d\tau} = \frac{\int (\sum_i c_i \chi_i) H (\sum_j c_j \chi_j) dr}{\int (\sum_i c_i \chi_i)(\sum_j c_j \chi_j) dr} = \frac{\sum_{ij} c_i c_j H_{ij}}{\sum_{ij} c_i c_j S_{ij}} \quad (10)[46]$$

H_{ij} is the resonance integral and S_{ij} is the overlap integral. The functions are assumed orthonormal. Substituting the electronic Hamiltonian into the Slater determinants gives the following equation.

$$E = 2\sum_{i=1}^{n} H_{ii} + \sum_{i=1}^{n}\sum_{j=1}^{n}(2J_{ij} - K_{ij}) \quad (11)$$

H_{ii} contains the kinetic energy of an electron and the potential energy of the electron to each of the nuclei. J_{ij} is the coulomb integral and K_{ij} is the exchange integral. The orbitals that minimize the energy satisfy the Hartree-Fock equation,

$$\hat{F}(r_1)\psi_i(r_1) = \varepsilon\psi_i(r_i) \quad (12)$$

where $\hat{F}$ is the Fock operator and the eigenvalue ε is the Hartree-Fock orbital energy. The set of equations for the expansions coefficients is a matrix equation called the Hartree-Fock-Roothaan equation,

$$Fc = \varepsilon Sc \quad (13)$$

where F is the Fock matrix and it defines the average effect of the electron field on each orbital. S, the overlap matrix, is a measure of how much the basis functions interact, or overlap. c is a column vector of the molecular orbital coefficients, and ε is a diagonal matrix containing the orbital energies. Because the Fock matrix depends upon the molecular orbital expansion coefficients, the Hartree-Fock-Roothaan equation is not linear and needs to be solved iteratively using the Self-Consistent Field (SCF) method. This method first makes a guess of the molecular orbitals coefficients that are used to construct the density matrix, and then the Fock matrix. The Hartree-Fock-Roothaan equation is diagonalized to find the eigenvalue and eigenvector matrices ε and c. These are then used to form a better density matrix, and an improved Fock matrix. These steps are repeated until the new matrix elements differ from the previous ones by some set small amount. When this happens, the calculation is said to have converged.

The largest problem with the HF method is that it considers electron correlation only in an average way. The correlation energy is given by:

$$E_{correlation} = E_{exact} - E_{HF} \quad (14)$$

Where E_{exact} is the true energy and E_{HF} is the energy in the HF limit. Because the electron correlation is not considered in HF calculations, the errors can be quite large. Dispersion interactions, which rely fully on electron correlation, are not possible to model with the HF method. Post HF methods that were developed to be an improvement to HF, such as Møller-Plesset perturbation theory (MP2[49],MP3 etc), configuration interaction (CI)[50] and coupled cluster (CC)[51] do a better job of including electron-electron interaction, but the computational cost and time are often prohibitive.

An advantage of DFT is that it can do a calculation almost as fast as HF with the accuracy of a MP2 calculation.[52] While HF is based on the wavefunction, DFT is based on the electron probability density function.[53] The electron density is only a function of position, with three variable (x,y, and z), and this is true no matter how big the molecule is. The wavefunction of a n-electron molecule is a function of 4n variables, three spatial and 1 spin variable for each electron. In 1964 Honenberg and Kohn demonstrated that all the properties of a molecule could be determined by the ground state electron density function, and also that any trial density functional will have an energy higher than the true energy.[54] Honenberg and Kohn divided the total energy into the following parts.

$$E_0 = E_v[\rho_0] = T_0[p] + V_{Ne}[\rho_0] + V_{ee}[\rho_0] \quad (15)[44]$$

The ground state energy, E_0, is a function of the ground state density, ρ_0, and dependent on the external potential, v. $T_0[p]$ is the kinetic energy of the electrons. $V_{Ne}[\rho_0]$ is the attraction between the electron density and the nuclei and $V_{ee}[\rho_0]$ is the coulombic repulsion between electrons. Each of these terms is a function of the ground state electron density. The term $V_{Ne}[\rho_0]$ is the only known term in this equation.

Kohn and Sham developed a method to find the electron density without the wavefunction and then use that density to find the energy.[55] The Kohn and Sham (KS) method uses a reference system (s) of n non-interacting electrons that has the same

density as the real system (0), and each electron feels the same attraction to the external potential from the nuclei, $v_s(r_i)$.

$$\rho_s(r) = \rho_0(r) \tag{16}$$

The Hamiltonian for the reference system is,

$$\hat{H}_s = \sum_{i=1}^{n}\left[-\frac{1}{2}\nabla_i^2 + v_s(r_i)\right] \equiv \sum_{i=1}^{n}\hat{h}_i^{KS} \text{ and } \hat{h}_i^{KS} \equiv -\frac{1}{2}\nabla_i^2 + v_s(r) \tag{17}$$[44]

where $\hat{h}_i^{KS}$ is the KS one electron operator. The ground state wavefunction of the reference is the Slater determinant of the KS spin orbitals. The spatial part of the spin orbitals are an eigenfunction of $\hat{h}_i^{KS}$.

$$h_i^{KS}\psi_i^{KS} = \varepsilon_i^{KS}\psi_i^{KS} \tag{18}$$

where the ε_i^{KS}'s are the KS orbital energies. In equation (18) for KS non-interacting electrons, the difference between the kinetic energy of the reference systems electrons and the real kinetic energy of the electrons is given by:

$$\Delta T[\rho_0] \equiv T[\rho_0] - T_0[\rho_0] \tag{19}$$

The difference between the columbic repulsion between the reference system's electrons and real systems electrons is given by,

$$\Delta V_{ee}[\rho_0] = \Delta V_{ee}[\rho_0] - \frac{1}{2}\iint \frac{\rho_0(r_1)\rho_0(r_2)}{r_{12}} dr_1 r_2 \tag{20}$$

Where the term $\frac{1}{2}\iint \frac{\rho_0(r_1)\rho_0(r_2)}{r_{12}} dr_1 r_2$ is equal to the repulsion energy between the electrons if they were spread out evenly with a density of ρ_0. The KS equation for energy is as follows:

$$E_0 = E_v[\rho_0] = T_s[p] + \int \rho(r)v(r) + \frac{1}{2}\iint \frac{\rho_0(r_1)\rho_0(r_2)}{r_{12}} dr_1 r_2 + E_{XC}[\rho_0] \tag{21}$$

$$\Delta V_{ee}[\rho_0] + \Delta T[\rho_0] = E_{XC}[\rho_0] \tag{22}$$

$E_{XC}[p]$ is called the exchange-correlation energy functional it includes electron exchange, electron correlation, the kinetic energy difference between the non-interacting electrons and real ones and also the correction to the coulombic repulsion.[56] The first three terms of equation (21) are easy to find and represent the majority of the energy, the last term the exchange-correlation term is difficult to find but represents only a small amount of the energy. The electron density for equation (21) is found by squaring the sum of the KS spatial orbitals.

$$\rho = \rho_s = \sum_{i-1}^{n} \left|\psi_i^{KS}\right|^2 \quad (23)$$

If the exchange-correlation functional was known, DFT would calculate the exact electron density and ground state energy. Because the exchange-correlation functional is unknown; there are many DFT functionals that approximate E_{XC}.

The local density approximations (LDA) are a class of functionals that have the electron density uniformly distributed. Hohenberg and Kohn demonstrated that if the density changes gradually with position then the exchange functional is given by

$$E_{XC}^{LDA}[\rho] = \int \rho(r)\varepsilon_{XC}(\rho)dr \quad (24)$$

where $\varepsilon_{XC}(\rho)$ is the exchange and correlation energy for each electron in an evenly smeared out electron density, with the positive charge also evenly distributed. The exchange energy and the correlation energy for each electron can be computed separately and added together. In a uniform distribution of electron density, the exchange energy for each electron can be calculated exactly using the following equation:

$$\varepsilon_X[\rho(r)] = \frac{9\alpha}{8}\left(\frac{3}{\pi}\right)^{\frac{1}{3}}\rho^{\frac{1}{3}}(r) \quad (25)$$

The variable α is given the value of 2/3 for the method usually referred to as LDA. The Slater(S) method, a type of LDA, has an α value of 1. An expression for the correlation energy density was developed by Vosko, Wilk, and Nusair (VWN)[57] is:

$$e_C^{LDA}(\rho) = e_C^{VWN}(\rho) \quad (26)$$

To make a DFT calculation with a LDA functional or any other functional an initial guess is made for the electron density. From this guess, an approximate value is found for the exchange-correlation potential by taking the functional derivative of exchange-correlation energy with respect to the electron density.

$$v_{XC}^{LDA} = \frac{\partial E_{XC}^{LDA}}{\partial \rho} \quad (27)$$

The value for v_{XC}^{LDA} is used to find the initial KS orbitals. The orbitals are made from a linear combination of basis functions χ_r that are often contracted Gaussian functions.

$$\psi_i^{KS} = \sum_{r=1}^{b} c_{ri}\chi_r \quad (28)$$

Solving equation (18) with the expanded KS orbitals produces an equation similar to the HF-Roothaan equations. The initial orbitals are then used to solve for a more accurate density, which is then in turn used to find a more accurate v_{XC}^{LDA}. The iterations are carried out until the density and the KS orbitals remain constant to a set number of decimal places. The ground state energy is then computed from the converged density and $E_{XC}^{LDA}[\rho]$.

When working with open shelled molecules the Local-Spin-Density Approximation (LSDA) will give better results than LDA. In LDA the KS spatial orbitals contain paired electrons. In LSDA electrons with opposite spins may occupy two different orbitals $\psi_{i\alpha}^{KS}$ and $\psi_{i\beta}^{KS}$.

Generalized-gradient approximation (GGA) functionals attempt to improve LSDA by allowing fluctuation of the electron density with position. This is accomplished by adding gradients of both $\rho^{\alpha}$and ρ^{β}.

$$E_{xc}^{GGA}[\rho^{\alpha},\rho^{\beta}] = \int f\left(\rho^{\alpha}(r),\rho^{\beta}(r),\nabla\rho^{\alpha}(r),\nabla\rho^{\beta}(r)\right)dr \qquad (29)$$

Where f is a function of the spin densities and the gradients. The exchange and correlation functionals are calculated separately. Some common GGA functionals are PBE[58], PW91[59] and BLYP[60-61]. PBE developed by Perdew, Burke and Ernzerhof and PW91[59] developed by Perdew, Chevary, Vosko, Jackson, Pederson, Singh, and Fiolhais both have exchange and correlation functionals with no empirical parameters. The functional BLYP[60-61] has an exchange functional developed by Becke (B88) and a correlation functional developed by Lee, Yang, and Parr. Becke's exchange functional containing the empirical parameter b is shown below.

$$E_x^{B88} = E_x^{LSDA} - b\sum_{\sigma=\alpha,\beta}\frac{(\rho^{\sigma})^{4/3}\chi_{\sigma}^2}{1+6b\chi_{\sigma}ln\left[\chi_{\sigma}+(\chi_{\sigma}^2+1)^{1/2}\right]}dr \quad \chi_{\sigma} \equiv |\nabla\rho^{\sigma}|/(\rho^{\sigma})^{4/3} \qquad (30)$$

The meta-GGA functionals (mGGA) include the Laplacian (second derivative) of the density or the orbital kinetic-energy density in addition to the density and the magnitude of the gradient of the density. The mGGA functionals require more time to calculate than GGA functionals but can give better results. Becke's mGGA functional B95[62] is dependent on the orbital kinetic energy and includes two empirical parameters.

Hybrid functionals are not pure DFT functionals but are a mixture of DFT and HF exchange with DFT correlation functionals. Where:

$$E_{hybrid}^{xc} = c_{HF}E_{HF}^{x} + c_{DFT}E_{DFT}^{xc} \quad (31)$$

The c's are constants. Becke's hybrid GGA functional B3LYP[63], has the following form.

$$E_{xc}^{B3LYP} = (1 - a_0 - a_x)E_x^{LSDA} + a_0E_x^{HF} + a_xE_x^{B88} + (1 - a_c)E_c^{VWN} + a_cE_c^{LYP} \quad (32)$$

The three parameters, the 3 in B3LYP, a_0, a_x and a_c were selected by fitting to experimental atomization energies. In the B3PW91 hybrid functional the LYP correlation term LYP is replaced by a W91[59] term. In 1997 Becke formulated the B97[64] functional as an improvement to B3LYP and B3PW91. The exchange correlation term of the GGA hybrid B97 functional has 10 empirical parameters that were fit to the G2 test set and includes 19.43% HF exchange.

A single electron wavefunction ψ, called a molecular orbital, is made from a linear combination of basis functions χ_s. The group of N, χ_s, basis functions is called the basis set.[46] There are two types of basis functions, Slater Type Orbitals (STO) and Gaussian Type Orbitals (GTO). STOs have an advantage over GTOs in that they more closely resemble hydrogenic atomic orbitals but they have limited use because are they are difficult to calculate. The functional form for Slater orbitals is

$$\chi_{\zeta,n,l,m}(r,\theta,\varphi) = NY_{l,m}(\theta,\varphi)r^{n-1}e^{-\zeta r} \quad (33)^{65}$$

where N is the normalization function and $Y_{l,m}$ are the spherical harmonic functions, r is the distance of the electron from nucleus, and ζ is a constant that is related to the effective charge of the nucleus. In 1950 Boys[66] proposed that the atomic orbitals have the form of a Gaussian function, which are much easier to work with. Gaussian orbitals are shown in equation 34.

$$\chi_{\zeta,n,l,m}(r,\theta,\varphi) = NY_{l,m}(\theta,\varphi)r^{(2n-2-l)}e^{-\zeta r^2} \quad (34)^{65}$$

The r^2 makes the GTO's function's slope zero at the nucleus, and fall off too fast, far from the nucleus, but this can be compensated for by summing up a number of GTOs. By using four or five GTOs to represent one STO, the integrals will be calculated faster than if STOs are used.

The larger the basis set the more correctly it models the orbitals by allowing the electrons to be less restricted in their positions.[47] The basis functions are called contracted functions and the Gaussian functions are called primitives. An uncontracted basis function contains only a single Gaussian function. A minimal basis set has the smallest possible number of basis functions for each atom, one basis function for each inner shell and valence-shell atomic orbital (AO). The minimal basis set STO-3G uses three primitive Gaussian functions (3G) per basis function to resemble a STO.[46] A basis set with two functions for each AO is called a double zeta (DZ) basis set while three functions is called triple zeta(TZ).[65] A split valence basis set doubles or triples only the valence orbitals. Polarization functions add orbitals with angular momentum above the ground state for each atom. Diffuse functions are large size s or p orbitals that let the orbitals spread out more in space.

John Pople developed basis sets that use "SP" shells, which share exponents for s and p functions.[67] The popular Pople split-valence basis sets have the form k-nlmG.[65] Where k is the number of primitive Gaussians used for the core orbitals. The n, l and m express how many functions the valence orbitals are split into, and the number of primitive Gaussians for each. The Pople basis set 6-311G is a triple zeta split valence with the core orbitals represented by six contracted GTOs, and the valence orbitals split into three functions with three, one and one primitive GTO respectively. To add diffuse sp functions to Pople basis sets a (+) for one set of diffuse functions added to the heavy atoms and (++) to add diffuse functions to hydrogens also,for example (6-311++G).[65] The notation (*) after the G indicates polarization functions are added to non-hydrogen atoms and (**) that they are also added to hydrogen. The D95 basis set proposed by Dunning and Huzinaga is a double zeta basis set that is contracted from 9 s primitive functions and 5 p primitive functions on the heavy atoms to 4s and 2p. The correlation-consistent polarized (cc-p) basis sets, developed by Dunning, are more flexible than the Pople basis sets because they do not have equal exponents for the s and p-functions. In the aug-cc-pVTZ,[68] In Dunning basis set, the aug refers to augmented with diffuse functions, and,

VTZ, is split valence triple zeta. Ahlrichs basis set,[69] TZVP is a split valence and triple zeta basis sets with added polarization functions.

CHAPTER 2

MODELS OF THE INHIBITION OF ZINC-FINGER PROTEINS BY REDUCIBLE SULFUR AND SELENIUM COMPOUNDS

Introduction

Zinc fingers (ZFs) are small protein domains, frequently positioned on the surface of the protein, that have Zn^{2+} tetrahedrally coordinated to at least 2 Cys and His.[70] ZFs are involved in many cellular processes including replication, repair, transcription, translation, cell proliferation, apoptosis, metabolism and signaling.[13] Three percent of the human genome encodes for these small (20 to 60 amino acids) ZF domains, the majority of which are transcription factors.[37] Zn^{2+} plays a structural role in the correct folding of the protein, which is required for interaction with DNA, RNA, proteins, or small molecules.[71] ZFs are divided into three classes based on the number and amino acid ligands involved in Zn^{2+} coordination: (1) CCHH, where Zn^{2+} is coordinated to 2 Cys and 2 His, (2) CCCH, where Zn^{2+} is coordinated by 3 Cys and 1 His, and (3) CCCC, where Zn^{2+} is coordinated by 4 Cys[72] (Fig. 1). Zn^{2+} redox inactive, but oxidation of the Cys thiolates release Zn^{2+}, causing the ZF to lose its secondary structure and no longer bind DNA or RNA.[11, 21] The zinc storage protein metallothionein (MT) has 20 Cys residues that reversibly bind 7 Zn^{2+} similarly to CCCC ZF.[73-74] MT, with its low redox potential, releases Zn^{+2} when the Cys residues are oxidized, and binds Zn^{2+} when the Cys are reduced to regulate cellular Zn^{+2} levels and trigger signaling pathways.[12, 15, 20]

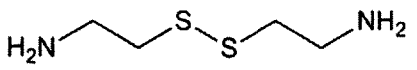

cystamine

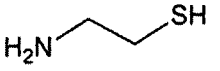

cysteamine

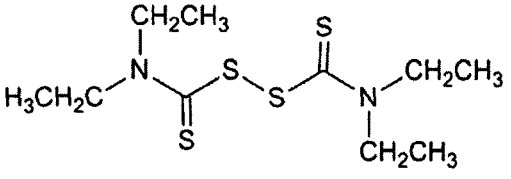

tetraethythiuram disulfide (disulfiram)

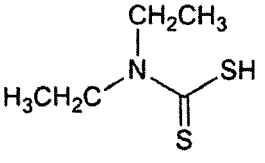

diethyldithiocarbamate (dithiocarb)

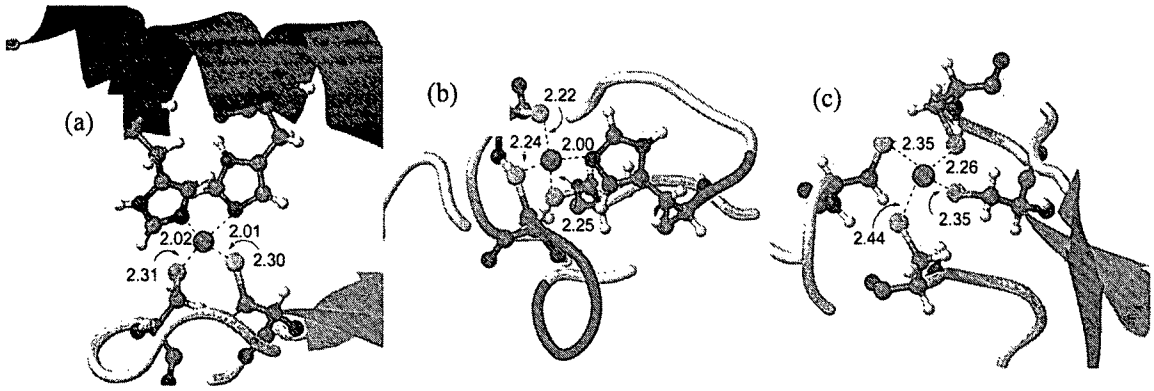

Figure 1. NMR solution structure of each class of zinc-finger proteins.(a) Transcription Factor Sp1 DNA Binding Domain (Zinc Finger 1), PDB 1VA1,[75] as example of Zn-CCHH ZF.(b) NCp7 from HIV-1, PDB 1ESK, as example of Zn-CCCH ZF.(c) DNA-binding domain of the human repair factor XPA, PDB 1XPA, [76] as example of Zn-CCCC ZF. Bond distances in Å.

ZF proteins have been proposed as drug targets for cancer and viral treatment.[14] Several viruses contain conserved CCCH- or CCCC-type ZF motifs that are attractive drug targets because the ZFs are essential for viral reproduction.[37] The E6 oncoprotein (CCCC) in the human papillomavirus (HPV) causes cervical cancer.[26] There is a search for potential drugs to inhibit the E6 protein by releasing Zn^{2+}.[26] The nucleocapsid protein NCp7, a Zn-CCCH ZF protein, from the human immunodeficiency-1 virus (HIV-1), is an attractive antiviral target because it is important for viral assembly and is highly conserved.[5, 77-79] A potential solution to drug resistance in anti-HIV drugs is to target conserved proteins[80,81-82] using electrophilic compounds that release Zn^{2+} from these proteins and terminate virus replication.[83]

Reducible sulfur and selenium compounds (r-S/Se), defined as sulfur and selenium compounds in oxidation states of -1 to +6, have been shown to release Zn^{2+} from various ZF proteins.[27, 31-34, 84] Disulfide compounds cystamine and disulfiram (oxidation state of = -1) were able to release Zn^{2+} from NCp7 CCCH ZF. However, cysteamine and dithiocarb, in the fully reduced (-2) state, could not release Zn^{2+} even after prolonged incubation.[85] Se compounds with an oxidation state higher than -2 react with MT,[86] where as selenomethionine (-2) is not reactive.[27] Se compounds benzeneseleninic acid (oxidation state +2) and benzeneselenenyl chloride (oxidation state 0) release Zn^{2+} from MT even

when there is a 200 to 500-fold excess, the human cellular concentration, of GSH over MT.[86]

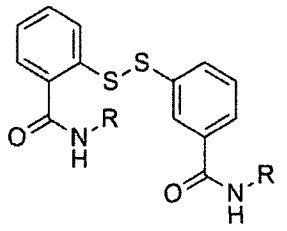

dithiobisbenzamide (DIBA)

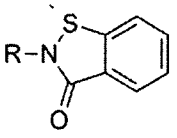

benzisothiazolone (BITA)

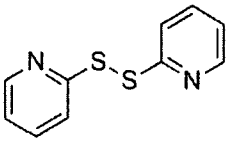

2,2'-dipyridyl disulfide (AT-2)

The National Cancer Institute's drug screening program identified disulfide-substituted benzamides (DIBAs) as ZF reactive compounds.[31] DIBAs quickly cyclize to benzisothiazolones (BITAs) in aqueous solution,[34, 87] release Zn^{2+}, and unfold the NCp7 Zn-CCCH ZF.[31-34] Domagala et al. found that the BITAs were more active than the parent DIBAs and hypothesized that BITAs were reactive intermediates in viral activity.[34] The proposed mechanism of Zn^{2+} release from NCp7 by DIBAs and BITAs is oxidation of the thiolates chelated to Zn^{2+} to form a disulfide.[31-32, 87] DIBA compounds that release Zn^{2+} rapidly were also highly toxic, implying that they may also react with cellular Cys.[87] DIBA drugs that released Zn^{2+} more slowly were much less toxic and were more promising antiviral chemotheropy agents.[87] No resistant virus strains have been found in cell cultures with DIBA's.[88] Aldrithiol-2, or 2,2'-dipyridyl disulfide (AT-2), has been studied extensively both experimentally and theoretically as a deactivator of viral ZF proteins.[24-26, 83, 89-90] AT-2, but not diphenyl disulfide, releases Zn^{2+} irreversibly from NCp7's CCCH ZF from the HIV virus under cellular conditions[83, 90] and recently has been tested in a phase 1 clinical trial (SAV CT 01) of an HIV vaccine.[91] AT-2 also releases Zn^{2+} from E6 (CCCC),[26] the CCCH nucleocapsid of the Friend murine disease,[24] and the arenavirus Z protein with tethered CCCH and CCCC ZF regions.[92]

Ebselen and other r-Se compounds, well-known for their antioxidant activity, can also release Zn^{2+} from ZF proteins and MT[84] and have potential as antiviral and anticancer

agents.[86] r-Se compounds react faster than r-S: selenocystamine releases Zn^{2+} from MT faster than cystamine.[86] Selenocystine, along with phenylselenyl chloride, ebselen, 2-nitrophenylselenocyanate, and phenylseleninic acid, can inactivate the CCCC-type ZF DNA-repair proteins formamidopyrimidine-DNA glycosidase (Fpg) and xeroderma pigmentosum group A protein (XPA)[27] to inhibit DNA binding.[27] Ebselen inhibits the binding of DNA to transcriptions factors TFIIIA and Sp1, both Zn-CCHH ZFs, with disulfide bond formation between two Cys formally coordinated to the released Zn^{2+} [84, 93] The organoselenium compound, 1,4-phenylenebis(methylene)selenocyanate (p-XSC) has been shown to be a chemopreventive agent in many preclinical animal studies.[35-36] p-XSC diminished DNA binding to the CCHH ZF transcription factors Sp1 and Sp2, presumably through modification of the Cys ligands. Its sulfur analogue did not prevent cancer and had no effect on DNAs binding to transcription factors.[94] A proposed target of p-XSC in prostate E6 (CCCC),[26] cancer cells is the CCCC ZF DNA binding domain of the androgen receptor.[95] Zn^{2+} release by selenite may explain how it suppresses tumor cell growth and activates apoptosis.[93]

Scheme 2. Mechanism of Zn^{+2} ejection from ZF proteins by divalent R-S/Se compounds.

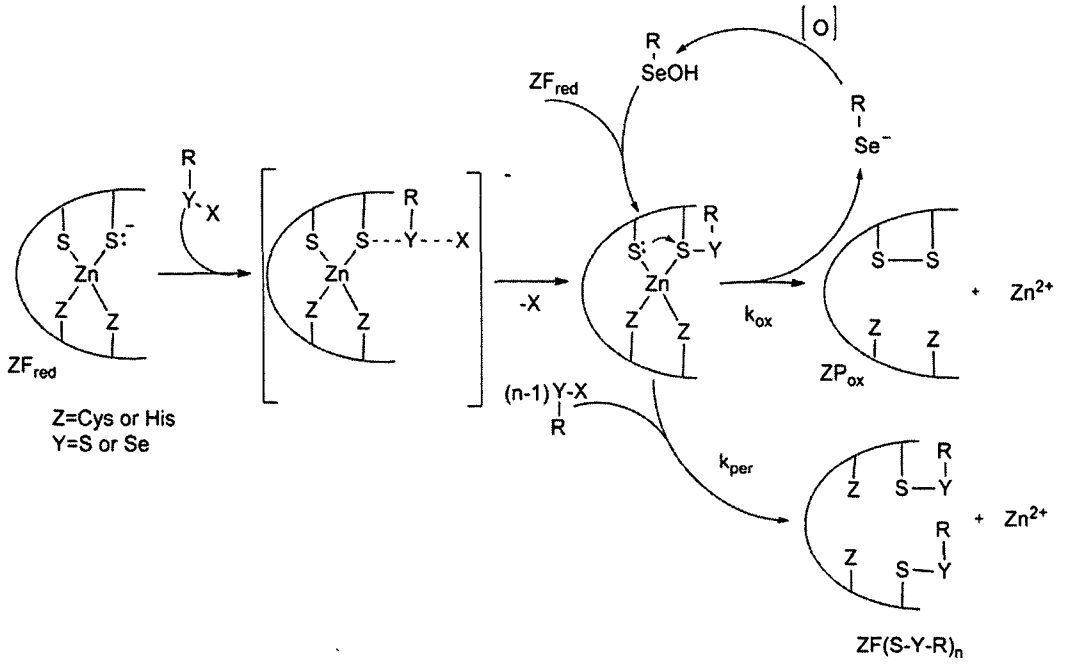

The proposed mechanism for the reaction of reducible sulfur and selenium compounds (r-S/Se) with ZF proteins (Scheme 2) involves the nucleophilic attack on the electron poor S/Se by the sulfur of a ZF Cys to form a S/Se-S bond. The initial attack is followed either by intramolecular disulfide formation with release of RS/Se$^-$ or additional equivalents of r-S/Se can form further S/Se-S bonds. Both paths destabilize the coordination sphere to release Zn^{2+}. RSe$^-$ can react with reactive oxygen species (ROS) to form R-SeOH, which can then react with other ZFs to catalyze Zn^{2+} release.[19, 96] The r-S compounds do not show the catalytic potential that r-Se compounds do based on the difference between the relative stabilities of selenenic and sulfenic acid.[86, 96] When DIBAs and BITAs react with the Zn-CCCH ZF protein NCp7, Reily et al. found apoproteins with intra- (Cys-Cys) and intermolecular (Cys-DIBA) disulfide bonds.[34] Understanding the interaction of r-S/Se with ZF proteins is important for explaining the beneficial chemoprevention, viruscidal activity, and detrimental toxicity of these compounds. It can provide clues about the reactivity of small drugs with ZF proteins and guide the production of new chemo preventive, chemotherapy, and anti-viral agents. In this study

we will use DFT to investigate the interaction of small r-S/Se compounds with models of three classes of ZF proteins: CCHH, CCCH and CCCC.

Theoretical Methods

DFT geometry optimizations and frequency calculations were performed using the Gaussian 09 software package[97] with the PW91TPSS functional. PW91 is the exchange component of Perdew and Wang's 1991 functional[98] and TPSS is the τ-dependent gradient-corrected correlation functional of Tao, Perdew, Staroverov, and Scuseria.[99] This combination of functionals was found to be one of the best performing DFT methods in terms of geometry and interaction energy of the 382 functionals available in the Gaussian 09 software for non-covalent interactions.[100] PW91TPSS was used in conjunction with Dunning's split-valence triple-ζ basis set augmented with polarization functions (TZVP)[101] on C, N, O and H, with added diffuse s and p functions on C, N and O. Se and Zn were represented by the Hurley et al. relativistic effective core potential (RECP) double-ζ basis set augmented with a set of s, p, and d diffuse and polarization functions.[102] The Wadt-Hay ECP basis set augmented with a set of s and p functions was used for S and Cl.[103] Relative energies of formation for the complexes were calculated and corrected for zero-point energies (ΔE + ZPE). The Natural Bond Orbital (NBO) program version 3.1[104] was used to calculate the natural atomic orbital (NAO)-Wiberg bond index (WBI)[105] and the natural population analysis (NPA) charges on all atoms. The WBI, which gives a measure of the bond interaction between two atoms,[106] is the sum of the squares of the off-diagonal elements of the density matrix, P, between pairs of atoms in the NAO basis (Equation 35).[105]

$$B_{AB}^{Wiberg} = \sum_{s\in A}\sum_{t\in B} P_{st}^2 \qquad (35)^{105}$$

The DFT(PW91TPSS) HOMO and LUMO energies were used to calculate the softness (σ) of the ZF models and the r-S/Se compounds used in this study, along with $\Delta E_{covalent}$ of the S/Se compounds. Softness, which measures the ease of charge redistribution initiated by a chemical reaction, is the inverse of hardness (η).[107] Hardness is the second derivative

of the electronic energy (E) versus N (number of electrons) at external potential v(r), and is calculated as the finite difference of ionization potential (IP) and electron affinity (EA) (Equation 36).[107] The second order energy term $\Delta E_{covalent}$ measures the amount an electrophile stabilizes a soft covalent bond. When donor-acceptor interactions form, the electrons are redistributed and the chemical potential (μ) equilibrates between them. The amount of stabilization increases with increasing σ and difference in μ (Equation 37).[32, 107] $\Delta E_{covalent}$ is calculated as the square of electronegativity (χ) times the softness.[32, 107] Electronegativity, the derivative of E versus N at external potential v(r), is calculated as the average of IP and EA (Equation 38).[108 32] IP is the opposite of the DFT HOMO energy,[109] and the EA can be approximated by the opposite of the DFT LUMO energy.[110] Maynard et al. found the DFT calculated $\Delta E_{covalent}$ of a selection of electrophilic agents to positively correlate with the agents experimental reaction rates with NCp7.[32]

$$\eta = \frac{1}{\sigma} = \frac{1}{2}\left(\frac{\partial^2 E}{\partial N^2}\right)_v = \frac{IP-EA}{2} \approx \frac{HOMO-LUMO}{2} \quad (36)$$

$$\Delta E^A_{covalent} = -\frac{1}{4}\frac{\left(\mu^0_B-\mu^0_A\right)^2}{\eta_A+\eta_B} \approx (\chi^0_A)^2\sigma \quad (37)$$

$$\chi = \left(\frac{\partial E}{\partial N}\right)_v = \frac{IP+EA}{2} \approx \frac{HOMO+LUMO}{2} \quad (38)$$

Results and discussion

The S/Se···S interaction formed by the r-S/Se compound and the ZF can be explained with the three center four electron bond of valence bond theory[111] (Scheme 3a). The thiolate lone pair expands S/Se's octet creating a linear L-S/Se-X interaction comparable to a T-shaped hypervalent molecule.[112-113] The resonance structures for this interaction demonstrate the dependence of the strength of the interaction on the basicity of the thiolate donor. Strong basic donors will shift the dominant resonance structure to the right. The stronger the base, the more favored the interaction becomes, and in some cases may shift the dominate resonance structure towards iii in Scheme 3a. In terms of molecular orbital theory, the ZF thiolate donates a lone pair to the S/Se-X antibonding

MO ($\phi^*_{S/Se-X}$) of the r-S/Se compound (Scheme 3b). The incoming thiolate is nearly collinear to the leaving group as this is the direction of in-phase orbital overlap of the thiolate donor lone pair orbital and the linear $\phi^*_{S/Se-X}$. The interaction strength between r-S/Se compounds and the thiolate of a ZF model depends on the strength of the S/Se-X bond and the Lewis basicity of the ZF model. The Weaker S/Se-X bonds are more Lewis acidic because of their available low lying antibonding orbitals.[114] The Lewis basic ZF thiolates have high energy lone pairs.[115-117] The closer in energy the antibonding orbitals is to the donor MO the stronger the donor acceptor interaction.[114] The delocalization of the thiolate charge into the $\phi^*_{S/Se-X}$ orbital decreases the S/Se-X bond order.[117]

Scheme 3. Resonance structures and molecular orbital diagrams for RS/Se-thiolate lone pair interaction. (a) Resonance structures for interaction of RS/Se with the thiolate lone pair. (b) Molecular orbital diagram for the interaction of the RS/Se $\phi^*_{S/Se-X}$ with the thiolate lone pair.

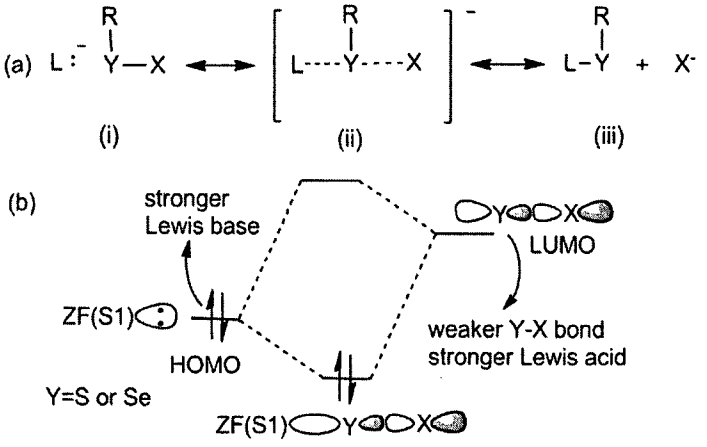

In this study, we investigate the trends in the interactions of r-S/Se compounds with small models of the three ZF classes. The ZF models were constructed to represent

only the coordinating residues since DFT studies by Topol et al. found the chelating Cys and His to be responsible for the bulk of the free energy of metal binding, with other residues contributing only marginally.[118] His was modeled with neutral imidazole (Im) groups and two Cys were modeled with 1,4-butanedithiolate. Each pair of thiolates was connected by a butyl group to approximate the adjoining residues that stabilize the ZF's structure. The butyl was chosen to balance ring strain with flexibility, too small a connection could lead to ring strain and too large would give multiple conformations that would be difficult to work with computationally. The third Cys in the Zn-CCCH model was represented with methyl thiolate. Modeling all Cys with methyl thiolate, which is common in computational models,[118] gives too much freedom of movement to the ligand relative to the actual protein environment where the thiolates are attached to a chain of amino acids (Fig. 2). The DFT(PW91TPSS)-optimized geometries of the resulting models $[Zn(Im)_2(S(CH_2)_4S)]$ **Zn-CCHH**, $[Zn(Im)(SMe)(S(CH_2)_4S)]^-$ **Zn-CCCH**, and $[Zn(S(CH_2)_4S)_2]^{2-}$ **Zn-CCCC** were comparable to values measured from crystal structures deposited in the Protein Data Bank.[119] The Zn-S bond distances increase as the number of sulfur atoms coordinated to Zn^{2+} increase due to steric interaction with other thiolates and the increased negative charge around Zn^{2+}. The WBI for the Zn-S1 bond decreases linearly going from **Zn-CCHH** to **Zn-CCCC** (Fig 3c) revealing a weakening of the bond.

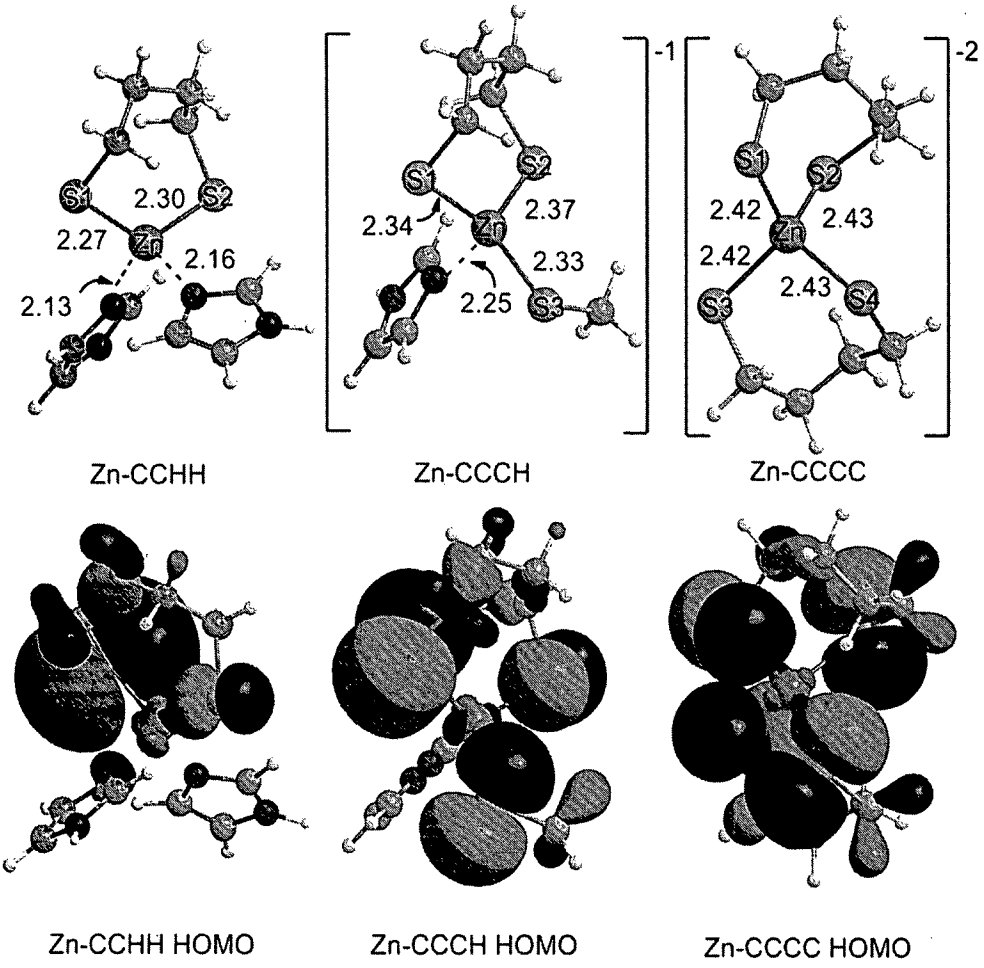

Figure 2. Optimized structure of the three ZF models **Zn-CCHH**, **Zn-CCCH** and **Zn-CCCC**. Bond distances were measured in Å. Orbital representations (isodensity = 0.02) of the HOMO for each model are included.

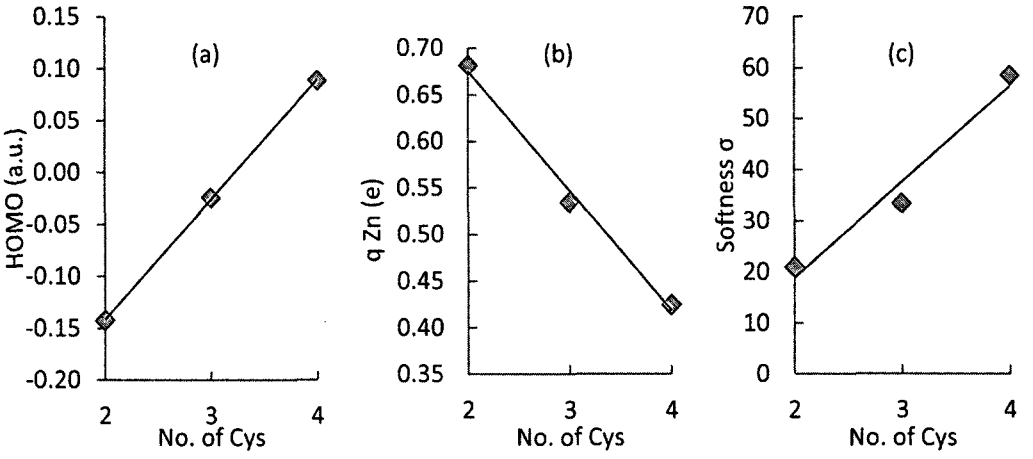

Figure 3. Correlation plots of DFT calculated properties of ZF models. (a) The HOMO energy in a.u. of the 3 ZF models plotted as a function of the number of thiolate ligands. (b) Softness (σ) plotted as a function of the number of thiolate ligands in the ZF models. (c) The WBI for the Zn-S1 bond plotted as a function of the HOMO energy of the ZF models in a.u.

Table 1. DFT(PW91TPSS) results for ZF models. HOMO energy in a.u., WBI and natural population analysis (NPA) charges for model ZF's

Model	HOMO	LUMO	σ	WBI Zn-S1	WBI Zn-S2	WBI Zn-S3	WBI Zn-S4	q S1 e	q S2 e	q S3 e	q S4 e	q Zn
Zn-CCHH	-0.142	-0.047	20.92	0.766	0.698			-0.356	-0.411			0.682
Zn-CCCH	-0.025	0.035	33.40	0.674	0.634	0.694		-0.393	-0.414	-0.382		0.535
Zn-CCCC	0.089	0.123	58.48	0.596	0.590	0.596	0.590	-0.414	-0.423	-0.414	-0.423	0.424

The Lewis basicity of the ZF models increases with the number of Cys ligands, as demonstated by the increase in the HOMO energy and the overall model charge (Fig. 3a, Table 1), indicating that the **Zn-CCCC** will be a better donor than **Zn-CCCH**, which will be better than **Zn-CCHH**. Similary, Topol found the DFT ionization potential of ZF models to decrease, making them more redox reactive, as the number of thiolates coordinated to the Zn^{2+} increased.[118] The HOMO of each ZF model is localized on a thiolate 3p lone-pair MOs that is perpendicular to the Zn-S-C plane (Fig. 2). Of the three thiolate lone pairs, one is involved in the coordinate bond to Zn^{2+}, while the other two are available for

bonding with incoming electrophiles.[19, 120] As you move from **Zn-CCHH** to **Zn-CCCC**, the charge on the Zn^{2+} becomes less positive as the increased number of thiols donate electron density to Zn^{2+}[121](Fig. 3b). The softness (σ) also increases as more thiolates are coordinated to Zn^{2+}, increasing the affinity of the ZF model for soft electrophiles like the r-S/Se compounds (Fig. 3c). The increase in basicity and softness from the added thiolates should cause the initial interaction energy between the thiolate and the r-S/Se reaction to be largest for **Zn-CCCC**.

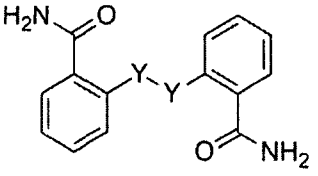

1a Y=S
1b Y=Se

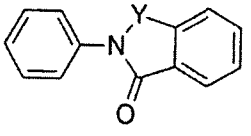

2a Y=S
2b Y=Se (ebselen)

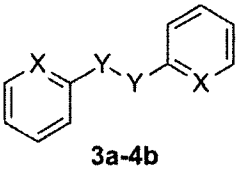

3a-4b

3a X=N Y=S (AT-2)
3b X=N Y=Se
4a X=CH Y=S
4b X=CH Y=Se

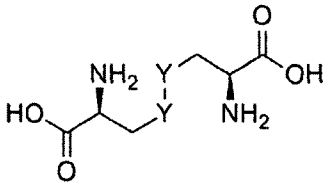

5a Y=S (cystine)
5b Y=Se (Se-cystine)

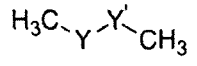

6a Y=S Y'=S
6b Y=Se Y'=Se
6c Y=S Y'=Se
6d Y=Se Y'=S

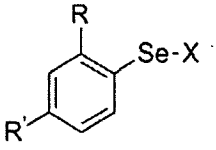

7-12

7 X=Cl R, R'=H
8 X=Cl R=H R'=OCH_3
9 X=CN R, R'=H
10 X=CN R=NO_2 R'=H
11 X=OH R, R'=H
12 X=OOH R, R'=H

The DFT(PW91TPSS)-optimized structures of the r-S/Se compounds 1-12 were comparable to previously reported experimental and theoretical results[19,122-123] (Fig. 4). In general, the Se-Se bond distances are on average 0.28 Å longer that the S-S bonds from the larger size of the Se atom. The Lewis acidity, as measured by the $\phi^*_{S/Se-X}$ energy, softness and $\Delta E_{covalent}$ of compounds 1-12, was compared to make predictions about the strength of donor acceptor interactions with the ZF models (Table 2 and Fig. 5a). The $\phi^*_{S/Se-X}$ in all r-S/Se compounds is generally the LUMO, with the exception of 3a (LUMO+2) and 10 (LUMO+4) due to the strength of the disulfide bond and the intramolecular

interaction with the nitro group, respectively. A low energy $\phi^*_{S/Se-X}$ indicates an unstable S/Se-X bonds that should readily form donor-acceptor interactions with the lone pair electrons of the ZF models. The selenenyl chlorides 7 and 8 had the lowest $\phi^*_{S/Se-X}$ energy, the highest softness, along with the largest $\Delta E_{covalent}$ (Table 2), and are expected to have the strongest donor acceptor interaction with the ZF models. The compounds with the next lowest $\phi^*_{S/Se-X}$ energy are bisbenzamides **1b** and **1a,** followed by ebselen **2b,** selenocystine **5b**, seleninic and selenenic acids **12** and **11**, the sulfur analogue of ebselen **2a**, diphenyldiselenide **4b**, and selenocyanate **9**. The dimethyl compounds **6a-d** have strong S/Se-X bonds and higher energy $\phi^*_{S/Se-X}$ and should be poor acceptors and be less reactive with the ZF models. The oxidation number of the r-S/Se compounds is independent of the LUMO energy and should not be a determining factor in their reactivity with ZFs. Of the compounds that have a sulfur and a selenium analogue (e.g., **2a** and **2b** (Fig. 5b), the r-Se compounds have a lower $\phi^*_{S/Se-X}$ energy, a higher $\Delta E_{covalent}$, are softer, and are thus expected to have a greater interaction with the ZF models than their sulfur analogues. The softness of the r-S/Se compound as well as its $\Delta E_{covalent}$ value, a measure of the amount of stabilization an electrophile gives to a soft covalent bond, correlate well with $\phi^*_{S/Se-X}$ energies, suggesting that $\phi^*_{S/Se-X}$ energies can predict stabilization energy for soft covalent bonds (Fig. 5c) and potentially faster release of Zn^{+2} from ZF proteins. The $\Delta E_{covalent}$ values for **1a** and **2a** follow the same trends as those found by Maynard et al.,[32] to correlate to experimental reaction rates of Zn^{2+} release from HIV's Zn-CCCH NCp7 ZF.

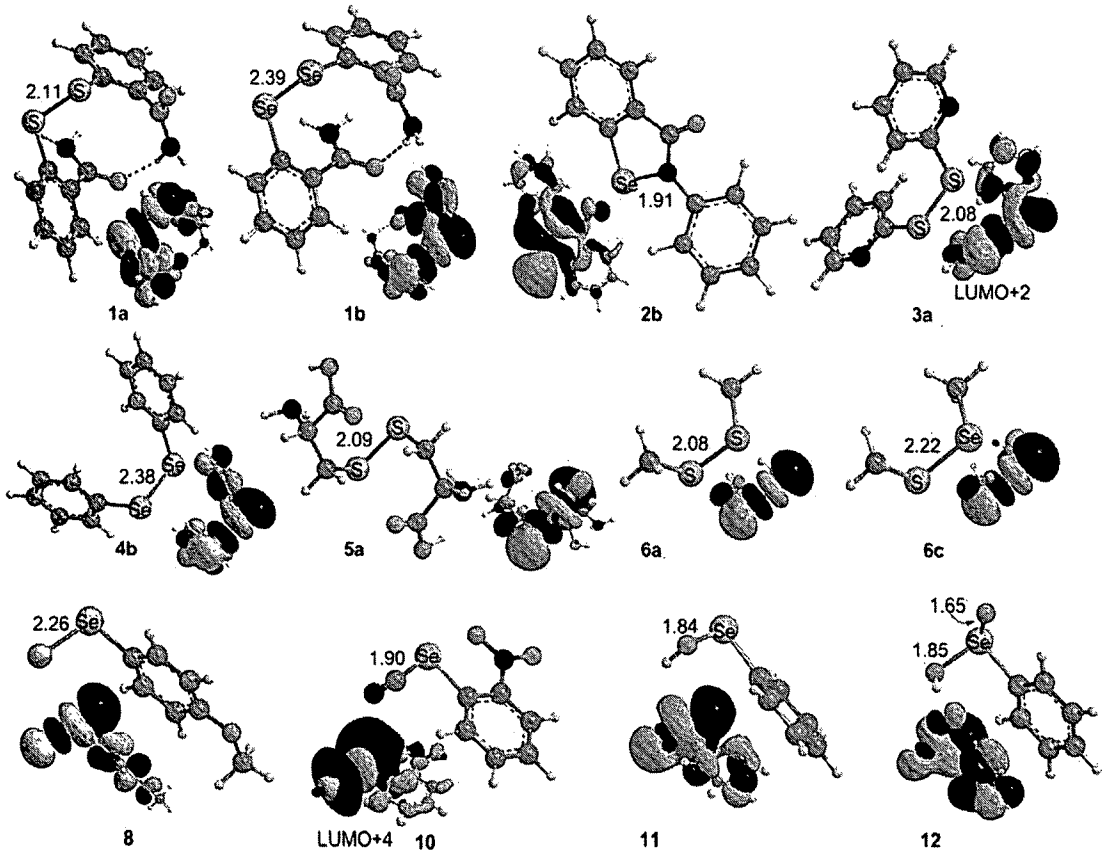

Figure 4. Sample of small S/Se-X molecules with orbital representation of the $\phi^*_{Se/S-x}$. S/Se-X bond distance in Å, with orbital representation of the $\phi^*_{Se/S-x}$ (isodensity = 0.02).

Table 2. DFT(PW91TPSS) calculated results for small S/Se compounds 1-12. LUMO energy in a.u. ,softness σ, $\Delta E_{covalent}$, NPA charge in e, S/Se-X bond distances in (Å), and WBI for the S/Se-X bond for compounds **1-12** *LUMO+2 (**3a**) and LUMO+4 (**10**).

r-S/Se	LUMO	σ	$\Delta E_{covalent}$	qS/Se e	qX e	q(other)	Bond (Å) S/Se-X	WBI S/Se-X
1a	-0.113	20.63	0.537	0.033	-0.221		2.11	1.093
1b	-0.114	21.79	0.554	0.269	0.149		2.39	1.015
2a	-0.092	19.06	0.396	0.586	-0.527		1.76	0.886
2b	-0.103	22.28	0.487	0.690	-0.568		1.91	0.812
3a	-0.067*	14.51	0.268	0.182	0.182		2.08	1.066
3b	-0.082	16.31	0.334	0.225	0.225		2.35	1.069
4a	-0.076	15.52	0.306	0.182	0.182		2.07	1.081
4b	-0.091	20.84	0.458	0.193	0.193		2.38	1.012
5a	-0.078	14.36	0.313	0.086	0.086		2.09	1.056
5b	-0.096	18.46	0.418	0.139	0.139		2.37	1.057
6a	-0.060	13.47	0.243	0.087	0.087		2.08	1.079
6b	-0.081	17.10	0.331	0.140	0.140		2.35	1.087
6c	-0.073	15.92	0.295	0.228	-0.001		2.22	1.069
6d	-0.073	15.92	0.295	-0.001	0.228		2.22	1.069
7	-0.128	27.98	0.750	0.432	-0.278		2.24	0.894
8	-0.121	27.65	0.684	0.427	-0.296		2.26	0.864
9	-0.087	14.19	0.353	0.496	-0.065	(N)-0.310	1.86	1.090
10	-0.039*	10.12	0.191	0.654	-0.085	(N) -0.302	1.90	0.987
11	-0.094	20.50	0.420	0.675	-0.878		1.84	0.835
12	-0.096	14.91	0.396	1.659	-0.927	(O) -0.962	1.85	0.702

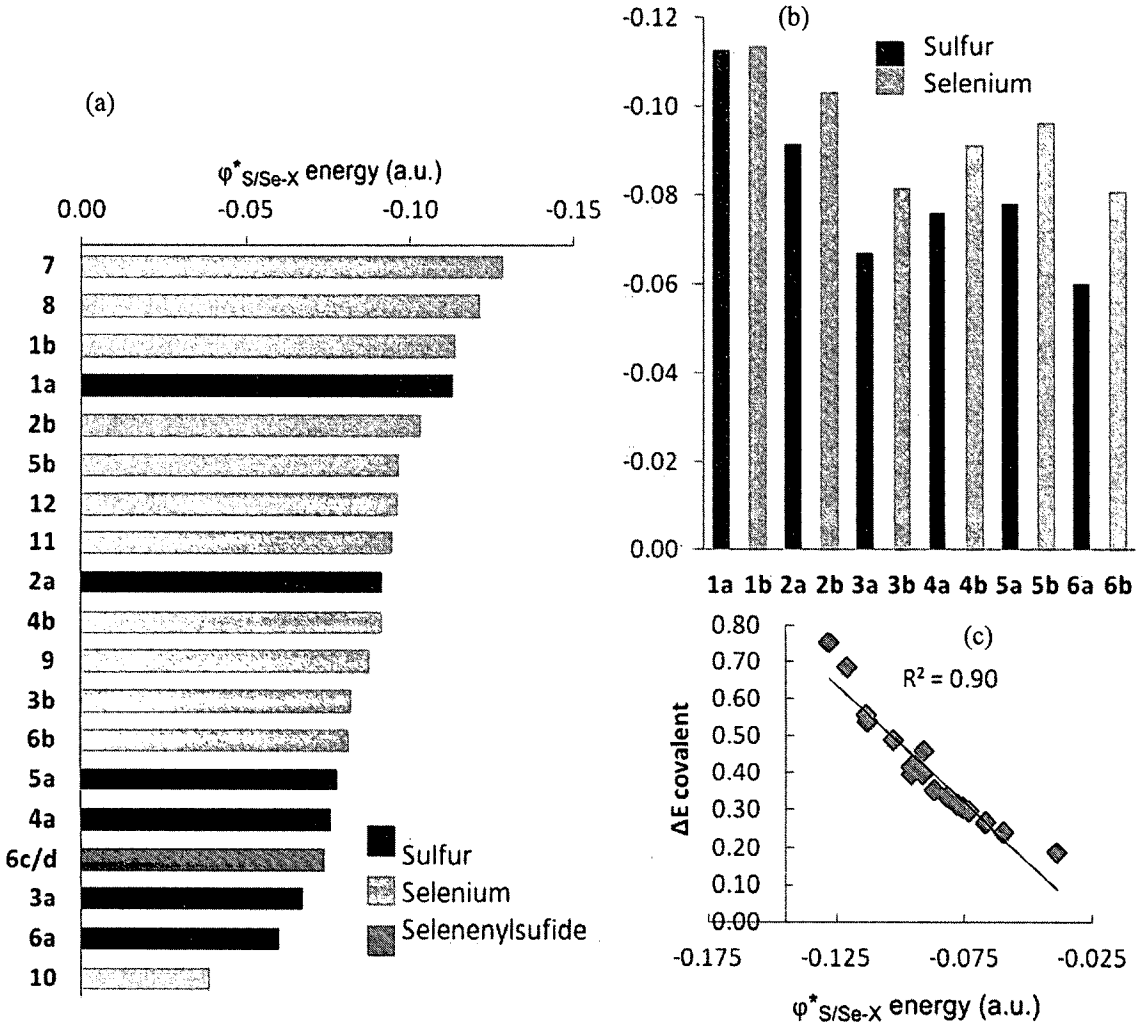

Figure 5. Comparisons and correlations of $\phi^*_{S/Se\text{-}X}$ energy for r-S/Se compounds **1-12**. (a) Comparison of $\phi^*_{S/Se\text{-}X}$ energy. (b) Comparision of $\phi^*_{S/Se\text{-}X}$ energy between all sulfur and selenium analogues. (c) $\Delta E_{covalent}$ plotted as a function of $\phi_{S/Se\text{-}X}$ energy in a.u.

Donor-acceptor complexes were constructed to model the initial (S···S/Se···X) interaction (Scheme 2a) of each of the r-S/Se compounds with all three ZF models. Geometry optimizations and frequency calculations were performed at the DFT(PW91TPSS) level and were comparable to previous results[19] (Table 3). Relative energies of formation for the complexes were calculated and corrected for zero-point energies (ΔE + ZPE). When comparing the relative Lewis basicity of the ZF models to the ΔE+ZPE of the initial S/Se···S donor acceptor interaction, we found common trends for compounds **1-12a**. As expected from the bonding model, the ΔE+ZPE of each r-S/Se compound, with the exception of **6a**, increased with the Lewis basicity of the ZF model, Zn-CCHH < Zn-CCCH < Zn-CCCC (Fig. 6a). Comparison of the $\phi^*_{S/Se-X}$ energy **1-12,** to ΔE + ZPE for the donor-acceptor complexes showed an inverse relationship the interaction with **Zn-CCHH** (Fig. 6b). The correlation demonstrates that the lower the $\phi^*_{Se/S-X}$ energy of the r-S/Se compound, the closer in energy it will be to the HOMO of the ZF model to greater donation and a stronger interaction. The correlation of $\phi^*_{S/Se-X}$ with interaction energy also suggests that the $\phi^*_{S/Se-X}$ energy of a potential r-S/Se compound could be used to test its ability to oxidize ZF proteins. In the interaction of **11** with all 3 ZF models the representations of the bonding MO HOMO-2,(Zn-CCHH) HOMO-4 (Zn-CCCH) and HOMO-7 (Zn-CCCC) captures the electron donation from The HOMO of the ZF model to the $\phi^*_{S/Se-X}$ (Fig 7). The larger electron donation originates from the stronger basicity of the ZF models causing a smaller gap between the HOMO of the ZF and the $\phi^*_{S/Se-X}$. The HOMO-7 is lower than HOMO-2 and HOMO-4 illustrating that the larger electron donation causes the pair of orbitals to have a greater contribution to the overall stabilization of the interacting system. The softness also correlated well with ΔE+ZPE for the Zn-CCHH ZF model, (Fig. 6c) showing that the softer the Lewis acids interact more strongly with the soft Lewis basic ZF models.

The change in the S/Se-X distance as **2a** and **7-12** interact with Zn-CCHH correlates with ΔE+ZPE for that interaction, showing that as the strength of the donor-acceptor interaction increases, the bond to the leaving group is weakened and elongated (Fig. 6d) by the donation into $\phi^*_{S/Se-X}$. The Zn-S1 bond lengthens from the loss of negative charge

on S1 (i.e., q_{S1} = 0.07e (**11-Zn-CCHH**), 0.15e (**11-Zn-CCCH**) and 0.19 e (**11-Zn-CCCC**)) causing it to move away from the Zn^{2+} coordination sphere (compare for **11** in Table 3). The changes in bond length were accompanied by similar shifts in the WBI, for example the inverse correlation to the S/Se-S1 bond distance (Figure 6e). The WBI of the S/Se-S1 bond has a positive correlation to ΔE+ZPE for the interaction of compounds **1-12** with Zn-CCHH, demonstrating that the stronger the bond between S1 and S/Se, the stronger the interaction to the ZF model (Fig. 6f).

In examining the Lewis acidity of the dimethyl compounds **6a-d**, we predicted that **6b**, the diselenide would have the strongest interaction with the ZF models because it has the lowest energy $\phi^*_{S/Se\text{-}X}$, is softer, and RSe^- is more polarizable; therefore, it is more stable than RS^-, making it a better leaving group.[124] Surprisingly, the strongest interactions was with **6c**, the selenenylsulfides, with sulfur as the leaving group, for both the interaction with **Zn-CCHH** and **Zn-CCCH**. For the interaction with **Zn-CCCC**, the ΔE+ZPE was the lowest for **6b** (Fig. 8). Compound **6d**, the selenenylsulfides, with selenium as the leaving group, had a much weaker interaction. The increased interaction for the sulfur leaving group of the selenenylsulfide resulted from the polarization of the Se-S bond (q_S = -0.001e and q_{Se} = 0.228e). Reversing the Se-S bond for **6d**, has S1 donating electron density into the more negative sulfur for an unfavorable interaction. We found the dimethyl disulfide **6a** to have no S···S interaction with **Zn-CCHH** (Fig. 8) as predicted by its weak Lewis acidity. Compound **6a** had several weak S···H-C interactions that account for its stronger interaction with **Zn-CCHH** than with **Zn-CCCH**.

Table 3. DFT(PW91TPSS) results for interactions of r-S/Se compounds with 3 ZF models. Results include relative energies of complex formation, WBIs, bond distances, and NPA Charges.

Model	ΔE	Wiberg indices				bond length Å			Natural Charge		
	kcal/mol	S1-S/Se	S/Se-X	Zn-S1	S1-X	S/Se-X	S1-S/Se	Zn-S1	qS1 e	qS/Se e	qX e
1a-Zn-CCHH	-10.35	0.296	0.689	0.625	0.178	2.30	2.77	2.31	-0.207	-0.144	-0.227
1a-Zn-CCCH	-16.48	0.604	0.379	0.280	0.236	2.69	2.40	2.71	-0.063	0.087	-0.193
1b-Zn-CCHH	-13.89	0.330	0.682	0.606	0.190	2.57	2.76	2.32	-0.165	0.201	-0.010
1b-Zn-CCCH	-22.70	0.677	0.289	0.423	0.181	2.74	2.31	2.49	0.055	0.147	-0.206
2a-Zn-CCHH	-9.33	0.182	0.778	0.666	0.064	1.82	2.99	2.30	-0.315	0.091	-0.540
2a-Zn-CCCH	-20.45	0.374	0.617	0.505	0.137	1.93	2.68	2.42	-0.231	0.440	-0.501
2a-Zn-CCCC	-49.47	0.834	0.233	0.000	0.144	2.38	2.23	6.42	-0.062	0.210	-0.525
2b-Zn-CCHH	-18.06	0.392	0.563	0.586	0.115	2.04	2.71	2.33	-0.218	0.526	-0.573
2b-Zn-CCCH	-30.55	0.489	0.492	0.478	0.132	2.12	2.61	2.43	-0.195	0.513	-0.544
2b-Zn-CCCC	-64.71	0.764	0.302	0.000	0.135	2.33	2.40	7.99	-0.193	0.385	-0.547
3a-Zn-CCHH	-4.76	0.039	1.041	0.705	0.031	2.08	3.63	2.29	-0.370	0.205	0.181
3a-Zn-CCCH	-6.89	0.547	0.457	0.473	0.457	2.53	2.43	2.44	-0.064	0.061	-0.073
3b-Zn-CCHH	-5.34	0.343	0.694	0.608	0.214	2.56	2.73	2.32	-0.174	0.188	0.062
3b-Zn-CCCH	-18.39	0.510	0.505	0.410	0.210	2.70	2.57	2.56	-0.117	0.206	-0.076
4a-Zn-CCHH	-5.23	0.005	1.073	0.665	0.002	2.08	4.65	2.28	-0.434	0.149	0.166
4a-Zn-CCCH	-10.60	0.233	0.809	0.488	0.175	2.23	2.85	2.38	-0.319	0.128	0.058
4a-Zn-CCCC	-23.40	0.604	0.379	0.280	0.236	2.69	2.40	2.71	-0.063	0.087	-0.193
4b-Zn-CCHH	-9.29	0.251	0.794	0.631	0.172	2.50	2.89	2.31	-0.238	0.168	0.084
4b-Zn-CCCH	-16.96	0.330	0.706	0.506	0.216	2.56	2.78	2.42	-0.217	0.214	0.024
5a-Zn-CCHH	-1.89	0.100	0.952	0.657	0.078	2.15	3.24	2.31	-0.373	0.077	0.033
5a-Zn-CCCH	-23.92	0.659	0.364	0.386	0.231	2.71	2.34	2.56	-0.018	0.054	-0.346
5b-Zn-CCHH	-11.51	0.296	0.764	0.591	0.185	2.52	2.84	2.34	-0.262	0.135	-0.061
5b-Zn-CCCH	-32.95	0.314	0.727	0.478	0.223	2.54	2.78	2.45	-0.267	0.121	-0.062
6a-Zn-CCHH	-5.35	0.051	1.023	0.712	0.039	2.11	3.46	2.28	-0.361	0.089	0.044
6a-Zn-CCCH	-4.48	0.108	0.964	0.636	0.083	2.14	3.214	2.34	-0.335	0.114	0.002
6a-Zn-CCCC	-9.92	0.407	0.619	0.408	0.233	2.40	2.62	2.57	-0.170	0.023	-0.199
6b-Zn-CCHH	-8.20	0.183	0.892	0.712	0.137	2.45	3.03	2.30	-0.287	0.111	0.018
6b-Zn-CCCH	-11.36	0.281	0.794	0.654	0.186	2.51	2.86	2.40	-0.263	0.137	-0.061
6b-Zn-CCCC	-19.73	0.450	0.622	0.638	0.230	2.64	2.64	2.60	-0.172	0.117	-0.201
6c-Zn-CCHH	-8.87	0.202	0.868	0.649	0.127	2.32	2.99	2.30	-0.287	0.182	-0.105
6c-Zn-CCCH	-12.03	0.296	0.773	0.542	0.167	2.38	2.84	2.40	-0.267	0.197	-0.164
6c-Zn-CCCC	-19.24	0.507	0.548	0.359	0.209	2.58	2.6	2.63	-0.167	0.169	-0.303
6d-Zn-CCHH	-5.14	0.057	1.006	0.708	0.054	2.26	4.21	2.28	-0.352	0.002	0.171
6d-Zn-CCCH	-5.30	0.161	0.895	0.580	0.144	2.32	3.05	2.38	-0.314	0.025	0.084
6d-Zn-CCCC	-12.73	0.385	0.649	0.453	0.255	2.51	2.64	2.53	-0.144	-0.032	-0.113

Table 3. continued

Model	ΔE	Wiberg indices				bond length Å			Natural Charge		
	kcal/mol	S1-S/Se	S/Se-X	Zn-S1	S1-X	S/Se-X	S1-S/Se	Zn-S1	qS1 e	qS/Se e	qX e
7-Zn-CCHH	-21.84	0.673	0.351	0.501	0.170	2.67	2.44	2.42	-0.065	0.299	-0.605
7-Zn-CCCH	-48.72	0.970	0.111	0.001	0.070	3.17	2.27	5.95	-0.065	0.336	-0.755
8-Zn-CCHH	-20.30	0.536	0.473	0.483	0.187	2.51	2.54	2.35	-0.164	0.291	-0.540
9-Zn-CCHH	-11.00	0.172	0.958	0.656	0.094	1.93	2.99	2.30	-0.308	0.467	-0.058
9-Zn-CCCH	-21.64	0.422	0.723	0.435	0.195	2.10	2.62	2.53	-0.192	0.374	-0.240
9-Zn-CCCC	-30.68	0.417	0.741	0.399	0.172	2.08	2.66	2.58	-0.219	0.368	-0.036
10-Zn-CCHH	-3.07	0.206	0.922	0.639	0.116	1.94	2.91	2.31	-0.292	0.481	-0.056
10-Zn-CCCH	-12.39	0.226	0.915	0.553	0.116	1.95	2.85	2.39	-0.298	0.470	-0.052
10-Zn-CCCC	-26.87	0.344	0.788	0.457	0.172	2.04	2.72	2.51	-0.211	0.437	-0.042
11-Zn-CCHH	-13.84	0.331	0.646	0.619	0.104	1.94	2.81	2.31	-0.251	0.547	-0.942
11-Zn-CCCH	-19.53	0.435	0.570	0.476	0.128	2.00	2.70	2.46	-0.241	0.538	-0.968
11-Zn-CCCC	-29.10	0.570	0.472	0.368	0.141	2.10	2.57	2.64	-0.170	0.451	-1.018
12-Zn-CCHH	-14.02	0.236	0.628	0.637	0.066	1.90	2.93	2.31	-0.286	1.628	-0.954
12-Zn-CCCH	-16.22	0.292	0.580	0.538	0.083	1.93	2.85	2.40	-0.267	1.624	-0.972
12-Zn-CCCC	-26.15	0.515	0.515	0.375	0.102	1.99	2.73	2.52	-0.241	1.549	-1.009

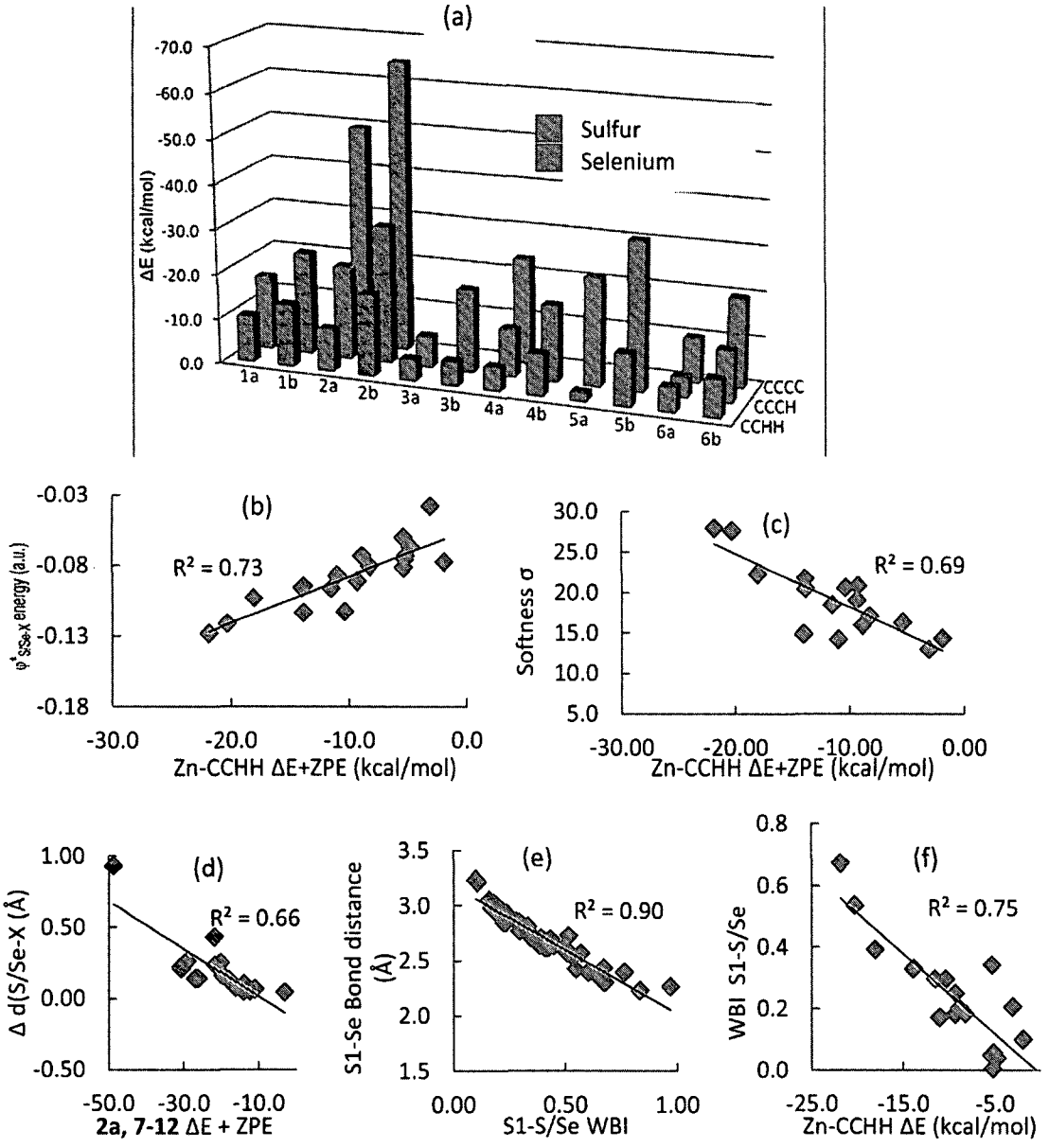

Figure 6. Correlations of calculated data for compounds **1-12** with 3 ZF models. (a) Comparison of Interaction energy for sulfur (blue) and selenium (red) analogues with all ZF models. (b) The $\phi^*_{S/Se\text{-}X}$ energy in (a.u.) plotted as a function of interaction energy of **1-12** with **Zn-CCHH** ZF model. (c) The softness, σ , as a function of the **Zn-CCHH** ΔE+ZPE energy in kcal/mol. (d) Plot of the change in S/Se-X bond distance as a function of the interaction energy for selenium compounds **2a** and **7-12** with all 3 ZF models.
(e) S1-S/Se distance (Å) as a function of the S1-S/Se WBIs for **1-12** with all 3 ZF models. (f) WBIs of the S1-S/Se interaction plotted as a function of the interaction energy of compounds **1-12** with Zn-CCHH ZF model.

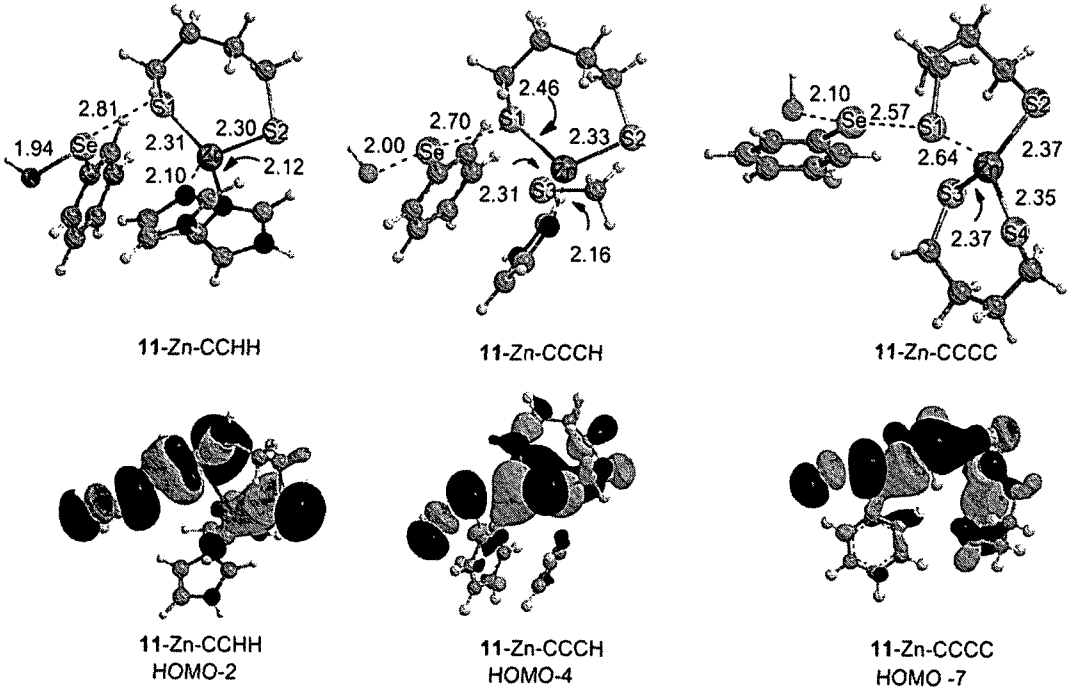

Figure 7. Interactions of **11** with three ZF models. (a) **11-Zn-CCHH**, (b) **11-Zn-CCCH**, and (c) with **11-Zn-CCCC**. (Isodensity = 0.02). Bond distances are recorded in (Å).

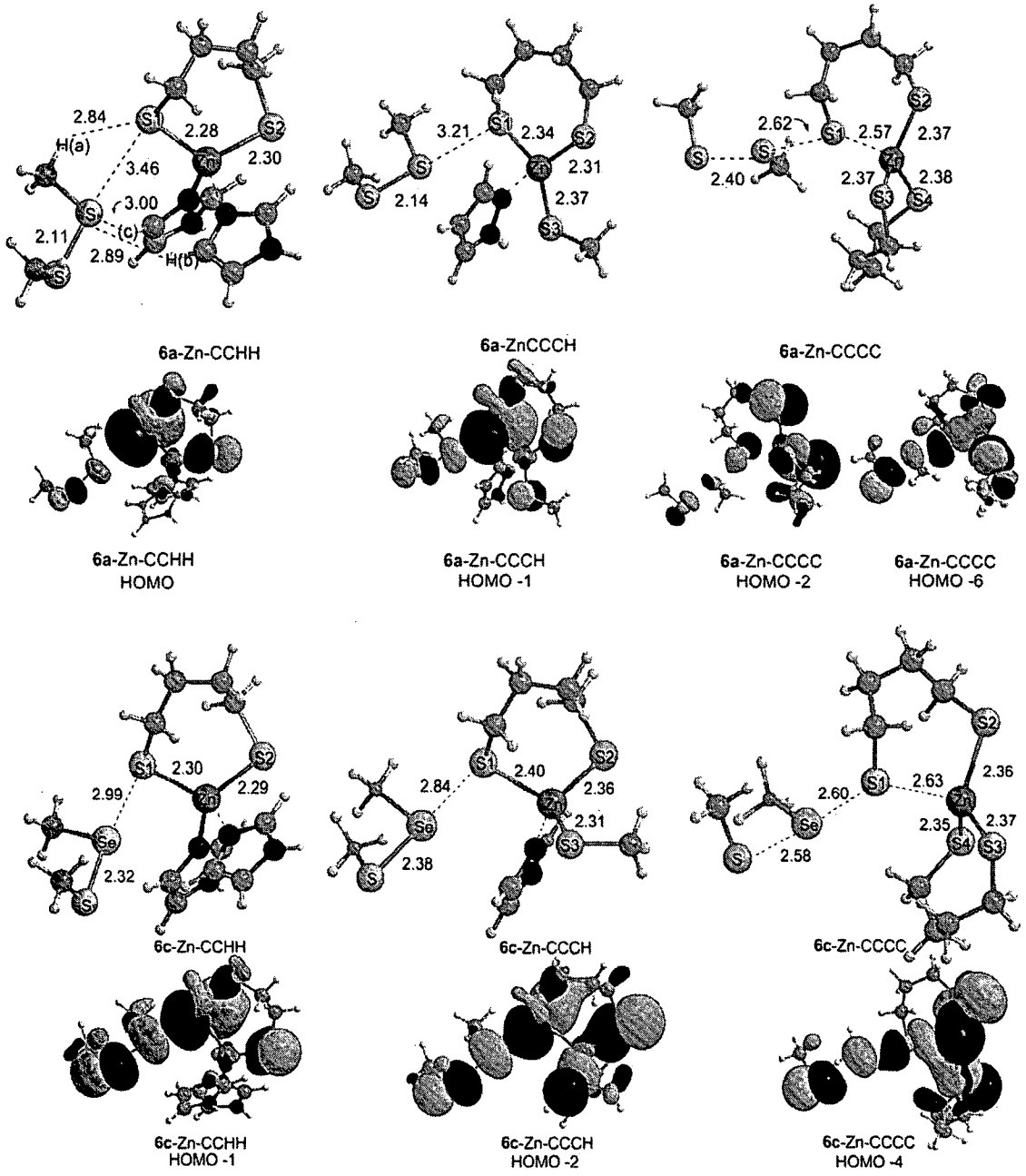

Figure 8. Interactions of **6a** and **6c** with **Zn-CCHH**, **Zn-CCCH** and **Zn-CCCC**. Orbital representaitons are included (isodensity 0.02).

The high Lewis acidity of some of the r-Se compounds led to bond breaking in the donor-acceptor complexes when coupled with strong ZF donors. The interaction of **7** with **Zn-CCCH** shifts the dominate resonance structure towards iii in scheme **2a**, with bond formation between S1 and Se (WBI of 0.97), and Zn-S1 and Se-Cl bond breaking. The formation of the Se-S bond oxidizes the thiolate, which leaves the Zn^{2+} coordination sphere, causing the geometry to change from tetrahedral to trigonal planar (Fig. 9). Similiarly, the interaction of **2b** with **Zn-CCCC** (ΔE+ZPE= -64.71 kcal/mol) has bond formation between S1 and Se, and S1 has left the Zn^{2+} coordination sphere (Fig. 10). The Se-N bond, though weakened, is not broken, leaving N··Se··S1 stuck at the hypervalent structure since in a gas phase reaction there is no water to protonate the amide leaving group. In an earlier DFT study of **2b** with Zn-CCHH, a three water network was added to the initial Se···S interaction to supply a proton for Se-N breaking the bond simultaneous with forming the Se-S1 bond.[125] The Se-S1 bond formation in these gas phase calculations implies that **7**,**8** and **2b** would rapidly release Zn^{2+} from a Zn-CCCC ZF protein.

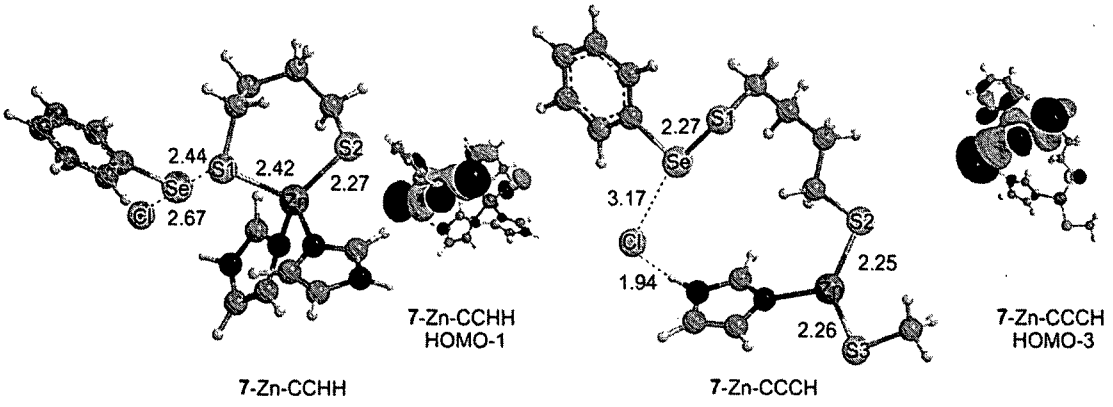

Figure 9. Interaction of **7** with **Zn-CCHH** and **Zn-CCCH** with orbital representation. (iso-density 0.02)

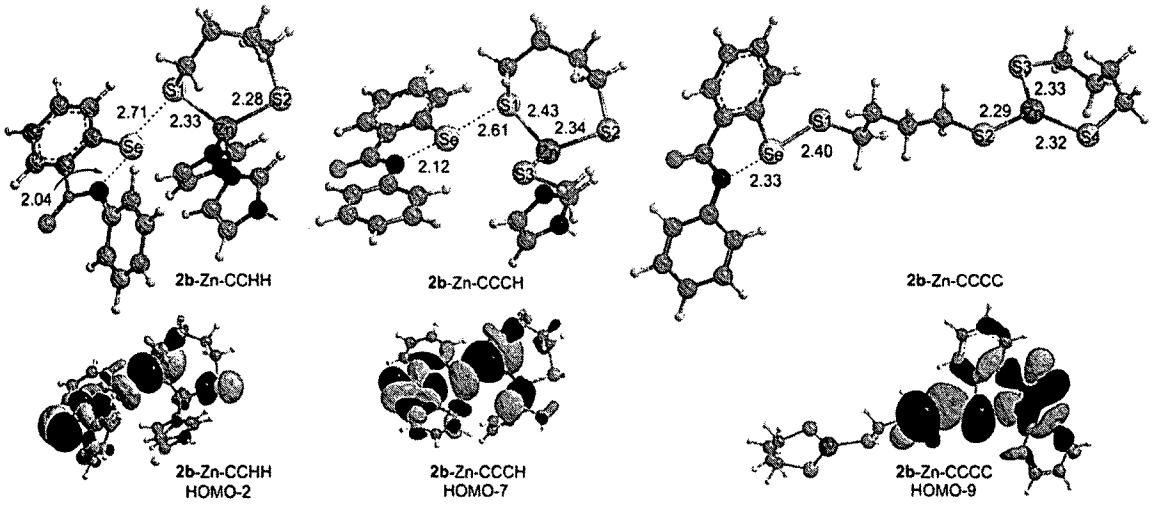

Figure 10. Interactions of **2b** with **Zn-CCHH**, **Zn-CCCH** and **Zn-CCCC**. Bond distances and orbital representations are included. (Isodensity = 0.02).

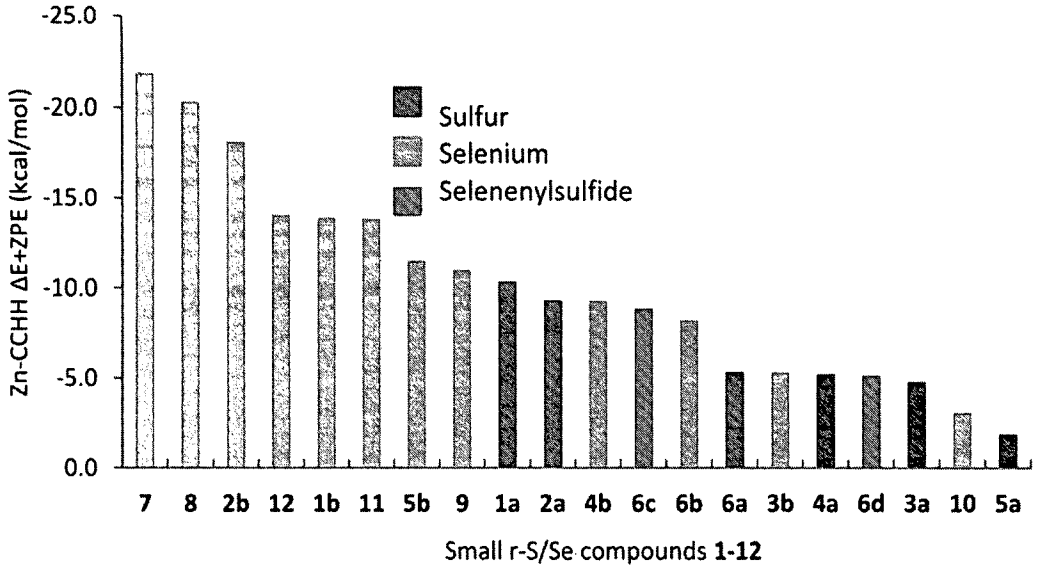

Figure 11. Comparison of compounds **1-12** ΔE+ZPE with **Zn-CCHH**.

Overall, the r-Se compounds had stronger interactions with the ZF models than the r-S compounds (Fig. 11). The lower ΔE+ZPEs of the r-Se compounds are caused by the relative instability of Se-X bond compared to the S-X bond. Selenium is larger and, therefore, a more polarizable (softer) Lewis acid than sulfur, making it a better electrophile for reacting with the soft Lewis base ZF models. Blessing et al. found that while **5b** and **12** inhibited Fpg activity, their sulfur analogues did not, even at high concentrations.[27] Vallee et al. found that rSe compounds were better able to release Zn^{2+} from MT than their sulfur counterparts.[86] Experimentally, Blessing et al. found **2b,** to be the most effective at inhibiting the activity of Fpg with a CCCC ZF, followed by **7**, **10**, **12**, and **5b**, but found **10** better able to release Zn^{2+} from a peptide of XPA with a Zn-CCCC ZF than **5b>12>2b>7**.[27] Our DFT calculations found **2b** to have the highest interaction energy (-64.7 kcal/mol) with **Zn-CCCC** followed by **10** and **12** (-26.9 kcal/mol) consistent with the experimental trend for Fpg. **5b** and **7** are highly reactive, as they both had Se/S1 bond formation and S1-Zn dissociation. We do not see full correlation between the DFT results and Blessing's experimental results due to the effect of sterics and other interactions with the surrounding residues as reflected in the differing experimental results for Fpg and XPA. There is much interest in **2b** as a therapeutic drug because of it low toxicity *in vivo*.[126] Ebselen is less toxic than other Se compounds, with a mice LD_{50} of 400μmol/kg[127] which is attributed to its Se not being bioavailable.[128] The DFT reaction barrier for the interaction of **Zn-CCHH** was lower with **2b** than with H_2O_2 due to the softness of the Se atom.[125] Experimental evidence shows that **2b** reacts more slowly with MT than with a free thiolate,[84] and there is a higher activation barrier for **2b** with MeSH than with Zn-CCHH.[129] Because CCCH and CCCC are more nucleophilic than Zn-CCHH, the barriers are expected to be lower. Topal, in a DFT study, found the potential curve for cyclic disulfides with model CCCH ZFs to be almost barrierless.[130] For the Zn-CCHH interaction with **2b**, the modest reaction barrier allows the S-Se-R bond to last long enough for the formation of intramolecular disulfide bonds and $ZF_{ox.}$($k_{ox}>k_{per}$; Scheme **2**).[125] When **2b** interacts with CCCC ZFs or MT, Se-S bond formation is much faster ($k_{per}>k_{ox}$), and additional **2b** forms further Se-S bonds.[131] The intermediate basicity of the less studied Zn-CCCH may interact

via a different pathway. Valley et al. concluded that since **2b** reacts faster with GSH than with MT, and still releases Zn^{2+} in the presence of GSH, that **2b** reacts with ZF's through a ebselen-GSH selenenyl sulfide intermediate.[84]

Although r-Se compounds are potentially more reactive with ZFs, there is more experimental data available for r-S compounds. Our DFT results are in reasonable agreement with experimental data. For example, **1a** and **2a** equally release between 25 to 75% of Zn^{2+} from NCp7's Zn-CCCH ZF, whereas **4a** is unreactive.[83, 87] **1a** and **2a** were shown to form strong S···S interactions with ZF models due to their low energy $\phi^*_{S/Se\text{-}X}$ MOs, but **4a** does not interact with either **Zn-CCHH** or **Zn-CCCH**, but does interact with **Zn-CCCC** (Fig 12). Experimentally, **3a** releases 60% of Zn^{2+} from the E6 CCCC-type ZF, while **4a** and **5a** release only 15 and 12%, respectively.[26] Our results for **4a** are in agreement with experimental results that show it is not reactive with CCCH ZFs but is reactive with a CCCC type ZF proteins. We found **3a**, AT-2, to interact with **Zn-CCCH** but not **Zn-CCHH** consistent with Huang et al.'s experimental data. These results suggest that some weakly oxidizing agents can selectively react with CCCH ZFs, and not with CCHH or CCCC types.[88] Topal et al. also found that **3a** was able to attack the NCp7 CCCH ZF, but had weak activity against CCHH and CCCC ZFs.[83]

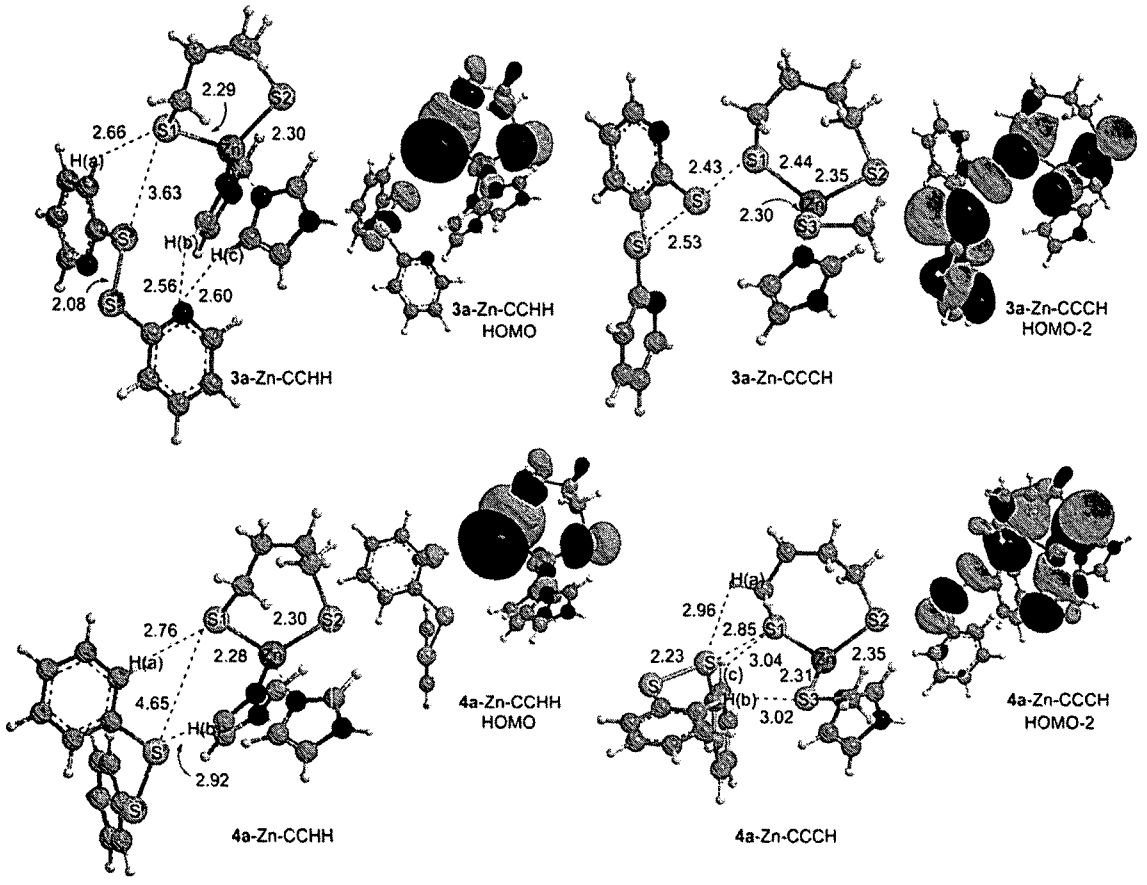

Figure 12. Interactions of **3a** and **4a** with **Zn-CCHH**, **Zn-CCCH** and **Zn-CCCC**. With orbital representaitons included. (isodensity 0.02).

Conclusion

The interaction of r-S/Se compounds with the zinc bound thiolates of three classes of ZFs, was investigated using DFT. We found that increasing the number of thiolates coordinated to Zn^{2+} led to stronger interactions with the r-S/Se compounds. The $\phi^*_{S/Se-X}$ of compounds **1-12** had an inverse correlation with the ΔE+ZPE of all r-S/Se compounds with **Zn-CCHH** ZF model, which demonstrates that the lower the $\phi^*_{Se/S-x}$ energy of the r-S/Se compound, the closer in energy it will be to the HOMO of the ZF model. And the low lying $\phi^*_{S/Se-X}$ are better able to accept electron donation from the Lewis basic ZF models, making the donor acceptor interactions stronger. The correlation of $\phi^*_{S/Se-X}$ with interaction energy suggests that the LUMO energy of a potential r-S/Se drug could be

used to test its ability to oxidize ZF proteins. The initial S/Se···S interaction for the complex formation of r-S/Se compounds with all three ZFs had common trends across each of the compounds **1-12a**. The ΔE+ZPE of each r-S/Se compound, with the exception of **6a**, increased with **Zn-CCHH** < **Zn-CCCH** < **Zn-CCCC**. The changes in geometry, charge, and WBIs that accompanied the increase in energy from the additional thiolates were the following: (1) the bond between S/Se-X and Zn-S1 expanded, while concomitantly the S1-S/Se bond distance decreased, (2) the WBI decreased between S/Se-X and Zn-S1 and increased between S/Se-S1, (3) the NPA charge on S1 because more positive, while the NPA charge on X decreased. The Wiberg of the S1-S/Se bond exhibits an inverse correlation to the S/Se-S1 bond distance, validating the WBI as a measure of bond strength. The WBI of the S/Se-S1 bond has a positive correlation to ΔE+ZPE for the interaction of compounds 1-12 with Zn-CCHH, demonstrating that the stronger the bond between S1 and S/Se, the stronger the interaction to the ZF model. The change in the S/Se-X distance as compounds **1-12** interact with Zn-CCHH correlates with ΔE+ZPE for that interaction, showing that as the interaction of r-S/Se to S1 increases, the bond to the leaving group is weakened and elongated.

In our study of r-S/Se compounds with ZF models, the models was limited since they were constructed to represent only the coordinating residues. Although the free energy of metal binding is coming from the coordinating ligands, the other residues can affect the nucleophilicity of the thiolates. A zinc bound thiolate is less reactive if it is N-H--S hydrogen bonded to the peptide backbone or other residue. GATA-1 (CCCC-type ZF transcription factor) had a much lower ionization potential than the CCCH ZF from NCp7 due to additional Cys thiolates, but the ligands were more sterically hindered than in NCp7, and thus less reactive. For future work, larger models that include the entire ZF protein from each of the classes, would be modeled with hybrid quantum mechanics/molecular dynamics (QM/MM) methods.

CHAPTER 3

DFT MODELING OF THE π-STACKING INTERACTIONS BETWEEN METALATED GUANINE AND TRYPTOPHAN AT THE NCp7 DNA RECOGNITION SITE

Introduction

Human immunodeficiency virus-1 (HIV-1) is a lentivirus in the retrovirus family that progresses to AIDS through a large number of replication cycles.[132] In the last 30 years, more than 35 anti-HIV drugs have been developed.[133] The majority are either reverse transcriptase inhibitors (RTI) or protease inhibitors (PRI).[133] Combinations of RTI and PRI, called highly active antiviral therapy (HAART), has been shown to boost clinical markers and stall resistance.[134] HAART has been used to delay the onset of AIDS, but cannot cure the disease, only diminish HIV transmission.[135] HIV-1 has a high rate of virus replication combined with high error prone reverse transcriptase with no proof-reading ability, making the largest problem with anti-HIV drugs the rapid development of drug resistant viruses.[135,136,137] The HIV-1 virus is resistant to one or more antiviral drugs in 75-85% of patients.[137] New antiviral agents that target novel viral and cellular processes are critical for developing new combinations of inhibitors.[80,81-82]

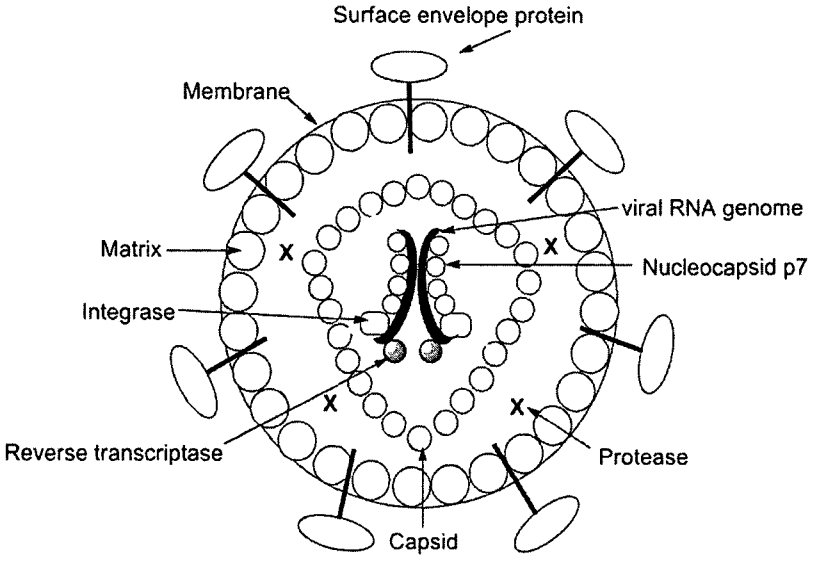

Figure 13. Structure of HIV virus.[138]

Much attention lately has been given to highly conserved structures that would be immune to mutations.[139-140,141] HIV-1 viruses have an outer envelope that encompasses the capsid, which in turn surrounds the nucleocapsid (NC). The NC structure contains the genomic RNA coated with around 2000 nucleocapsid proteins (NCp7)(Fig. 13).[138, 142] The NCp7, derived from the HIV structural protein Gag,[79] is a highly basic small protein that has two copies of a Cys-X_2-Cys-X_4-His-X_4-Cys zinc binding domain. The spacing and the metal-coordinating residues of the NC CCHC zinc finger (ZF), is highly conserved among retroviruses.[143] Altering a residue in the CCHC sequence results in non-functioning virons,[78, 143-146] verifying that NCp7 is mutation resistant.[147]

NCp7 is involved in many steps of the HIV life cycle (RNA binding, protecting and encapsidation[79], reverse transcription,[77, 148] strand transfer,[79] protection of viral DNA fragments,[149] and virus assembly/release[78]). Blocking any one of these steps could terminate HIV reproduction because the main mode of action in each process is the binding of NCp7 to single stranded nucleic acid.[150] NCp7 is an attractive target for the development of new antiviral agents since it is involved in both early and late steps in viral production, is a highly conserved structure, and the CCHC ZF is rare (most cellular zinc-fingers are CCHH or CCCC-type).[5]

Trp37 in the C-Terminal ZF (ZF-2) of NCp7 is crucial for RNA encapsidation and virus replication. Replacing W37 with a non-aromatic residue results in non-infective viruses with defective RNA packaging.[78] Zn^{2+} binding to CCHC induces a fold in the protein that exposes W37.[151] The interaction of NCp7 with a single-stranded pentanucleotide d(ACGCC), a short piece of stem loop 2 (SL2) of the ψ packaging signal, showed that W37 was π-stacked with a Gua base of the nucleotide.[151] When NCp7 was bound to various hexanucleotides, it was found that the finger region (12-53) is responsible for the interaction.[152] Irrespective of the position of Gua, it plays a critical role in the binding of RNA to NCp7.[152] The binding of NCp7 involves hydrogen bonding and hydrophobic stacking interactions.[152] The presence of Zn^{2+} is essential for binding of NCp7 to both RNA and DNA.[152] A molecular dynamics (MD) study of the interaction of NCp7, with both the RNA ψ packaging signal SL3 and the DNA(-) primer binding site (PBS), found the

recognition motif for Gua to be composed of π-stacking interactions with W37 and Q45 and H bonding to M46.[153] These three residues, W37, Q45, and M46, form a hydrophobic plateau on the upper surface of the distal finger.[151]

Molecules with electrophilic functional groups have been used to inhibit NCp7 by reacting with the Cys ligands of ZFs causing the protein to release Zn^{2+} ion and unfold. The lack of specificity of these electrophilic molecules for NCp7 ZFs has impeded their use as antiviral drugs.[154] An alternate strategy would be to design drugs that compete with RNA and DNA for the binding to NCp7. If the competitor compound binds with a higher affinity for NCp7, they will be able to inhibit NC binding to RNA and DNA. Drugs that act as antagonists of the RNA/DNA protein interaction are worth investigating as selective NCp7 inhibitors. Compounds that selectively π stack with W37 and remove Zn^{2+} could target NCp7 without interfering with cellular ZFs.

Alkyation of the nucleobase antagonists has been proposed as a mechanism for enhancing binding to W37 of NCp7.[155-158] Increased π-stacking between the positively charged methylated base and aromatic amino acid side chains is proposed to be responsible for the preferential recognition for alkylated bases.[157] The positive charge of the methylated base is delocalized over aromatic ring[157] and lowers the energy of the lowest unoccupied molecular orbital (LUMO) to make it a better acceptor for electron density from aromatic side chains.[157, 159] Trp is the best electron donor of the aromatic amino acids[160] and ^1H NMR studies show that methylation of Gua's N7 increases its π-π interaction to W's indole ring.[161]

Like methylation, the coordination to metal ions enhances the π-stacking interactions between nucleobases and aromatic amino acids.[162] Experiments show that π-stacking interactions to Trp are strengthened when the nucleobase is coordinated to a Pt^{2+} ion.[40-41, 162] The preferred metalation site for Pt^{2+} on Guan is N7, because the Gua carbonyl group increases the basicity of N7.[163,164] The association constants for platinated 9-ethylguanine (9-EtGua) with N-acetyl tryptophan and with the C-terminus of the second ZF (ZF-2) of NCp7 was about twice that of free 9-EtGua (K_π = 7.0 and 3.5 x 10^3 M^{-1}) respectively.[42] The binding constant was slightly lower for the palladium analog of the

metalated nucleobase. The circular dichroism (CD) spectrum of [Pt(diene)9-(EtGH)]$^{+2}$ with ZF-2 showed adduct formation, presumably through enhanced π-π interactions between W37 and metalated Gua with little disturbance of the ZF 3-d structure.[42] Targeting of the Gua-Trp interaction can be coupled with an electrophile to release Zn^{2+} to inhibit DNA binding. For example, reaction of trans-[PtCl(9-EtGH)(py)]$^{2+}$ with ZF-2 demonstrated a significant change in the 3-D structure of the ZF, due to the loss of the Zn^{2+} ion.[42] The enhanced π-stacking interactions caused by metalation of the nucleobases is believed to originate from increased donor-acceptor interactions.[157] The increased positive charge from the metal ion lowers the LUMO energy of the nucleobase and brings it closer in energy to the HOMO of Trp. The closer in energy the nucleobase's LUMO is to Trp's HOMO the stronger the interaction will be.[165]

The present study investigates the enhancement of the interaction between Gua and Trp through methylation and metalation of the nucleic acid bases. DFT calculations will be performed on small models of methylated and metalated MeGua and Xan π-stacked with MeInd as a model for Trp. The π-stacking energy, LUMO energies, and charge transfer will be examined in order to determine if the modified MeGua with the lowest LUMO energies have the largest charge transfer and the strongest π-stacking interactions. Larger models of truncated ZF-2 of NCp7 will be used to explore the added binding strength originating from hydrogen bonding interactions of modified MeGua with surrounding residues. Understanding the effect of metalation on π-stacking could lead to the design of chemotherapeutic agents that target specific recognition sites of DNA/RNA-protein interactions.

Theoretical Methods

Geometry optimizations of small models were performed using Gaussian 09[97] with the B97-D semilocal generalized gradient approximation (GGA) DFT functional, a re-parameterization of Becke's[64] B97 functional with a semi-empirical dispersion correction.[166] B97-D performs very well for non-bonded interactions[167] and adequately models all relevant interactions found in biological systems.[168] The D95V basis set with

polarization functions was used for C, H, N and O. Wadt/Hay ECP basis sets augmented with polarization functions were used for S,[103] Pt, and Pd.[169] The π-stacking interaction energy was calculated as the relative energy of the complex and the DFT-optimized monomers.

Charge decomposition analysis (CDA), as implemented in the Multiwfn program,[170] was used to quantify charge relocation between fragments in the π-stacked complex.[171] CDA builds the wavefunction of the complex from a linear combination of the donor and acceptor fragment orbitals (LCFO).[171] The charge donation from the occupied (occ) orbitals of the donor to the virtual (vir) orbitals of acceptor is denoted by d (Equation 39) where i and η are the index and occupation number of the molecular orbitals (MO) of the complex, $C_{m,i}$ is the coefficient of fragment orbital (FO) m in MO i of the complex, and $S_{m,n}$ is the overlap integral between FO m and FO n.[171]

$$d_i = \sum_{m\epsilon A}^{occ} \sum_{n\epsilon B}^{vir} \eta_i \, C_{m,i} C_{n,i} S_{m,n} \qquad (39)^{171}$$

The back donation from the occupied orbitals of the acceptor to the virtual orbitals of the donor is denoted by b (Equation 40).[171] The net electrons transferred (d-b) from the donor to the acceptor will be examined to see if there is a correlation to the LUMO energies of the modified Gua, and to the π-stacking interaction energy.

$$b_i = \sum_{m\epsilon A}^{vir} \sum_{n\epsilon B}^{occ} \eta_i \, C_{m,i} C_{n,i} S_{m,n} \qquad (40)^{171}$$

The larger models were optimized using the ONIOM method[172] as implemented in Gaussian 09. Our ONIOM method divides the structure into two different levels of accuracy, a semi-empirical (SE) level and a quantum mechanical (QM) level. The SE region was constrained to the solution structure to preserve the steric effects of the surrounding protein,[173] while the QM region was allowed to freely optimize. The QM region was modeled with B97-D while the SE regions was modeled with PM6, a recently developed SE method that emphasizes biochemical systems in parameterization.[174] PM6 had greater accuracy on the heat of formation of biological compounds than HF and B3LYP/ 6-31G(d).[174]

Donor-acceptor energies ($\Delta E_{d\rightarrow a}$) along with the natural atomic orbital NAO-Wiberg Bond Index (WBI)[105] (Equation 41) and the natural population analysis (NPA)

charges on all atoms were calculated with the Natural Bond Order (NBO) program Version 3.1.[104,175] The WBI, which gives a measure of the bonding interaction between two atoms,[106] is the sum of the squares of the off-diagonal elements of the density matrix P between pairs of atoms in the NAO basis.[105]

$$\underset{AB}{Wiberg} = \sum_{s\in A}\sum_{t\in B} P_{st}^2 \qquad (41)^{105}$$

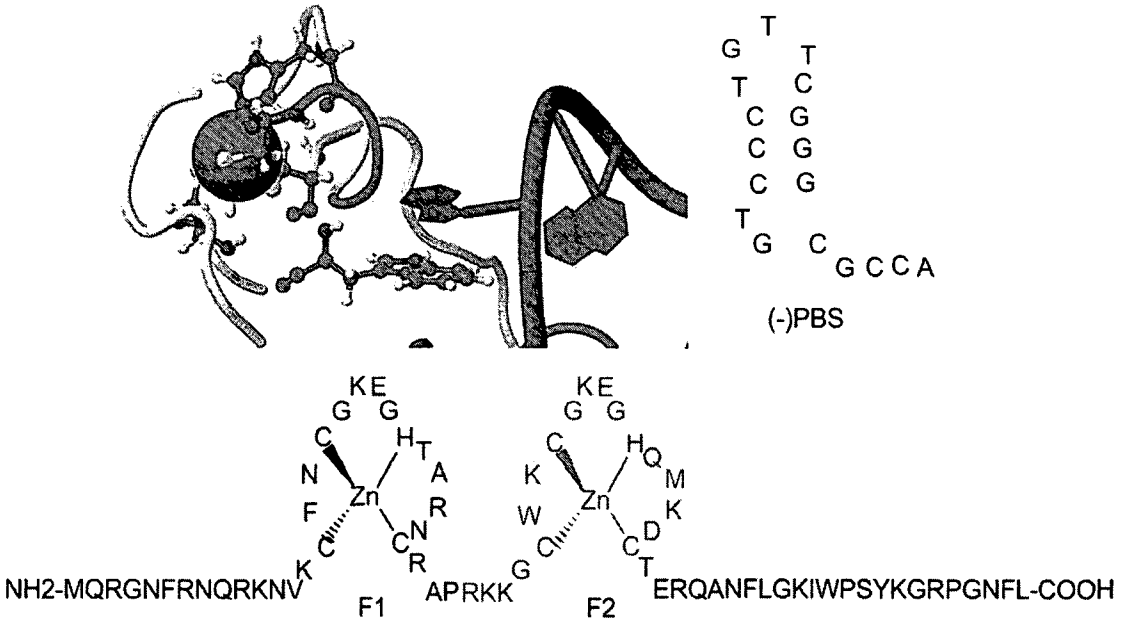

Figure 14. Solution structure (PDB 2EXF[176]). HIV-1 NCp7 complexed with DNA (-) primer binding site (PBS) with Gua. ZF-2 is shown in gray.

Results and Discussion

Small π-π stacked structures

Small models were constructed of MeGua π-stacked with 3-methylindole (MeInd), as a model for L-Trp, in the same orientation (**A**) found in the NMR solution structure (PDB 2EXF)[176] (Fig. 14). The dimers MeInd-MeGua, MeInd-M(9EtGua)$^{n+}$ (M = Me^{+}, $Pd(NH_3)_3^{2+}$, and $Pd(NH_3)_3^{2+}$) and Me-Ind-$Pt(NH_3)_3Xan^{2+}$ (Fig 15), where methylation/metalation is at the N7 position the MeGua, were DFT optimized to compate with experimental studies of π-stacking interactions with L-Trp with analogous studies by Ferrell et al using M = $Pt(dien)^{2+}$, $Pd(dien)^{2+}$.[40, 177]

The DFT/B97-D optimized geometries of the $M(NH_3)_3(MeGua)^{2+}$ monomers and their LUMO energies were comparable to previous studies.[177] Pt(II) and Pd(II) had square planar coordination of the NH_3 and MeGua/Xan ligands[164] with a hydrogen bonding interaction between the exocyclic oxygen of Gua/Xan and an ammine ligand to produce a twist in the nucleobase relative to the $Pt/Pd(NH_3)_3$. The dihedral angle between $Pt/Pd(NH_3)_3$ and Gua/Xan, along with the Pt-N7 bond distance, was largest for $Pt(NH_3)_3(9MeGua)^{2+}$ (Fig. 15b). The addition of the Me, $Pt(NH_3)_3$, and a $Pd(NH_3)_3$ groups to MeGua lowers the LUMO energy, with metalation (Pd>Pt) having a greater effect than methylation (Table 4). The lowering of the LUMO energy of a nucleobase to reduce the relative energy with the donor's HOMO has been proposed to strengthen π-π charge-transfer interactions.[157] As a result, Farrell et al. suggested that the LUMO energy could be used to predict modified nucleobases π-stacking strength to Trp.[177] The lower the LUMO energy, the better the orbital overlap, and the stronger the interaction.[177-178]

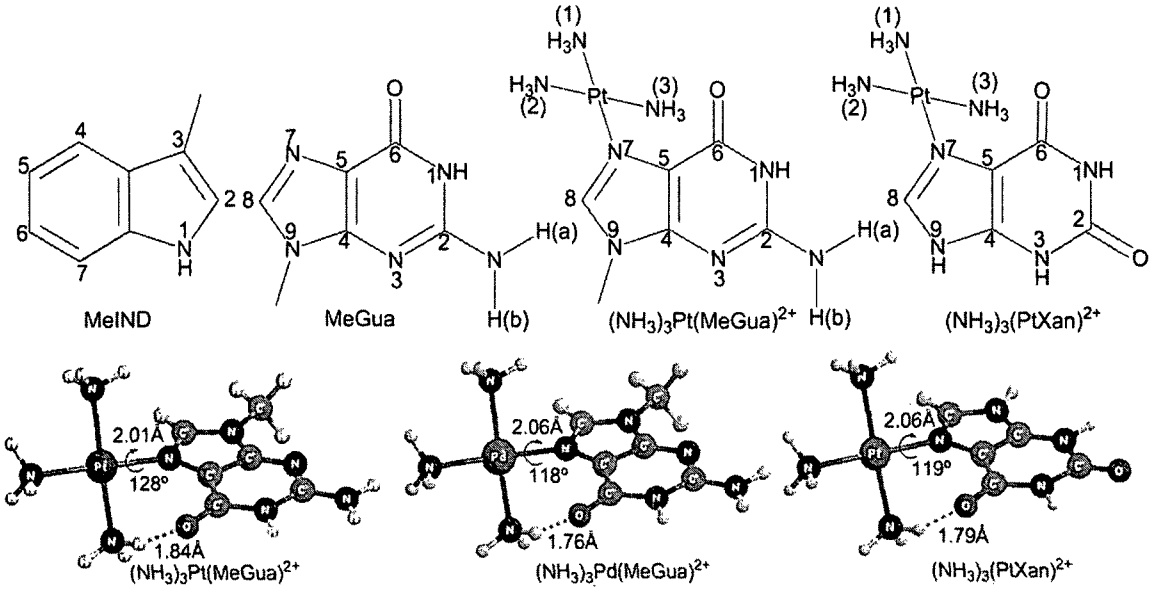

Figure 15. Structures of MeInd, methylated and metalated MeGua.(**a**) Numbering scheme for Trp, MeGua and $[Pt(NH_3)_3(9MeGua)]^{+2}$. (**b**)Optimized structures for $[Pt(NH_3)_3(9MeGua)]^{2+}$, $[Pd(NH_3)_3(9MeGua)]^{2+}$]and $[Pt(NH_3)_3Xan]^{2+}$.

Table 4. DFT optimized results for small π-stacked dimers. The LUMO and LUMO+1 energies in eV for all Gua analogues. The π-interaction energy was calculated as the difference of the dimer and monomer DFT energy. Electron donation from donor to acceptor d and back donation b (e),The experimental K_π values are for 9-Et(GH), $M(dien)9EtGH)^{2+}$ with L-Trp.M=Pt, Pd.[41]

Small Structures	LUMO Gua (eV)	LUMO+1 Gua (eV)	ΔE (kcal/mol)	d (e)	b (e)	d-b (e)	k_π (x 10^3) M^{-1}
MeInd-MeGua	-0.87	-0.03	-13.69	0.048	0.052	-0.004	3.50
MeInd-Me_2Gua^+	-5.52	-0.19	-19.74	0.080	0.035	0.046	
MeInd-$(NH_3)_3Pt(MeGua)^{2+}$	-9.36	-0.30	-26.70	0.124	0.027	0.097	7.00
MeInd-$(NH_3)_3Pd(MeGua)^{2+}$	-10.42	-0.30	-25.23	0.105	0.030	0.075	5.10
MeInd-$(NH_3)_3Pt(Xan)^{2+}$	-9.93	-0.33	-30.83	0.147	0.027	0.121	
Struct. B MeInd-$(NH_3)_3Pt(MeGua)^{2+}$	-9.36	-0.30	-27.57	0.140	0.023	0.117	

None of the DFT-optimized π-stacked structures had Gua/Xan directly eclipsed over MeInd, consistent with experimental evidence that π-stacked aromatic rings are generally displaced with respect to each other.[179] (Fig. 16). The distances between the MeInd and MeGua rings (3.3 and 3.2 Å) were slightly smaller than those found in crystal structures of Ind stacked with Gua (3.4 and 3.5 Å).[159] The addition of Me, $Pt(NH_3)_3$, and $Pd(NH_3)_3$ caused the π-stacked rings to tilt slightly away from parallel to each other so that the methylated and metalated N7 end of the purine rings are further from MeInd than the C2 end. (For example, 3.5 and 3.2 Å, respectively, for MeInd-$Pt(NH_3)_3$(MeGua)$^{2+}$, resulting in a tilt angle of 4.6°). Similarly, Rutledge et al. found a 10° tilt angle for an adenine-histidine π-stacked dimer.[180] The tilt angle between the monomer in the π-stacked structures increases from MeInd-MeGua < MeInd-Me_2Gua^{1+} < MeInd-$Pt(NH_3)_3$(MeGua)$^{2+}$ ≈ MeInd-$Pd(NH_3)_3$(9MeGua)$^{2+}$ < MeInd-$Pt(NH_3)_3$Xan^{2+}. The partial positive charge on the hydrogen atoms of the ammine ligand, are attracted to the partial negative charge of the MeInd π cloud, causing one ligand to extend down into the space between the π-stack, which may cause the rings to separate. In an aqueous solution the charges would be more diffuse and we might not see the steric interaction between the ammine ligand and the MeInd.

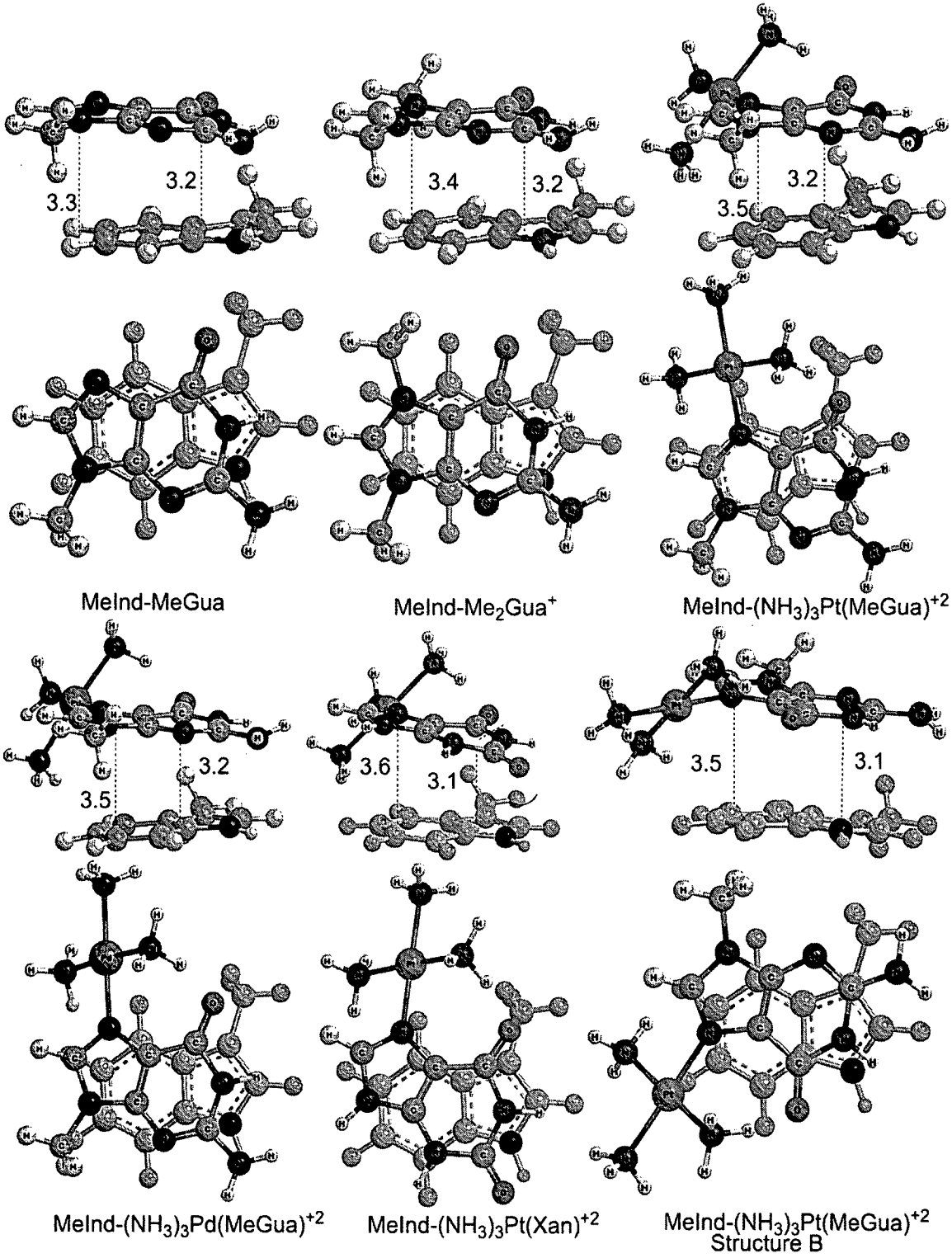

Figure 16. The DFT B97-D optimized small π-π stacked structures. The distances between monomers are in Å.

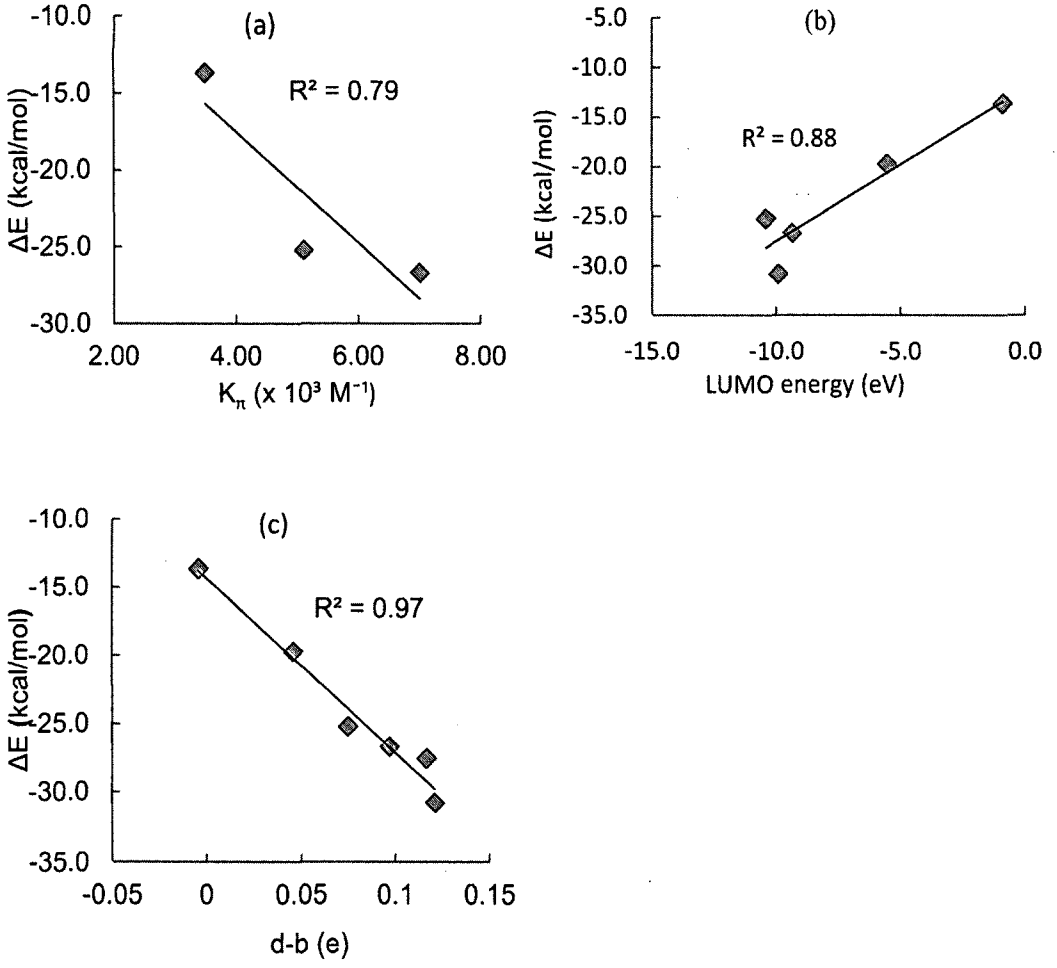

Figure 17. Correlation plots for small π-stacked structures. (a) Plot of π-stacking interaction energy as a function of the association constants, x 10^3 M^{-1} ,K_π , for L-Trp-9-EtGH, L-Trp-Pd(dien)9-EtGH)]$^{2+}$ and L-Trp-[Pt(dien)(9-EtGH)]$^{2+}$dimers. The experimental data is from Farrell et al.[41] (b) Plot of π-stacking interaction energy as a function of LUMO energy (eV) of modified Gua. (c) Plot of π-stacking interaction energy as a function of electron charge transfer.

The π-interaction energy was calculated as the relative energy of the π-complex and the separate monomers (Table 4). The addition of the Me group to MeInd-MeGua dimer enhanced the π-stacked interaction energy by 6.1 kcal/mol, whereas the addition of a $Pt(NH_3)_3$ and $Pd(NH_3)_3$ group increased the interaction by 13.0 and 11.5 kcal/mol, respectively. Substituting Gua for Xan produced an even more stable interaction (17.1 kcal/mol). The interaction energies correlate with available experimental Kπ values,[41]

supporting the use of our DFT/B97-D method for calculating π-stacking interactions (Fig. 17a). The correlation between the LUMO energies and the strength of the π-stacking interaction (Fig. 17b) suggests that the screening of potential targets through the nucleobase LUMO energy could give a quick estimation of π-stacking energy and the ability to inhibit NCp7.

Because the donor-acceptor interaction involves charge transfer from the HOMO of Trp and the LUMO of the modified Gua/Xan, CDA has been used to quantify charge relocation between fragments in the π-stacked complex.[171, 181] The net charge transfer was calculated as the difference between the electron donation from the occupied MO of the donor to the virtual MOs of acceptor (d) and back donation (b) from the acceptor to the donor (d-b). For the Trp-MeGua stack, a net 0.004e was transferred from MeGua to MeInd. For the other small π-stacked structures, the net charge transfer was from MeInd to the Gua/Xan monomer, with the largest transfer (0.12e) for Trp-$Pt(NH_3)_3Xan^{2+}$. For comparison, Tsipis and Stalikas found a net electron transfer of 0.14e for a π-stacked dimer of benzene within a trinuclear Cu(I) triiodide cluster.[181] The magnitude of the charge transfer is small (Table 4) which may suggest that it does not contribute significantly to the π-stacking energy, but there is a high positive correlation with the interaction energy, implying that charge transfer is important in π-stacking (Fig. 17c).

Larger Models

To include the effect of the surrounding residues on binding of Gua, a larger model of truncated ZF-2 of NCp7 was optimized using the ONIOM(B97-D:PM6) method to better compare with Farrell's experimental work.[40-41, 177] Although π-π interactions have been identified as the main mode of molecular recognition, the role of all intermolecular interactions, including hydrogen bonding, is important for designing molecules that target the recognition site.[152, 182] The solution structure of HIV-1 NCp7 complexed with DNA(-) primer binding site (PDB file 2EXF)[176] was truncated as illustrated in Fig 18 to make a large model of NCp-7 ZF-2 interacting with methylated and metalated MeGua and Xan. The DNA(-) primer binding site was truncated to MeGua. The protein was truncated to

residues R32 through G40 and H44 through C49. K34 and K38 were truncated to Ala and the side chain of K34 was truncated to an ethyl group. The model was divided into quantum mechanical (QM) and semiempirical (SE) regions. The QM region, indicated in Fig 18 with a ball-and-stick representation, was allowed to optimize freely. The remainder of the system, indicated by sticks was frozen and corresponded to the SE region. The largest difference in the larger model relative to the NMR solution structure of HIV-1 NCp7 complexed with DNA (-)PBS[176] was the absence of the DNA phosphate backbone which limits the binding configuration of Gua. Only the MeGua was retained in our model, since the objective of the modified Gua with its enhanced π-stacking properties is to compete with RNA and DNA for the binding to NCp7. In the NMR solution structure, the Q45 side chain (SC) NH_2 and both R32 SC NH_2 groups hydrogen bond to the phosphate backbone of DNA. In our ONIOM optimized structure, Q45 SC (=O) is hydrogen bonded to Gua NH_2 H(a) and the R32 SC NH_2 hydrogen bonds to the Gua NH_2. In the NMR structure, the K33 backbone (BB) carbonyl hydrogen bonds to Gua NH_2 H(a), but to R32 N-(H) in the ONIOM structure. M46 and W37 BB N-(H) are both H-bonded to Gua (=O) in both the NMR structure and our structure. The W37 hydrogen bond is 1.99 Å in the NMR structure and much longer in optimized structure. In the NMR structure, G35 BB (=O) is hydrogen bonded to Gua N1 H, but is too far away to H-bond in our structure (Fig. 18)

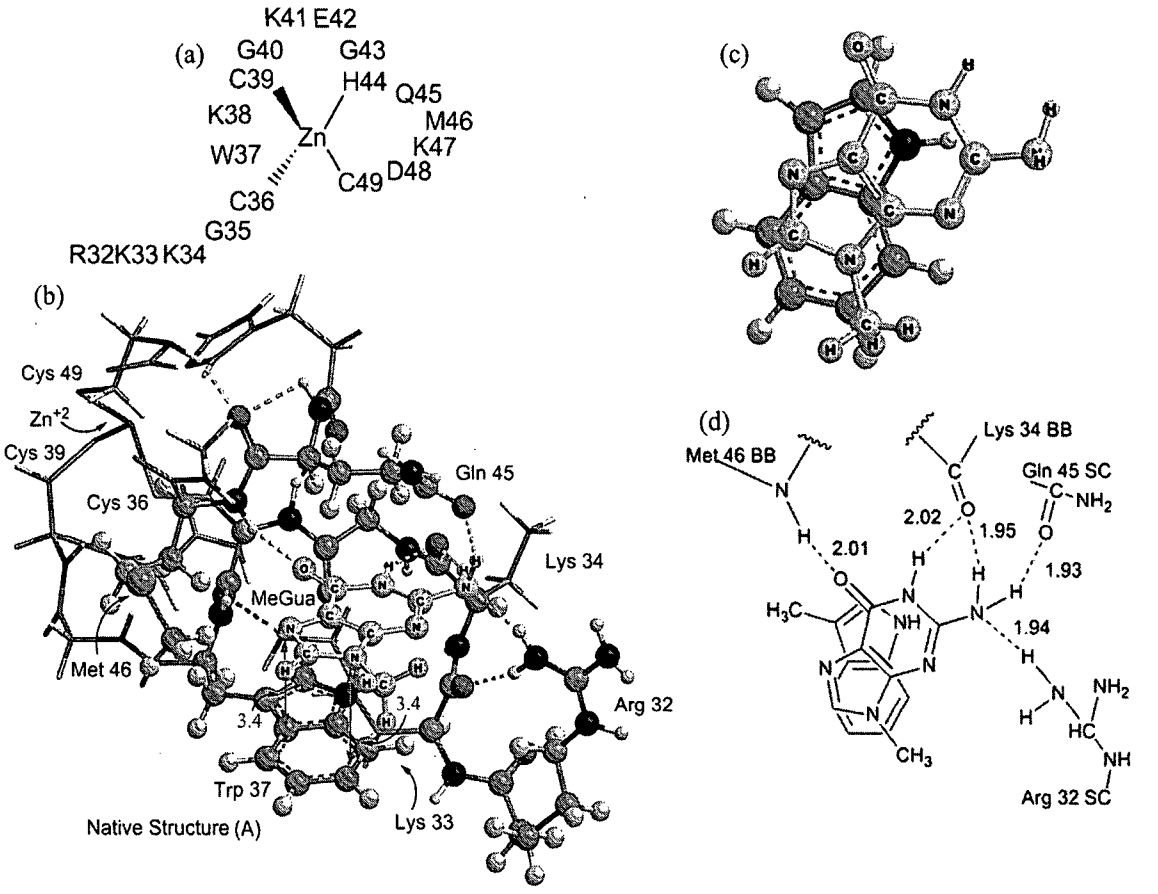

Figure 18. The truncated optimized model Structure **A** of NCp7 complexed with MeGua. Structure A. (a) The truncated optimized model of NCp7 complexed with MeGua. The truncated NCP7 finger 2 used in calculations, residues R32, K33, G35, C36, W37, C39, G40, H44, Q45, M46, and C49 were used without truncation, residues K34 and K38 were truncated to Ala, K47 was truncated to a modified Ala with ethyl group and residues K41, E42, G43 and D48 were eliminated. (b) ONIOM optimized Native structure. Ball and stick representations correspond to the QM region, stick representation correspond to the SE region. (c) The π-stacking interaction of structure A. (d) The hydrogen bonding interactions structure A. Bond lengths are given in Å.

(a)

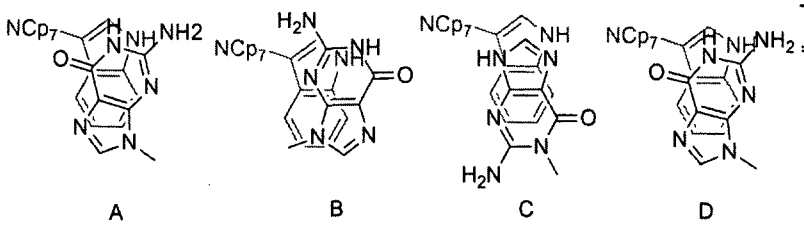

(b)

	Relative energy kcal/mol
A	6.22
B	0.00
C	15.69
D	11.67

Figure 19. Orientaitons of structures **A-D** with relative energies. (a) Different orientations of Gua in the binding site. (b) The relative energies of the four different orientations of MeGua in the binding site of NCp7. Structure **B** was set to zero.

Since the modified Gua is not limited by the DNA backbone, it could π-stack with Trp in orientations different from the native **A** conformation. We optimized the Gua in three addition orientations in the truncated NCp7 binding site. In **A**, the 6-member ring of Gua is over the 5-member ring of Trp with the NH_2 group over N1 of Trp. For **B**, the Gua is flipped such that the exocyclic oxygen of Gua is over N1 of Trp. For **C**, N7 of Gua is over N1 of Trp and N1 of Gua is over N1 of Trp in **D** (Fig. 19a). These four orientations of MeGua affects not only the nature of the π-stacking interaction, but also on the number and type of hydrogen bonding interactions (Fig. 19b). Structure **B** was the most stable conformation followed by the native structure **A** (+6.2 kcal/mol), **D** (11.7 kcal/mol) and **C** (+15.7 kcal/mol). To quantify the effect of the hydrogen bonding interactions on Gau binding, the relative strength of donor acceptor energies ($\Delta E_{d\rightarrow a}$) of the H-bond species was calculated by NBO analysis and by WBIs. The NPA charges on, and the distance between, the H-bond donor and acceptor were recorded (Table 5) to evaluate how these parameters effect the strength of the interaction, and the increased and decreased strength is observed in both $\Delta E_{d\rightarrow a}$ and the WBIs.

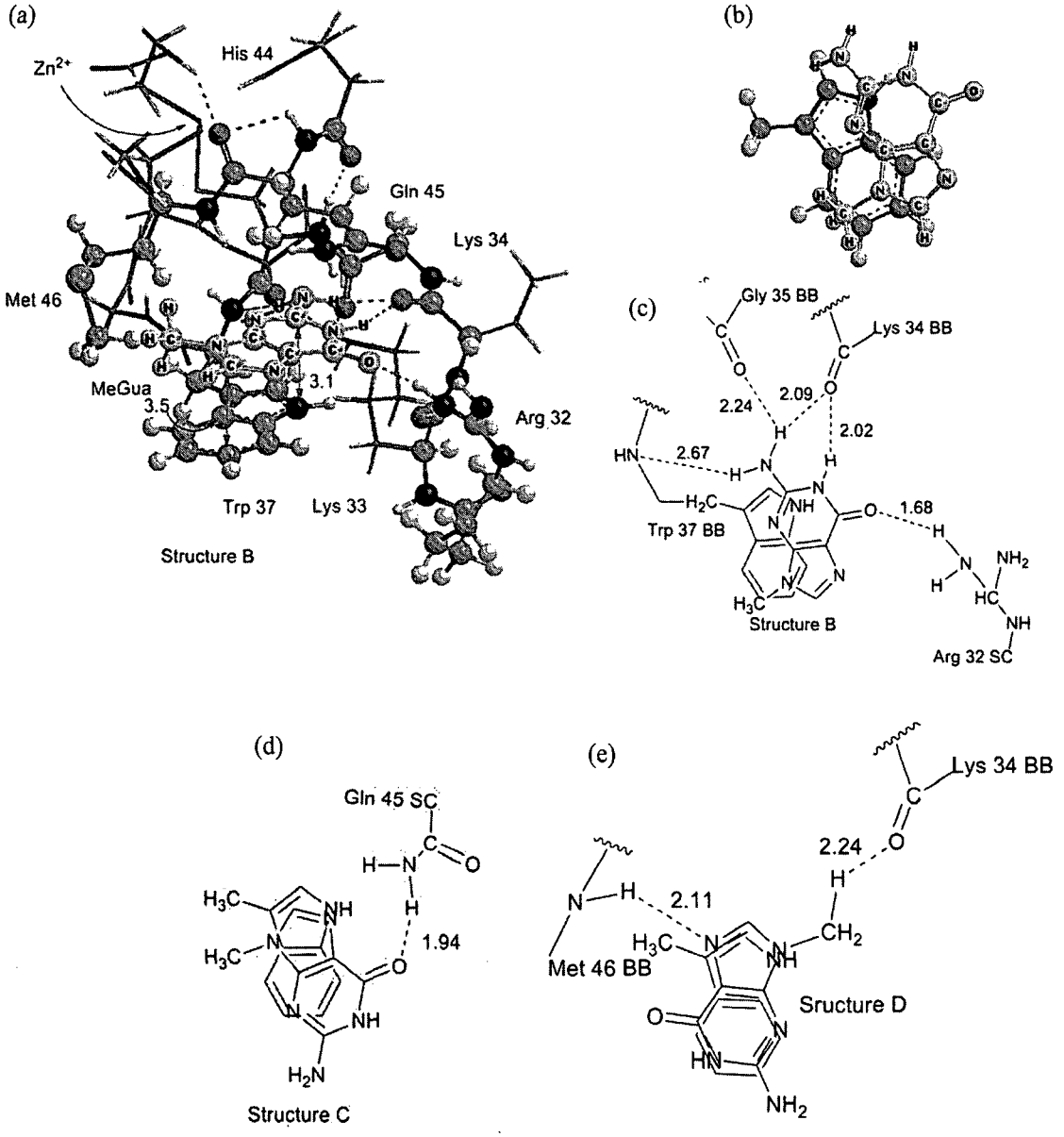

Figure 20. Hydrogen bonding interactions in structures **B-D**. (a) Truncated optimized model **B**. (b) The π-stacking interaction in **B**. (c) Hydrogen bonds in **B**. (d) Hydrogen bonds in **C**. (e) Hydrogen bonds in **D**.

The relative energy of **A**-**D** should be related to the number and strength of the their H-bonding interactions (Fig 20, Table 5). The stronger bound **A** and **B** both have 5 H-bonding interactions, whereas the weaker **C** and **D** had only 1 and 3 H-bonding interactions, respectively. Structure **B** was 6.2 kcal/mol more tightly bound in the binding site than **A**. H-bonds **2** and **3**, of **B**, involve the same donor and acceptor but are longer and weaker than those in **A**. The strongest H-bond in **A** is H-bond (**5**) between MeGua NH_2 (N) and R32 SC N-(H) the N-H distance was 1.9 Å. For **B**, The strongest H-bond of **B,** Hydrogen bond (**1**) is also with R32, but in this orientation it is MeGua =O pointing toward R32, with an O-H distance of 1.7 Å. This short distance produces a strong H bond. **B** also has 2 weak H-bonds to W37 BB (N) and G35 BB (O=). Collectively, the H-bond ($\Delta E_{d\rightarrow a}$) was lower in **B** than **A** by 10.4 kcal/mol and the total WBIs were lower by 0.06. The tighter binding of **B** compared to **A** is from stronger π-stacking interactions. A small model of MeInd-Pt$(NH_3)_3$(MeGau) in the orientation of Structure **B** was optimized and found to be more stable that structure **A** with Pt$(NH_3)_3$, which demonstrates that structure **B** has stronger π-stacking interactions than **A**. The $\Delta E_{d\rightarrow a}$ of each H-bond in each structure **A** through **D** has a high correlation to the WBI revealing that $\Delta E_{d\rightarrow a}$ energy is a good estimation of the bonding strength. The difference in the charges of the donor and acceptors divided by the distance between them correlates well with $\Delta E_{d\rightarrow a}$ demonstrating that H-bond strength is augmented by an increase of charge separation of donor and acceptor and decreases as the distance between them is lengthened. (Fig. 21)

Table 5. ONIOM(B97-D:PM6) results for structures A-D. NPA charges of hydrogen bond donors and acceptors, distances between hydrogen bond donorand acceptors in Å, WBI between the hydrogen bond donor and acceptor, the difference between the charges of the donor and acceptor, and the difference between the charges of the donor and acceptor divided by the distance between them (e/Å).

	Donor	NPA q_D (e)	Acceptor	NPA q_A (e)	Interaction type	d(D-A) (Å)	$\Delta E_{d\rightarrow a}$ kcal/mol	WBI	$q_D - q_A$ (e)	$\frac{q_D - q_A}{d}$
	Native Structure									
1	MeGua (=O)	-0.704	M46 BB N-(H)	0.421	H-Bond	2.01	8.16	0.032	-1.125	-0.560
2	K34 BB (=O)	-0.714	MeGua N-(H)	0.451	H-Bond	2.02	6.84	0.026	-1.165	-0.577
3	K34 BB (=O)	-0.714	MeGua NH_2 H(a)	0.416	H-Bond	1.95	10.52	0.038	-1.130	-0.579
4	Q45 SC (=O)	-0.699	MeGua NH_2 H(b)	0.442	H-Bond	1.93	11.38	0.041	-1.141	-0.591
5	MeGua NH_2 (N)	-0.948	R32 SC N-(H)	0.447	H-Bond	1.94	17.04	0.071	-1.395	-0.719
	Structure B									
1	MeGua (=O)	-0.707	R32 SC N (H)	0.452	H-Bond	1.68	26.84	0.089	-1.159	-0.690
2	K34 BB (=O)	-0.710	MeGua N1 (H)	0.460	H-Bond	2.02	7.13	0.025	-1.170	-0.579
3	K34 BB (=O)	-0.710	MeGua NH_2 H(a)	0.425	H-Bond	2.09	5.88	0.022	-1.135	-0.543
4	W37 BB (N)	-0.705	MeGua NH_2 H(b)	0.422	H-Bond	2.67	1.32	0.007	-1.127	-0.422
5	G35 BB (=O)	-0.691	MeGua NH2 H(a)	0.425	H-Bond	2.24	2.36	0.007	-1.116	-0.498
	Structure C									
1	MeGua (=O)	-0.688	Q45 SC N (H)	0.427	H-Bond	1.94	11.75	0.042	-1.115	-0.575
	Structure D									
1	MeGua (N7)	-0.586	M46 BB N (H)	0.418	H-Bond	2.11	7.9	0.032	-1.004	-0.476
2	MeGua (N7)	-0.586	W37 BB N (H)	0.418	H-Bond	2.44	2.37	0.012	-1.004	-0.411
3	K34 BB (=O)	-0.662	MeGua CH_3 (H)	0.242	O··H-C Bond	2.24	2.51	0.009	-0.903	-0.403

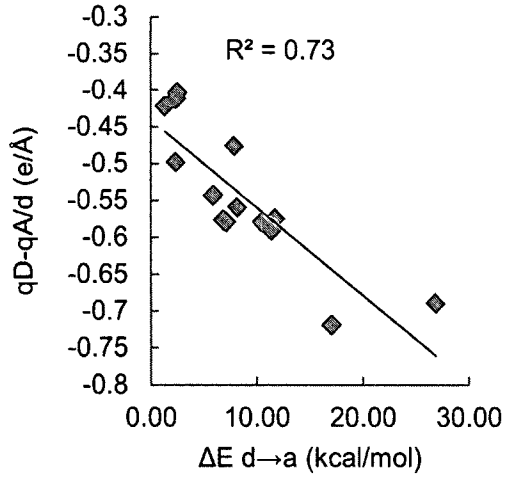

Figure 21. Plot of $\Delta E_{d\rightarrow a}$ (kcal/mol) as a function of TWBI for all H-bonding interactions in **A**, **B**, **C** and **D** large models.

Table 6. ONIOM(B97-D:PM6) results for methylated and platinated MeGua bound to NCp7 model. NPA charges of hydrogen bond donors and acceptors (e), distances between hydrogen bond donor and acceptors in Å, WBI between the hydrogen bond donor and acceptor, the difference between the charges of the donor and acceptor, and the differnce between the charges of the donor and acceptor divided by the distance between them (e/Å).

	Donor	NPA q_D (e)	Acceptor	NPA q_A (e)	Interaction type	d(D-A) (Å)	$\Delta E_{d\to a}$ kcal/mol	WBI	$q_D - q_A$ (e)	$\frac{q_D - q_A}{d}$
	Native NCp7 with Me_2Gua^+									
1	Me_2Gua (=O)	-0.691	M46 BB N (H)	0.397	H-Bond	2.26	2.54	0.012	-1.09	-0.48
2	Me_2Gua (=O)	-0.691	W37 BB N (H)	0.416	H-Bond	2.08	5.66	0.022	-1.11	-0.53
3	G35 BB (=O)	-0.770	Me_2Gua N (H)	0.465	H-Bond	1.75	20.92	0.062	-1.23	-0.71
4	G35 BB (=O)	-0.770	Me_2Gua NH_2 H(a)	0.420	H-Bond	2.12	5.51	0.024	-1.19	-0.56
5	Q45 SC (=O)	-0.685	Me_2Gua NH_2 H(b)	0.445	H-Bond	1.87	14.68	0.057	-1.13	-0.60
6	Me_2Gua (=O)	-0.691	M46 SC C (H)	0.220	O··H-C Bond	2.13	1.97	0.008	-0.91	-0.43
	Native NCp7 with $(NH_3)_3Pt(MeGua)^{2+}$									
1	PtMeGua (=O)	-0.722	W37 BB N (H)	0.409	H-Bond	2.1	5.95	0.023	-1.131	-0.538
2	G35 BB (=O)	-0.778	PtMeGua N1 (H)	0.462	H-Bond	1.81	16.65	0.054	-1.240	-0.685
3	G35 BB (=O)	-0.778	PtMeGua NH_2 H(a)	0.422	H-Bond	2.05	6.93	0.028	-1.200	-0.585
4	Q45 SC (=O)	-0.685	PtMeGua NH_2 H(b)	0.449	H-Bond	1.84	17.12	0.064	-1.135	-0.617
5	M46 SC (S)	0.065	PtMeGua(NH_3(3)) (H)	0.420	S··H-N Bond	2.23	16.05	0.084	-0.355	-0.159
6	PtMeGua (=O)	-0.722	M46 BB N (H)	0.404	H-Bond	2.31	1.85	0.011	-1.126	-0.488
7	PtMeGua (=O)	-0.722	M46 SC C (H)	0.211	O··H-C Bond	2.23	1.46	0.005	-0.933	-0.418
8	PtMeGua (=O)	-0.722	PtMeGua(NH_3(3)) (H)	0.444	H-Bond*	2.40	0.74	0.007	-1.166	-0.485
	Native NCp7 with $(NH_3)_3Pd(MeGua)^{2+}$									
1	PdMeGua (=O)	-0.722	W37 BB N (H)	0.407	H-Bond	2.17	4.31	0.019	-1.129	-0.521
2	G35 BB (=O)	-0.778	PtMeGua N1 (H)	0.462	H-Bond	1.84	16.27	0.049	-1.240	-0.675
3	G35 BB (=O)	-0.778	PtMeGua NH_2 H(a)	0.422	H-Bond	2.00	8.89	0.032	-1.200	-0.599
4	Q45 SC (=O)	-0.685	PtMeGua NH_2 H(b)	0.449	H-Bond	1.84	17.37	0.065	-1.135	-0.618
5	M46 SC (S)	0.071	PtMeGua(NH_3(2)) (H)	0.422	S··H-N bond	2.29	10.72	0.062	-0.352	-0.153
6	M46 SC (S)	0.071	PtMeGua(NH_3(1)) (H)	0.417	S··H-N bond	2.26	14.13	0.076	-0.346	-0.153
7	PdMeGua (=O)	-0.722	M46 SC C (H)	0.422	O··H-C bond	2.22	1.51	0.005	-1.144	-0.515
8	PdMeGua (=O)	-0.722	PtMeGua(NH_3(3)) (H)	0.439	H-Bond*	2.37	0.82	0.008	-1.161	-0.490
	Native NCp7 with $(NH_3)_3Pt(Xan)^{2+}$									
1	PtXan C6 (=O)	-0.684	M46 BB N (H)	0.447	H-Bond	2.25	2.7	0.012	-1.131	-0.503
2	PtXan C6 (=O)	-0.684	W37 BB N (H)	0.408	H-Bond	2.23	3.7	0.013	-1.092	-0.489
3	G35 BB (=O)	-0.762	PtXan N1 (H)	0.481	H-Bond	1.74	22.4	0.065	-1.243	-0.714
4	M46 SC (S)	0.070	PtXan(NH_3(3)) (H)	0.421	S··H-N Bond	2.21	15.5	0.088	-0.351	-0.159
5	M46 SC (S)	0.070	PtXan(NH_3(1)) (H)	0.420	S··H-N Bond	2.19	15.3	0.089	-0.351	-0.160
6	PtXan C6 (=O)	-0.684	PtXan(NH_3(3)) (H)	0.447	H-Bond*	2.42	1.2	0.007	-1.131	-0.467

Structure A was further explored by methylation and metalation of Gua in the four orientations (Table 6, Fig. 22). Only **A** and **B** had the $Pt(NH_3)_3$ fragment added, because **C** and **D** could not accept the $Pt(NH_3)_3$ fragment due to steric constrants. Binding of $Pt(NH_3)_{3(}Xan)^{2+}$ was also modeled. Our goal was to see how methylation and metalation affects the H-bonds and to see whether the $Pt(NH_3)_3$ fragment could fit in the binding site in a different conformation. It is our hypothesis that the increased positive charge on the Gua fragment increase its hydrogen bonding strength. The relative energy of the methylated and metalated NCp7 models was calculated with equation 42, as the difference in energy of the products and reactants.

NCp7-MeGua + Me/Pt/Pd$(NH_3)_3$MeGua/Xan^{2+} →

NCp7-Me/Pt/Pd$(NH_3)_3$MeGua/Xan^{2+} + MeGua (42)

We were surprised that in our large model binding of Me_2Gua^+ was only 1.14 kcal/mol more stable than MeGua, since addition of a methyl group to MeGua in the small models strengthened its π-stacking interaction to MeInd by 6.1 kcal/mol. The total H-bond $\Delta E_{d\rightarrow a}$ was 7.7 kcal/mol lower, and WBI totals were 0.023 lower for Me_2Gua than the Native NCp7 model, despite the fact that Me_2Gua^+ has six H-bonds relative to native (**A**) NCp7 model's five (Table 6). The Me_2Gua^+ is rotated in the binding pocket relative to **A** NCp7, so that the strongest H-bond (**5**) for the Native NCp7 model is no longer present in Me_2Gua's structure. H-bond **1** for Me_2Gua is the same as **1** for the NCp7 **A** model, but is further away and weaker. We suggest that the majority of the increase in π-stacking strength we saw in the small models was lost in the larger models due to the reduction of the H-bonding strength.

The addition of $Pt(NH_3)_3$ to the native structure increased its stabilty by 35.2 kcal/mol. In the Pt NCp7 structure the purine and indole rings have a 9.5° tilt angles between the rings, with the largest separation near the $Pt(NH_3)_3$ fragment, similar to the small models. In the Pt stuctures, the sum of the H-bond ($\Delta E_{d\rightarrow a}$) was 12.8 higher than in Native NCp7 structure. Like the Me_2Gua^+ structure, the Gua ring is twisted in respect to the Native so that H-bond **1** is longer and weaker than the native. The H-bond to Q45 is much closer and stronger than in the Native NCp7 structure. The gain of 12.8 kcal/mol

appears to come from the $Pt(NH_3)_3$'s interaction with M46's divalent sulfur, which accounts for 16.1 kcal/mol of total ($\Delta E_{d\rightarrow a}$). Our hypothesis that the H's from $Pt(NH_3)_3$ $MeGua^{2+}$ would be more positively charged and have stronger H-bonding interactions did not appear to be the case.

The NCp7-$(NH_3)_3$PdMeGua^{2+} and NCp7-$(NH_3)_3$Pt(Xan)$^{2+}$ structures were similar to the Pt analogue and their H-bonds **1-5** were comparable. Even with an increased total H-bond $\Delta E_{d\rightarrow a}$ of 7.2 kcal/mol over the Pt structure, the Pd structure was 5.2 kcal/mol less stable than the Pt analogue, which we assume is from a weaker π-stacking interaction. NCp7-$(NH_3)_3$Pt(Xan)$^{2+}$ had a relative energy that was similar to NCp7-$(NH_3)_3$PtMeGua^{2+}, but the total $\Delta E_{d\rightarrow a}$ was less than the Pt-Gua analogue by 5.95 kcal/mol. The replacement of NH_2 in Gua for =O in Xan, leads to less H-bonding interactions. We suggest that the lower H-bonding interactions were offset by a stronger π-stacking interaction.

NCp7-Structure B $PtGua^{2+}$ (Table 7, Fig. 23) had total $\Delta E_{d\rightarrow a}$ comparable to the Native Pt/Pd structures but was less stable than the Native by 4.31 kcal/mol. We believe is from the unfavorable repulsive coulomb interactions between the positive Pd fragment and the nearby positively charged Q45. The relative energies of the methylated and metalated large structures are in Fig. 24.

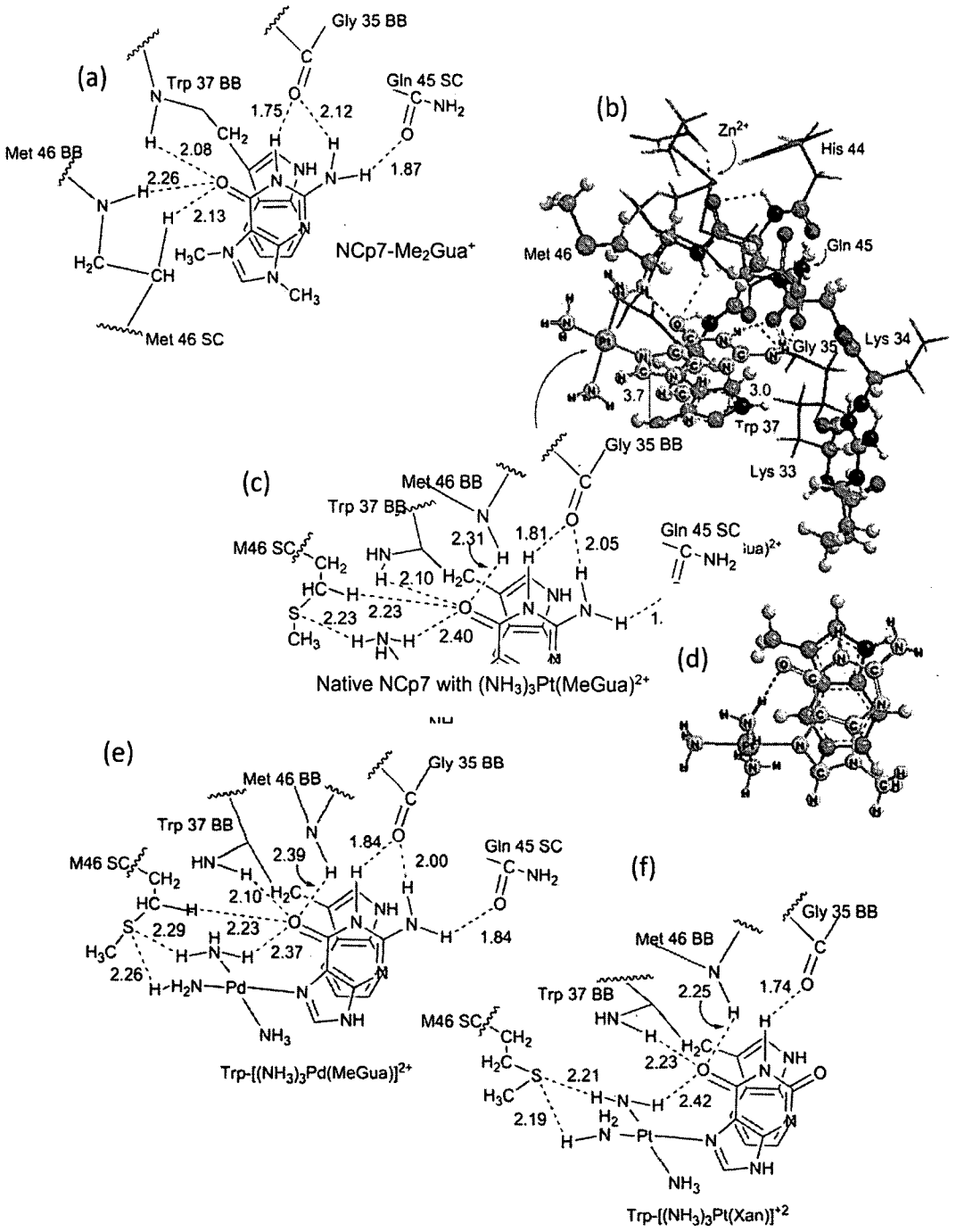

Figure 22. Bonding interactions for methylated and metalated nucleobases bound to NCp7 model. (a) Hydrogen bonding interactions for NCp7-Me2Gua^{+}. (b) ONIOM(B97-D/PM6)-optimized structure of NCp7 model with $(NH_3)_3Pt(MeGua)^{2+}$ (c) Hydrogen bonding interactions for $(NH_3)_3Pt(MeGua)^{2+}$ with NCp7 model. (d) π-stacking interaction only for Native NCp7 with $(NH_3)_3Pt(MeGua)^{2+}$.(e) Hydrogen bonding interactions for NCp7-$(NH_3)_3Pd(MeGua)^{2+}$ (f) Native NCp7 with NH3)3Pt(Xan)$^{2+}$.

Table 7. ONIOM(B97-D:PM6) results for platanated structure Pt. NPA charges of hydrogen bond donors and acceptors (e), distances between hydrogen bond donor and acceptors in Å, WBI between the hydrogen bond donor and acceptor, the difference between the charges of the donor and acceptor, and the differnce between the charges of the donor and acceptor divided by the distance between them (e/Å), for structure B.

	Donor	NPA q_D (e)	Acceptor	NPA q_A (e)	Interaction type	d(D-A) (Å)	$\Delta E_{d\rightarrow a}$ kcal/mol	WBI	$q_D - q_A$ (e)	$\frac{q_D - q_A}{d}$
	Structure B	NCp7	with $(NH_3)_3Pt(MeGua)^{2+}$							
1	PtMeGua (N3)	-0.629	M46 SC N (H)	0.410	H-Bond	2.41	2.87	0.012	-1.039	-0.431
2	K34 BB (=O)	-0.738	PtMeGua NH_2 H(a)	0.440	H-Bond	1.82	18.29	0.058	-1.178	-0.647
3	K34 BB (=O)	-0.738	PtMeGua N1 (H)	0.462	H-Bond	2.22	3.48	0.016	-1.200	-0.542
4	G35 BB (=O)	-0.692	PtMeGua NH_2 H(b)	0.433	H-Bond	2.48	1.22	0.004	-1.126	-0.453
5	Q45 SC (=O)	-0.750	PtMeGua (NH_3(3))(H)	0.466	H-Bond	1.79	17.69	0.060	-1.216	-0.678
6	PtMeGua (=O)	-0.720	R32 SC N (H)	0.438	H-Bond	2.49	1.33	0.009	-1.158	-0.466
7	PtMeGua (=O)	-0.720	PtMeGua (NH_3(3))(H)	0.452	H-Bond*	2.49	13.55	0.055	-1.172	-0.471

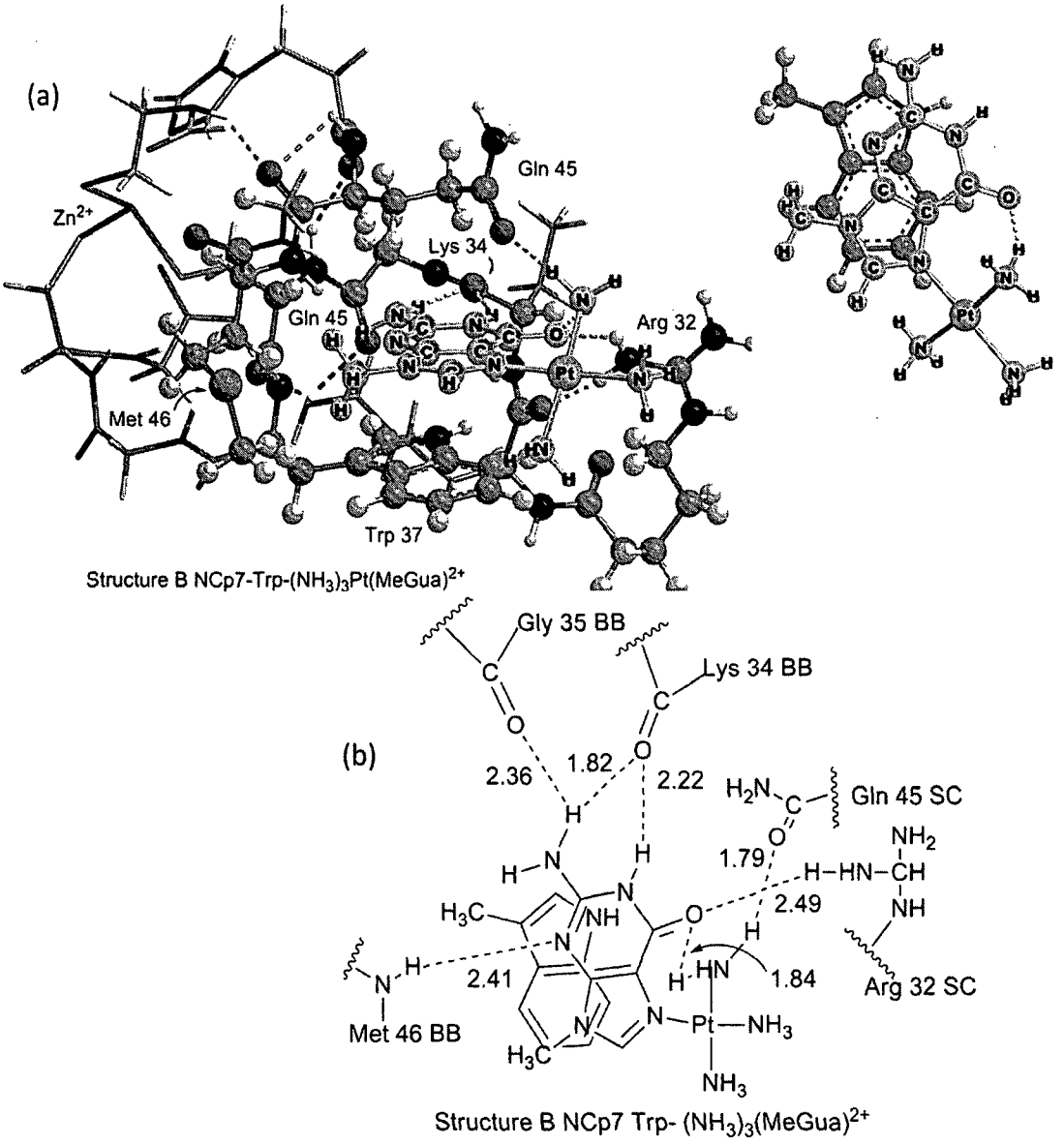

Figure 23. Bonding interactions for $(NH_3)_3Pt(MeGua)^{2+}$ Structure **B** with NCp7 model. (a) ONIOM(B97-D/PM6)-optimized structure of NCp7 model with $(NH_3)_3Pt(MeGua)^{2+}$ structure **B**. (b) Hydrogen bonding interactions for $(NH_3)_3Pt(MeGua)^{2+}$ structure B with NCp7 model.

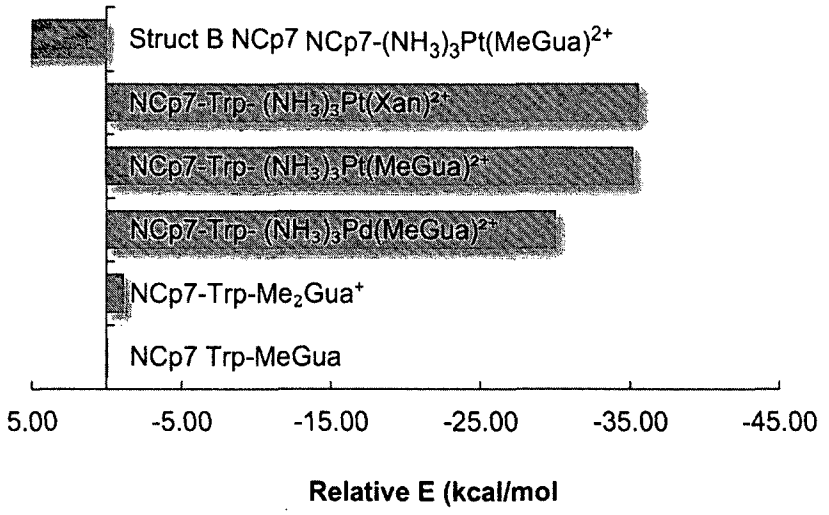

Figure 24. Relative bonding energies for methylated and metalated nucleobases. NCp7-Trp-MeGau was set to 0.0.

Conclusions

Concentrating on the Trp-Gua interaction of the NCp7-DNA adduct represents a selective and novel approach to NCp7 inhibitor design. The correlation of the LUMO energy, from the modified nucleobases in our small model study, with both the Kπ values as well as the DFT π-stacking energy shows that there is promise in using frontier orbital energies of the individual monomers to predict π-stacking interactions with methylated and metalated nucleobases with MeInd. The results from our study showing that metalated MeGua had a stronger π-stacking interaction with MeInd than either MeGua or Me_2Gua reinforces the idea that metalation is analogous to methylation, and that the π-stacking interactions are enhanced from the lowering of the LUMO energy of the positively charged metalated nucleobase. The strong correlation between the π-stacking energy and the amount of charge transfer bolsters the idea that the increased interaction between the modified MeGua and MeInd is the result of greater charge transfer. For the larger models the idea that the increased charge on the modified MeGua would be distributed over the entire molecule and lead to stronger H-bonding interactions was not verified by our results. The largest increase in H-bonding interactions appeared to be from

the hydrogens in the NH_3 ligands interacting with the sulfur from Met46. Although π-stacking interactions are considered the main mode of the MeGua binding in binding site in NCp7, the importance of other interactions was demonstrated by the study with the larger models. For example, structure **B** had the strongest π-stacking interaction to the truncated NCp7, compared to structures **A**, **C** and D. A small model of MeGua with added $Pt(NH_3)_3$ in the orientation of Structure **B**, was optimized and found to be more stable that structure **A** with $Pt(NH_3)_3$, which demonstrates that structure **B** has stronger π-stacking interactions than **A**. This suggested that platinated **B** in the NCp7 binding site in the large model would be more tightly bound than platinated **A**. When the relative energy was calculated for $(NH_3)_3$PtMeGua-structure **B** in the large model, it surprisingly had the weakest interaction, due to the unfavorable electrostatics from the nearby Q45. Thus, unfavorable interactions can occur when molecules involved in molecular recognition events are modified artificially. The overall results from this study show that using the LUMO energy of modified nucleobases can give a good first estimate of the π-stacking strength to Trp. This idea can be expanded to include other nucleobases with aromatic amino acid for applications to other π-stacking molecular recognition events.

CHAPTER 4

ORBITAL-BASED INSIGHTS INTO PARALLEL-DISPLACED AND TWISTED CONFORMATION IN π-π INTERACTIONS

Introduction

π-stacking interactions stabilize protein and DNA structures,[183-186] influence molecular recognition,[185] direct the self-assembly of crystals and host–guest systems,[187-188] and influence the design of organic electronics.[189] The benzene[190-194] and pyridine[195] dimers along with DNA base stacks[196-197] are important examples of π–π stacking interactions. Theoretical studies of the benzene dimer and its derivatives show that a parallel-displaced (PD) structure, commonly observed in crystal structures of aromatic compounds, is favored over the sandwich (S).[190-194] There are conflicting explanations as to why the PD is lower in energy than the sandwich. Early discussions by Hunter and Sanders explained that σ attractions between the positive σ framework and the negative π electron density outweigh the π–π repulsions when the monomers are offset.[198] More recently, dispersion has been argued as the major contributor to π–π interactions,[190, 192] but it is not clear why the S structure, believed to maximize dispersion, is not the most stable conformer.[193] Alternatively, the quadrupole–quadrupole interaction is expected to be the most attractive in the PD structure,[199] but aromatics with negligible quadrupole moments, such as 1,3,5-trifluorobenzene, also form PD stacks.[200] For π-stacked DNA bases, the dependence on the twist angle as well as parallel displacement,[201] is believed to arise from electrostatics and the dipole–dipole attraction.[201-202]

Lutz, P. B.; Bayse, C. A., Orbital-based insights into parallel-displaced and twisted conformations in π-π interactions. *Phys. Chem. Chem. Phys.* **2013,** *15* (23), 9397-9406.- Reproduced by permission of the PCCP Owner Societies.Despite being invoked in donor–acceptor π–π interactions,[177, 189, 203-207] orbital interactions are discussed abstractly, through energy decompositions[26] or as perturbations of the π cloud[195] and

have been largely discounted as an explanation of π-stacking and other noncovalent interactions.[199, 208]

As a result, an in-depth molecular orbital (MO) analysis of π-stacking interactions has yet to be explored. In this chapter, we use density-functional theory (DFT) calculations to suggest that the preference for PD and TW structures in the dimers of benzene (Bz_2), pyridine (Pyr_2), cytosine (Cyt_2) and several polyaromatic hydrocarbons (PAH) can be traced to shifts in the character of combinations of the monomer MOs.

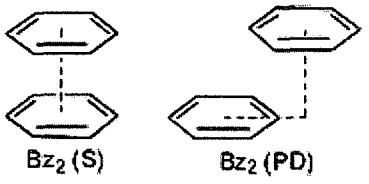

Theoretical methods

The vertical and slip distances for the Bz_2, Pyr_2 and Cyt_2 dimers were optimized using Zhao and Turhlar's M06-2X[209], SVWN[57, 210], and B97-D[166] xc functionals and the aug-cc-pVTZ[68] basis set within the Gaussian 09 software package.[97] Dimers of naphthalene, anthracene and tetracene were optimized using Dimers of naphthalene, anthracene and tetracene were optimized using M06-2X functional and Dunning's split-valence triple-ζ basis set augmented with polarization functions (TZVP).[69] Within the dimers, monomer geometries were fixed at optimized structures determined at the same level of theory as the dimers and constrained to be planar and parallel. Two-electron integrals were calculated numerically using a grid of 99 radial shells with 590 angular points per shell (an 'ultrafine' grid in Gaussian 09). Use of the coarser 'fine' (default) Gaussian 09 grid does not significantly change the qualitative results of the study. Contributions to the intermolecular interaction energies were calculated as a function of the horizontal slip distance (R_{slip}) using density-fitting DFT-based symmetry-adapted perturbation theory (DF-DFT-SAPT),[211-212] method which produces interaction energies comparable to high-

level ab initio methods at lower computational cost.

$$E_{int} = E^{(1)}_{pol} + E^{(1)}_{exch} + E^{(2)}_{ind} + E^{(2)}_{disp} + E^{(2)}_{ind\text{-}exch} + E^{(2)}_{exch\text{-}disp} + \delta(HF) \quad (43)$$

In DF-DFT-SAPT, the intermolecular interaction (E_{int}, eqn (43)) between monomers is decomposed into first, second, and higher order corrections (δ(HF)). The first-order contributions include electrostatics ($E^{(1)}_{pol}$) and exchange-repulsion ($E^{(1)}_{exch}$). The second-order contributions are composed of induction ($E^{(2)}_{ind}$), which includes charge transfer, induction exchange ($E^{(2)}_{ind\text{-}exch}$), dispersion ($E^{(2)}_{disp}$), and dispersion exchange ($E^{(2)}_{exch\text{-}disp}$). DF-DFT-SAPT[211] calculations were performed on the DFT(M06-2X) optimized structures using MOLPRO[212] and aug-cc-pVTZ-quality basis sets for the atomic orbitals and the auxiliary JK and MP2 fitting basis sets. Monomer densities were calculated using the asymptotic corrected PBE0 functional at the aug-cc-pVTZ level. Orbital analyses and Wiberg bond orders were generated at the DFT(M06-2X)/aug-cc-pVTZ or DFT(M06-2X)/TZVP (PAH dimers only) level.

Results and discussion

Prior to presenting an orbital analysis of π-stacked systems, we review the contributions to the stacking interaction using a highly-accurate DF-DFT-SAPT method. Contributions to the interaction energy E_{int} (Fig. 25) were determined for a series of Bz_2 structures in which the inter-ring distance (R_{vert}) was optimized with R_{slip} constrained at 0–4 Å using the M06-2X exchange–correlation (xc) functional and Dunning's augmented correlation-consistent triple-ζ basis set (aug-cc-pVTZ). This combination of xc functional and basis set has been found to correlate well to high-level complete basis set coupled-cluster calculations of a test set of noncovalent dimers.[213] The DFT(M06-2X)/aug-cc-pVTZ minimum energy PD structure (ΔE = −2.6 kcal mol^{-1}, R_{slip} = 1.70 Å; R_{vert} = 3.39 Å) is consistent with results calculated using the SVWN and B97-D functionals (Fig. 25a) as well as experimental values (−1.6[214] and −2.4[215] kcal mol^{-1}) and previous high-level theoretical results.[190-191, 216] Because R_{vert} is optimized at each R_{slip} value, the distance between the rings decreases by 0.37 Å as they slide away from the optimized S structure (R_{vert} = 3.76 Å; see Fig. 25b), a feature not observed in most other theoretical accounts in which R_{vert}

is frozen. Allowing R_{vert} to optimize provides a different perspective on the contributions to the energy in eqn (43). In contrast to previous studies which find the extrema of the energy components at S when R_{vert} is constrained to 3.3 Å,[217] the attractive $E^{(1)}_{pol}$, $E^{(2)}_{disp}$, and $E^{(2)}_{ind}$ and repulsive $E^{(1)}_{exch}$, $E^{(2)}_{exch\text{-}disp}$ and $E^{(2)}_{ind\text{-}exch}$ contributions are minimized and maximized, respectively, at the optimal PD structure (Fig. 25c). Although the overall E_{int} is a smooth function of R_{slip}, the individual contributions are influenced by R_{vert}; the shoulders between 1.0–1.5 Å in Fig. 25c may be attributed to variations in R_{vert} due to effects of the C2′ and C3 atoms slipping over one another. The trend in the DF-DFT-SAPT E_{int} relative to R_{vert} (Fig. 25d) shows that the increase in the interaction energy from the S to the PD structure is accompanied by a sharp decrease in R_{vert}. Further decrease in R_{vert} occurs as the monomers begin to move past one another beyond the PD structure.

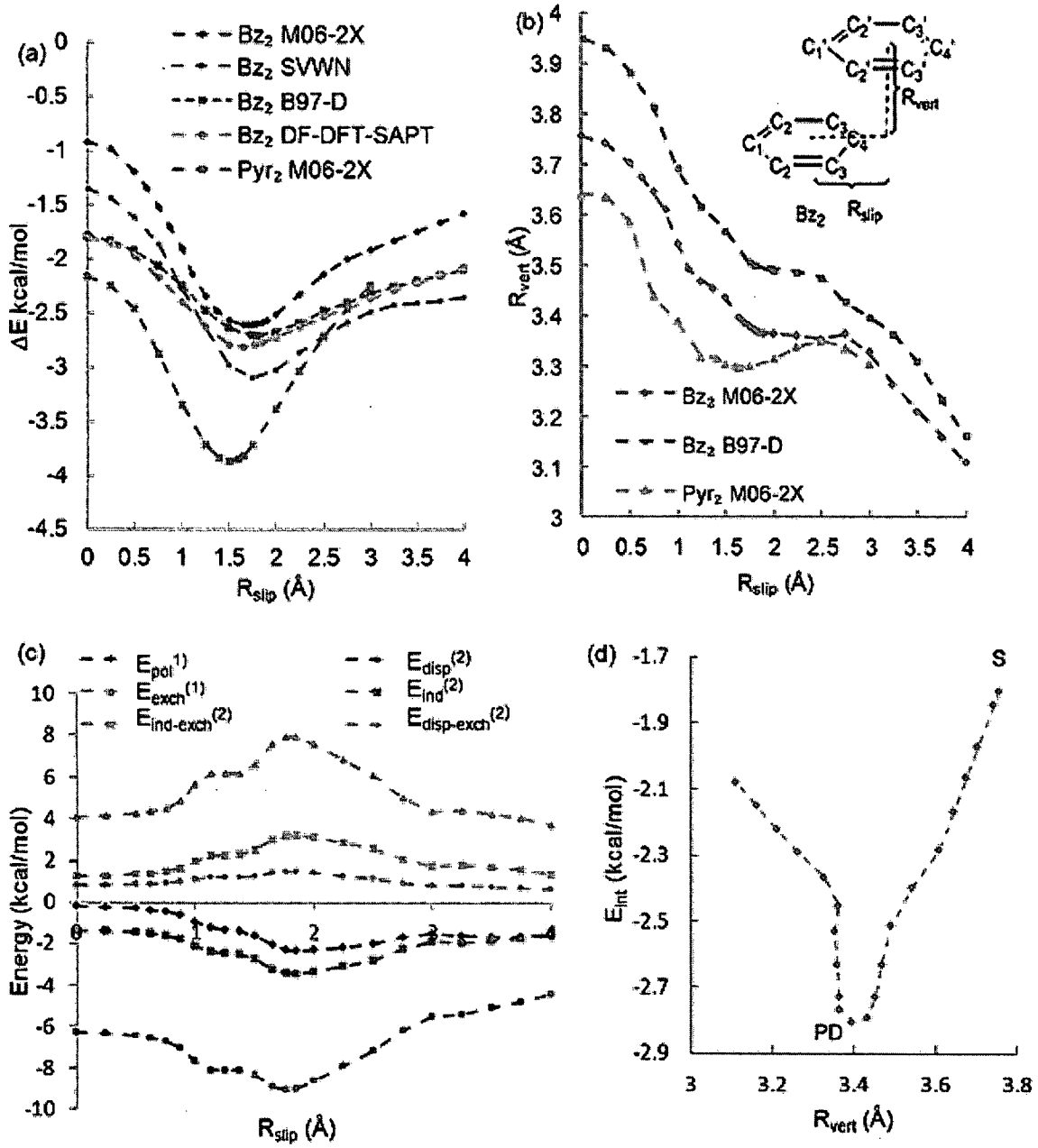

Figure 25. Correlation plots for Bz_2 and Pyr_2.(a) Potential energy curves for Bz_2 and Pyr_2 calculated with various xc functionals and DF-DFT-SAPT (Bz_2 only) as a function of R_{slip} in (Å). (b) Plot of R_{vert} as a function of R_{slip} in Å for Bz_2 and Pyr_2. (c) Contributions to the Bz_2 interaction energy as calculated by DF-DFT-SAPT as a function of R_{slip}. (d) DF-DFT-SAPT E_{int} values plotted as a function of R_{vert}.

The maximization of the contributions to E_{int} at the PD R_{slip} value is important in terms of the conventional wisdom that dispersion is greatest at the S structure due to the maximal, face-to-face overlap of the π clouds. However, this expectation is likely to be

true only on a potential energy curve where the inter-ring distance is fixed. When the S structure is fixed at the PD R_{vert} value (3.4 Å), the dispersion is larger than either the PD or the optimal S structures (Table 8), but this attactive contribution (−11.53 kcal mol^{-1}) is more than cancelled out by the repulsive $E^{(1)}_{exch}$ term (12.60 kcal mol^{-1}). In the optimized S structure, the dispersion is necessarily lower than that of the PD structure because the longer inter-ring distance (3.76 Å) required to reduce the repulsive terms in eqn (43) results in a significant decrease in the overlap of the π clouds. For this reason, we hesitate to single out the importance of the dispersion over other terms in eqn (43) as these terms are not necessarily independent and small changes potentially have a significant effect on the overall magnitude of E_{int}. For example, comparison of the S and PD results (Table 8 shows that the increase in $E^{(1)}_{exch}$ (+3.12 kcal mol^{-1}) from S to PD more than cancels the decrease in $E^{(2)}_{disp}$ (−2.36 kcal mol^{-1}). These differences, as well as most other contributions to E_{int}, are greater in magnitude than the actual difference in E_{int} between S and PD (−1 kcal mol^{-1}). In other words, the dispersion is the largest attractive term at PD, but one cannot clearly trace the PD structure to any individual change in the energy contributions to eqn (43) and we can only conclude from the DF-DFT-SAPT calculations that the PD structure is preferred energetically, but not why this is true.

Table 8. Contributions to the DF-DFT-SAPT interaction energy E_{int} (kcal mol^{-1}) for the S and PD structures of the benzene dimer[a]

DF-DFT SAPT	S(R_{vert}=3.76 Å)	PD(R_{vert}=3.39 Å	S(R_{vert}=3.39 Å)
$E^{(1)}_{pol}$	-0.26	-2.05 (-1.79)	-2.95
$E^{(1)}_{exch}$	4.27	7.39 (+3.12)	12.6
$E^{(2)}_{ind}$	-1.46	-3.14 (-1.68)	-4.9
$E^{(2)}_{ind\text{-}exch}$	1.33	2.95 (+1.62)	4.77
$E^{(2)}_{disp}$	-6.4	-8.76 (-2.33)	-11.53
$E^{(2)}_{disp\text{-}exch}$	0.84	1.40 (+0.64)	2.11
E_{int}	-1.79	-2.82	-0.26

[a] Values in parentheses are relative to the optimal S structure (Rvert=3.76 Å)

Orbital interactions in Bz_2

Although the DF-DFT-SAPT calculations show that extrema in E_{int} and its components occur at the optimal PD structure, they do not provide a clear or intuitive explanation for why the PD structure is preferred. In our attempt to understand the preference for PD in Bz_2, we noted curious features in the dimer molecular orbitals (MOs) and the Walsh diagram of the DFT(M06-2X)/aug-cc-pVTZ Kohn–Sham orbital energies constructed as a function of R_{slip} (Fig. 26a). By invoking a Walsh diagram, we view the Bz_2 dimer as a single entity (rather than two interacting monomers) in order to trace the observed geometric perturbations to mixing of the dimer MOs. At the S structure, the π-type Bz MOs (π_A, π_B, π_C) combine to create three pairs of in-phase, or bonding (π_A^+, π_B^+, π_C^+), and out-of-phase, or antibonding (π_A^-, π_B^-, π_C^-), dimer MOs. However, as R_{slip} increases, π_B^+ and π_B^-, well separated in the S structure, increase and decrease in energy, respectively, and cross at roughly the optimal PD structure (R_{slip} = 1.70 Å). The character of these MOs changes significantly as R_{slip} is increased (Fig. 26b): (a) for π_B^-, the out-of-phase antibonding combination of the monomer MOs convert to an in-phase bonding interaction; (b) the initially in-phase lobes of monomer MOs in π_B^+ MO slide over the opposite ring's nodes to become antibonding at long R_{slip}. At the PD structure, both of these MOs have net bonding character (Fig. 26b). Other Bz_2 MOs, including the π_C^+ and π_C^- π-type MOs, the bonding and antibonding MOs (π_A^+ and π_A^-) formed from the monomer π_A MO, as well as the σ framework, do not change significantly as R_{slip} is altered. The pattern and appearance of the Walsh diagram and the Bz_2 MOs is consistent over a range of methods and xc functionals (SVWN, B97-D, MP2,‡etc.) using both large and small basis sets.

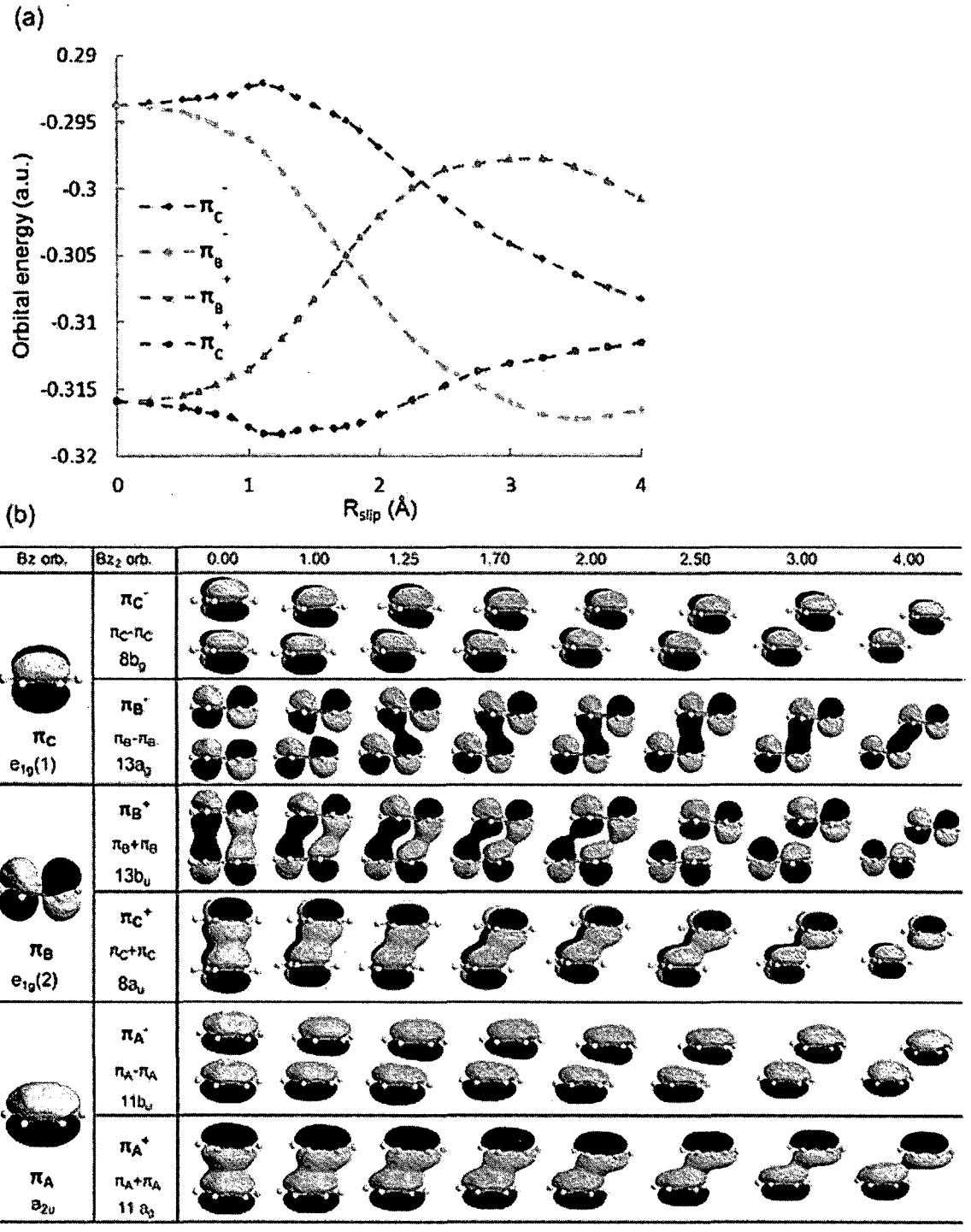

Figure 26. Walsh diagram and orbital representation of Bz2 slip. (a) Walsh diagram of the top four molecular orbital energies of Bz_2 plotted as a function of R_{slip}. (b) Representations of the six π-type dimer MOs (C_{2h} symmetry) of Bz_2 as a function of R_{slip}. The isosurface value is 0.010.

The location of the minimum near the crossing point of π_B^+ and π_B^- is reminiscent of the Walsh rule which states that a molecule will assume a geometry that best stabilizes the highest occupied molecular orbital (HOMO) or the next highest MO if there is no significant change in the HOMO.[218] The crossing point represents the lowest energy of HOMO-1 MOs; π_B^- before and π_B^+ after the minimum. Given that these MOs have net bonding character at the point where ΔE is minimized, the preference for the PD structure can be rationalized qualitatively through a stack bond order (SBO) which we introduce as the sum of the bonding and antibonding π-type MOs in direct analogy to the bond order in covalent MO theory. Our SBO is intended to count the occupation of bonding/antibonding MOs and not to assign a quantitative value to the bonding. When R_{slip} is zero (S), there are an equal number of occupied bonding and antibonding π-type MOs resulting in an SBO of zero for a net repulsive interaction that forces the rings beyond the sum of the van der Waals radii. The conversion of π_B^- to bonding at the PD structure, combined with no overall change in the bonding character of the other MOs, increases the SBO to two for a net attractive interaction. This prediction of an attractive interaction is consistent with the shorter PD R_{vert} value relative to S. In terms of the DF-DFT-SAPT data, we could interpret this increase in inter-ring bonding character as leading to an enhancement of the dispersion, polarization and other attractive contributions to E_{int} while the shortened inter-ring distance leads to maxima in the repulsive contributions.

This MO analysis suggests that orbital interactions exert an underlying influence on the parallel-displacement of π-stacked rings. However, the role of orbital interactions in π-stacking interactions is often discounted because the overlap is small.[208] Considering that non-covalent interactions are weaker than covalent bonds by one to two orders of magnitude, it is not surprising that the overlap would be small. Other than the weakness of the interaction, there is no reason to assume that the MOs of these systems could not mix in a similar fashion as the MOs that make up covalent bonds. Indeed, the Walsh diagram retains many of the features that would be expected for the

geometry-dependence of a covalent bond. To quantify the π–π interaction in terms of orbital contributions, intermolecular Wiberg bond indices (WBI_{AB}),[105] calculated as the sum of the squares of the inter-ring contributions to the M06-2x/aug-cc-pVTZ density (P_{ij}, eqn (44)), were determined as a function of R_{slip} (Fig. 27a).

$$B_{AB}^{Wiberg} = \sum_{s\in A}\sum_{t\in B} P_{st}^2 \tag{44}$$

$$WBI_{tot} = \sum WBI_{AB} \tag{45}$$

Because P_{ij} is derived from the atomic orbital coefficients of the Kohn–Sham MOs, the WBI_{AB} values are a direct measure of MO interactions between the monomer rings. The individual atom–atom WBI_{AB} values are small, roughly two-to-three orders of magnitude less than a covalent bond, as would be expected for a weak intermolecular interaction that is a fraction of typical covalent bond dissociation energies. As shown in Fig. 27a, the total inter-ring WBI (WBI_{tot}, eqn (45)) is maximized at the optimal R_{slip} distance with the largest contribution coming from the C3–C2′ terms due to the increase in net bonding character in the π_B^- MO. These results are consistent with inter-ring critical points found in Bader analysis of PD Bz_2[219] and surfaces of enhanced density in the inter-ring region identified by reduced gradient analysis.[220] We note that the maximum in WBI_{tot} is highly sensitive to the inter-ring distance, basis set, xc functional and the size of the numerical integration grid. The M06-2X xc functional with a minimum triple-ζ quality basis set with diffuse and multiple high-angular momentum polarization functions (e.g., aug-cc-pVTZ or TZV2P++) that properly represents the inter-ring region are required to find the maximum WBI_{tot} at the PD structure. More limited basis sets (e.g., TZVP, 6311+g*) as well as DFT functionals that do not adequately describe the dispersion[221] (SVWN) skew the maximum in the WBI_{tot} away from the minimum energy structure and should not be used for WBI analysis.

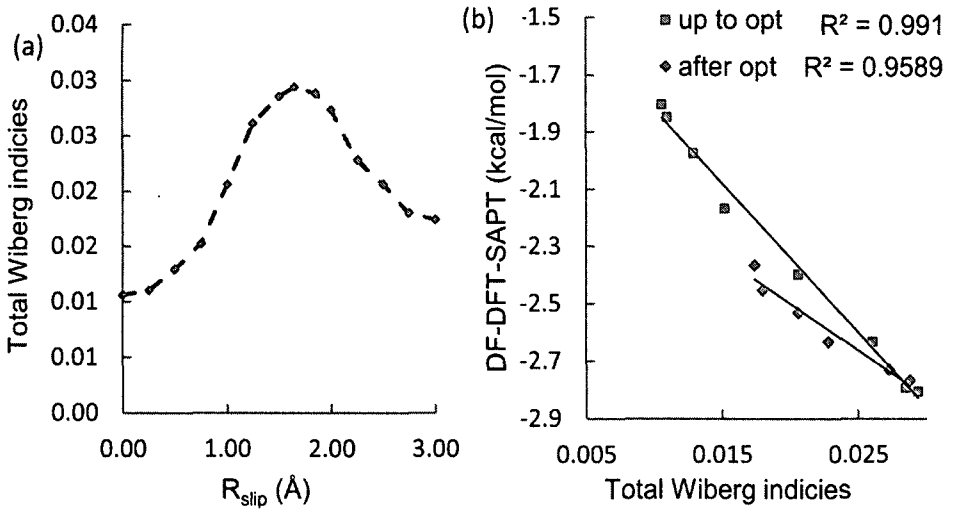

Figure 27. WBI correlations for Bz_2. (a) Total inter-ring WBI plotted as a function of R_{slip} for Bz_2. (b) DF-DFT-SAPT E_{int} for Bz_2 plotted as a function of the total inter-ring WBI.

The strong correlation between the total WBI and E_{int} (R^2 = 0.94, Fig. 27b) reinforces the case for orbital interactions contributing to the preference for a PD structure in Bz_2. Generally, these plots have a different slope before and after the PD minimum which is consistent with the change in the dimer MO with the greatest bonding character (π_B^+ before PD, π_B^- after PD). The correlation shown in these plots are consistent with the dependence of each of the SAPT terms on charge overlap effects, or the interaction of the monomer charge densities.[222] As shown in the dimer MO representations, the PD structure occurs in the region where the monomers are aligned for a net bonding interaction (SBO > zero) between certain monomer MOs. We speculate that the arrangement of the monomers in this fashion contributes to more favorable overlap of the monomer charge density, or maximizes inter-penetration of the π clouds, in the SAPT calculation resulting in the extrema shown in 25c.

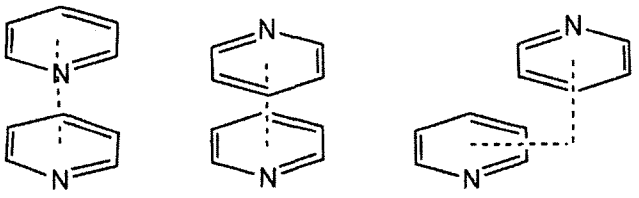

Pyr_2 (S) Pyr_2 (TW) Pyr_2 (TW-PD)

Orbital interactions in Pyr_2

A similar analysis of the lowest energy Pyr_2 conformation found by Sherrill,[13] was performed to determine if the trends in the orbital analysis could be found in other π-stacked systems. The monomers were arranged with opposing dipoles and allowed to slide over the bond perpendicular to the dipole axis (TW) which is 1.3 kcal mol^{-1} more stable than the S conformation (CCSD(T)/aug-cc-pVTZ).[195] The optimized DFT(M06-2X)/aug-cc-pVTZ TW-PD dimer (R_{vert} = 3.3 Å; R_{slip} = 1.50 Å) and its binding energy (ΔE = −3.9 kcal mol^{-1}) are consistent with Sherrill's results (SCS-MP2/aug-cc-pVTZ: ΔE = −3.8 kcal mol^{-1}; R_{vert} = 3.4 Å; R_{slip} = 1.6 Å).[195] The trend in MO character and the Walsh diagram of the highest energy MOs as a function of R_{slip} each produce a similar pattern to Bz_2 (compare Fig. 25 and 27). The TW as well as the S structures (not shown) have equal numbers of occupied bonding and antibonding π-type MO (SBO = zero). The two highest π-type MOs (π_F^+ and π_F^-), constructed from linear combinations of the π_F monomer MO and corresponding to the π_B^+ and π_B^- MOs of Bz_2, increase and decrease their bonding and antibonding character, respectively, to cross near the optimal R_{slip}. Deviations from purely π-type character for these MOs is due to mixing with the Pyr lone pair (lp) MOs of the same irreducible representation. The π_E^+ and π_E^- MOs lie below these MOs and maintain their antibonding and bonding character, respectively, over the range of R_{slip}. The π_D^+ and π_D^- MOs constructed from the Pyr MO analogous to π_A of Bz are lower in energy and do not change character over the range of R_{slip}.

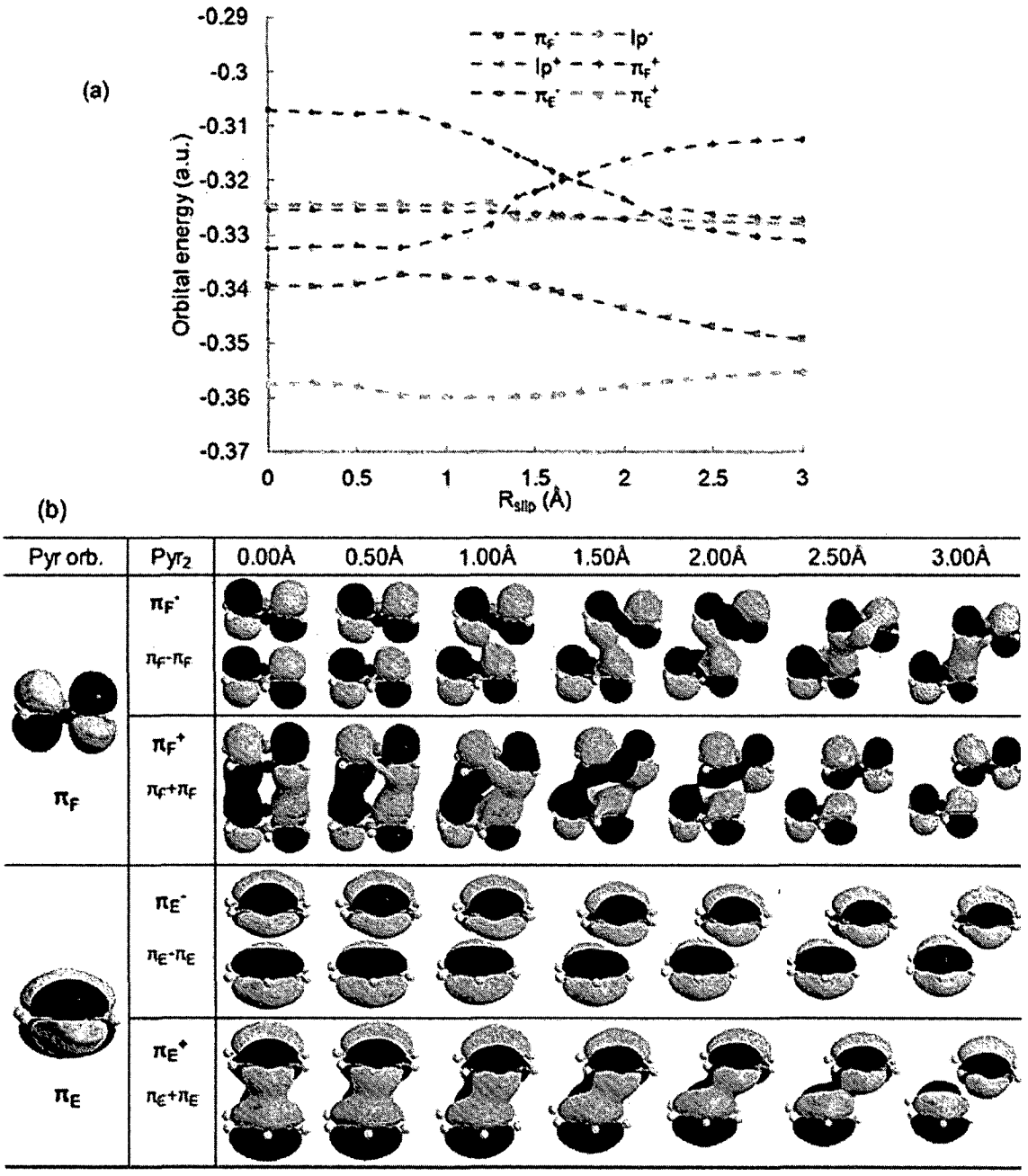

Figure 28. Walsh diagram and orbital representations for Pyr_2. (a) Walsh diagram of top six dimer MO energies of Pyr_2 plotted as a function of R_{slip}. Note the avoided crossings of π_F^+ and lp^- at 1.4 Å and lp^+ and π_F^- at 2.2 Å. (b) Representations of the top four π-type dimer MOs of Pyr_2 as a function of R_{slip}. The isosurface value is 0.010.

The minimum TW-PD structure is found in the region where π_F^- has been converted to a bonding interaction and all other MOs maintain their character for a qualitative SBO of two. Unlike Bz_2, the minimum energy structure does not occur at the crossing point of the critical MOs suggesting that the relative MO energies themselves are not as important as the bonding/antibonding characters of these MOs. The inter-ring WBI_{tot} is maximized at the optimal TW-PD structure (Fig. 29), suggesting again that the shift in the character of π–π orbital interactions to a SBO greater than zero is crucial to the π-stacking interaction. The largest contributions to WBI_{tot} are for the atoms making up the overlapping N=C–C=C fragments of the rings, consistent with the largest contributions to the stacking energy calculated by Hirshfeld partitioning of the MP2 energy for the analogous over-bond PD benzene dimer.[223]

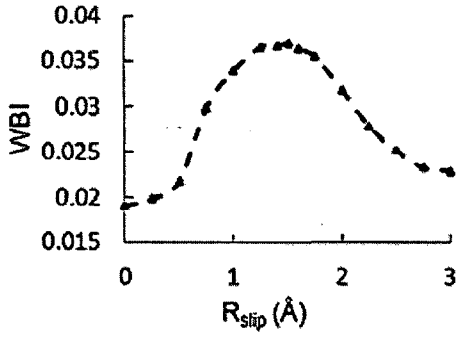

Figure 29. Total inter-ring WBI plotted as a function of R_{slip} for Pyr_2.

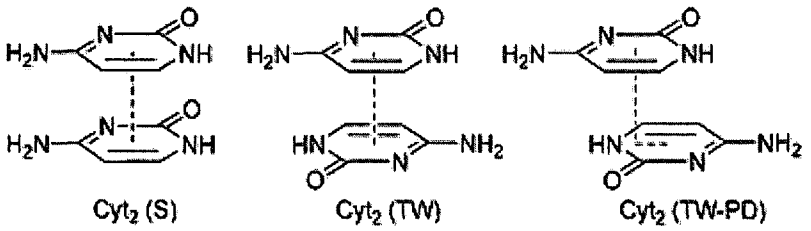

Orbital interactions in Cyt_2

Stacked dimers of purine and pyrimidine rings tend to be twisted as well as parallel-displaced with respect to their center of mass. Theoretical models[201] typically find the π-stacked Cyt_2 dimer twisted by 180° relative to S. The DFT(M06-2X)/aug-cc-pVTZ optimized structure of S Cyt_2 is unbound by 2.4 kcal mol^{-1} with the monomers separated by 4.5 Å, a large separation partially attributed to electrostatic repulsions within the dimer. In S Cyt_2, the π-type MOs of Cyt combine into five filled pairs of bonding and antibonding dimer MOs (SBO = zero) further contributing to the repulsive interaction. Inspection of these MOs shows that there is little inter-ring mixing of the in-phase monomer combinations due to the large R_{vert}. Twisting the rings by 180° (TW) around the center-of-mass reduces the electrostatic repulsions[20] and realigns the monomer MOs such that π_G^- (HOMO, Fig. 30) is converted from antibonding to bonding character at TW with no net change in the SBO of the remaining π-type MOs .The more favorable electrostatics and this change in the number of bonding MOs (six bonding, four antibonding; SBO = two) leads to a significant decrease in R_{vert} (3.2 Å) and increase in the energy of dimer formation (ΔE = −9.2 kcal mol^{-1}). This inter-ring distance and interaction energy is consistent with previous computational studies.[201, 224-226] Allowing the rings to slip (TW-PD) further increases the in-phase bonding interaction in π_G^- and converts π_H^- to bonding (seven bonding, three antibonding; SBO = four; Fig. 30 to strengthen π-stacking (ΔE = −10.0 kcal mol^{-1}) and draw the rings closer together (R_{slip} = 0.6 Å; R_{vert} = 3.15 Å). This MO is reminiscent of the HOMO of the guanine dimer proposed to contribute to the band structure of DNA molecular wires.[227] A Walsh diagram (Fig. 31a) shows that the TW-PD structure occurs near the crossing point of these MOs and the inter-ring WBI_{tot} is maximized at the optimal R_{slip} (Fig. 31b) relative to S, the intermolecular density increases

by 400% upon rotating the rings by (180° and 600% at the optimal R_{slip} as measured by the WBI_{tot}. These increases are greater than for Bz_2 and Pyr_2 partially due to the greater repulsive electrostatic contribution at the Cyt_2 S structure, yet confirm a picture of π-stacking as the enhancement of the net bonding character of the stack MOs.

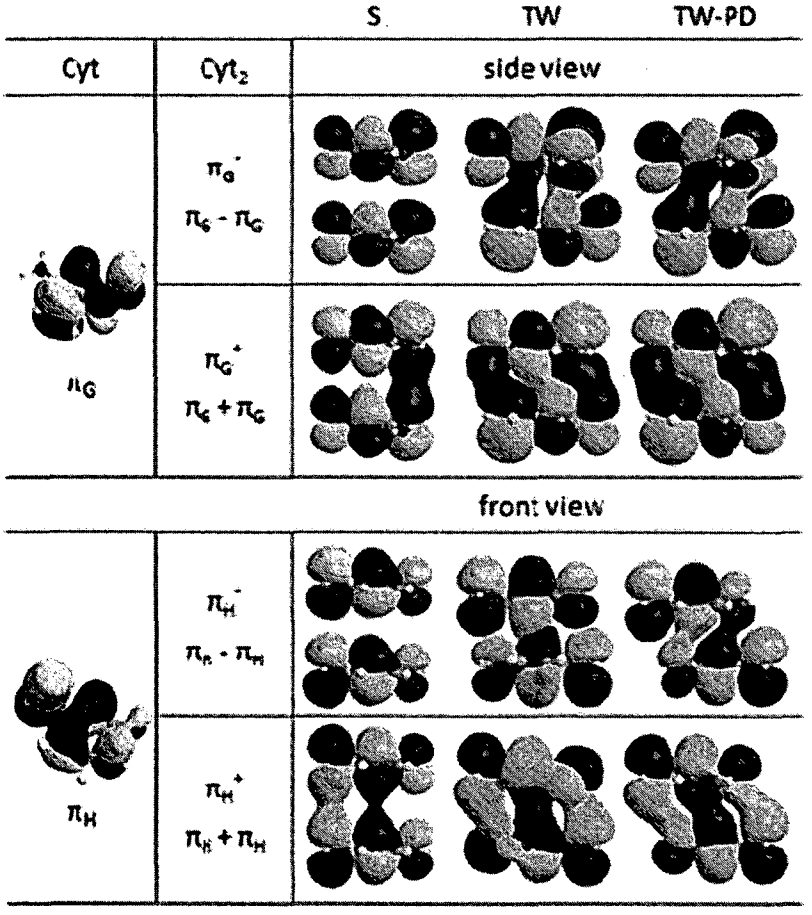

Figure 30. Representations of the top four π-type dimer MOs for Cyt_2. The isosurface value is 0.01.

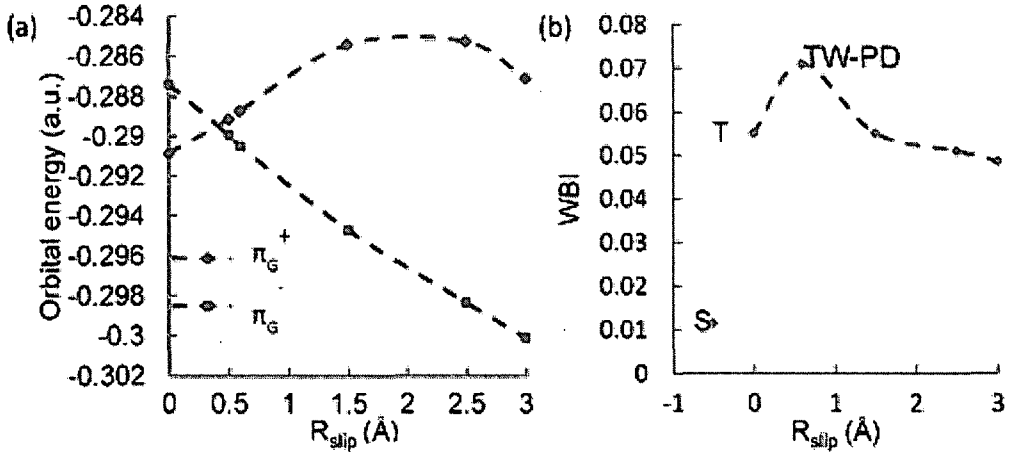

Figure 31. (a) Walsh diagram and Total inter-ring WBI for Cyt_2. Walsh diagram of the top two MO energies of Cyt_2 as a function. (b) Total inter-ring WBI as a function of R_{slip} for Cyt_2.

Orbital interactions in PAH dimers

The larger π-stacked systems of naphthalene, anthracene and tetracene dimers (1, 2 and 3, resp.) also show similar patterns of orbital interaction (Fig. 32) and have S and PD structures and energies (DFT(M06-2X)/TZVP) that are in good agreement with previous studies (Table 9).[208, 228-232] The PD structures are allowed to slip in both the x and y directions relative to R_{vert} (z) and tend to orient themselves such that half of the tertiary carbon atoms lie in the center of the other ring (i.e., graphite-like, Fig. 33). As expected, the MOs of the S dimers have the same pattern of zero SBO, whereas the PD structures convert most of the S antibonding MOs to MOs with some inter-ring overlap (e.g., $\pi_{1\text{-}B}^-$, $\pi_{1\text{-}C}^-$, $\pi_{1\text{-}D}^-$, and $\pi_{1\text{-}E}^-$ for naphthalene, see Fig. 32) for a non-zero SBO. As the number of fused rings in the PAHs increases, the number of dimer MOs with bonding character also increases. These MOs have varying degrees of bonding character (and some may be better classified as nonbonding (e.g., $\pi_{1\text{-}E}^-$, $\pi_{2\text{-}G}^-$, $\pi_{3\text{-}I}^-$), but the dimer MO constructed from the monomer MO with the most nodes coplanar with the short axis of the molecule appears to gain the most bonding character upon PD (e.g., $\pi_{1\text{-}D}^-$, $\pi_{2\text{-}F}^-$, $\pi_{3\text{-}H}^-$). The in-phase and out-of-phase combinations of these monomer MOs also become similar in energy (not shown). Although the bonding character in other dimer out-of-phase-type MOs is counterbalanced by a reduction in the bonding character of the in-phase-type MOs

(compare for example the $\pi_{2\text{-}E}^{+}$ MOs) upon parallel displacement, the overall enhancement of the inter-ring density (as reflected in WBI_{tot}) allows these rings to come closer together and become more tightly bonded (Fig. 32c–d). In contrast, only allowing the rings to slip in the x direction as shown for the anthracene dimer 2 leads to a conformation (2-PD_x) more stable than 2-S, but 2 kcal mol^{-1} higher in energy than the PD structure. Note that the 2-PD_x MOs with a node coplanar with the long axis of the monomer do not form bonding interactions, but the MOs with nodes coplanar with the short axis do (i.e., $\pi_{2\text{-}D}^{-}$ and $\pi_{2\text{-}E}^{-}$ in Fig. 34). These limitations in the inter-ring MO overlap lower the SBO relative to 2-PD and can explain the higher energy of the PD_x dimer. Finally, if the increase in size of the monomer π-systems leads to an increase in the number of bonding dimer MOs at the PD structures, there should also be a strong correlation between WBI_{tot}, the ΔE and the size of the π-system. This correlation is shown in Fig. 32b–d and includes Bz_2 calculated at the same level of theory. This result further demonstrates the importance of orbital interactions to π-stacking.

Table 9. DFT(M06-2X)/TZVP interaction energies (ΔE, kcal mol^{-1}) and structural parameters (Å) for the S and PD conformations of the dimers 1, 2 and 3.

	S		PD			
	ΔE	**R_{vert}**	**ΔE**	**R_{vert}**	**$R_{slip\,X}$**	**$R_{slip\,Y}$**
Bz_2	−0.44	3.75	−2.24	3.37	1.73	—
1	−1.70	3.71	−5.51	3.33	1.33	1.09
2	−3.18	3.70	−9.03	3.30	1.26	1.21
			−7.15[a]	3.30	1.37	0.00
3	−4.41	3.68	−12.37	3.30	1.28	1.13

[a] **For 2 slipped along the x axis only (2-PD_x).**

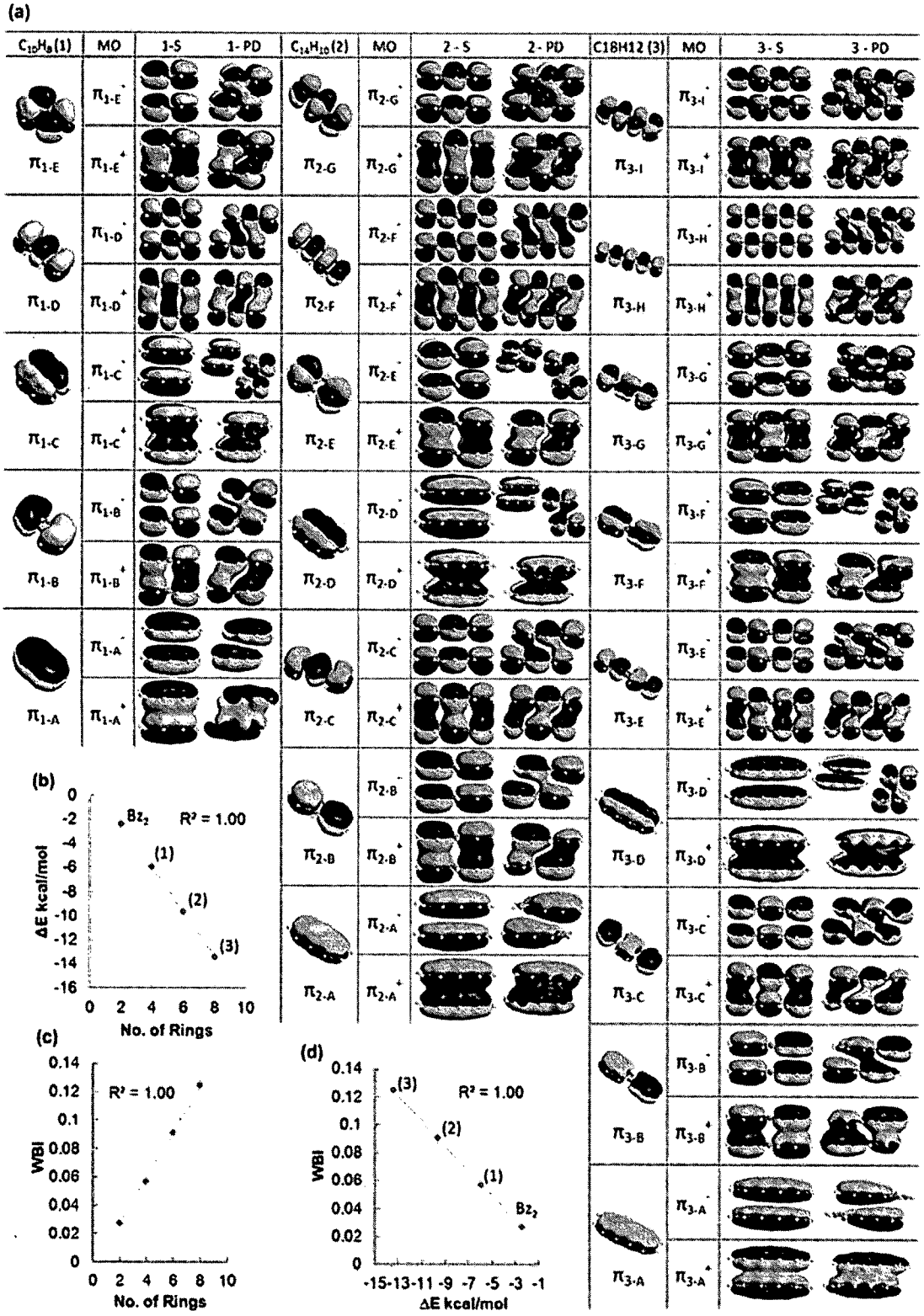

Figure 32. Orbital representations and correlation plots for PAH. (a) MOs for PAH dimers at the S and PD conformations (isosurface = 0.01). The DFT(M06-2X) energies of formation (ΔE) of the PD π-stack correlate well to the number of rings (b). The total inter-ring WBIs also correlate to the number of rings (c) and ΔE (d).

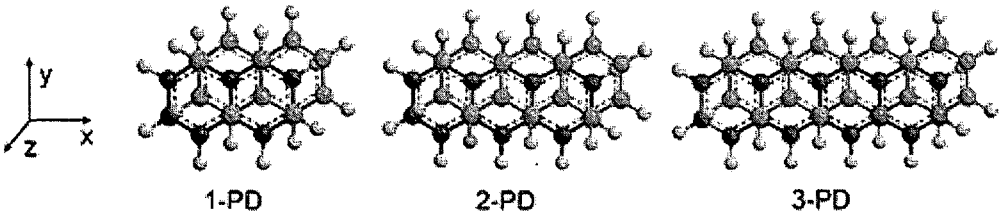

Figure 33. Structures of the PD conformations of the naphthalene (1), anthracene (2) and tetracene (3) dimers.

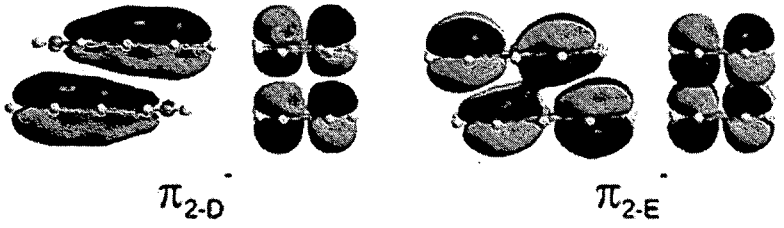

Figure 34. Views of selected MOs for 2-PD_x showing a node in the xz plane. Allowing the rings to rings to slip in the y direction allows greater mixing of the π lobes (compare the analogous 2-PD MOs in Fig. 8).

Conclusions

Although high-level methods such as DF-DFT-SAPT are effective in accurately describing the dispersion and other contributions to the π–π interaction energy, these methods have not yet provided a clear explanation for the geometric distortions from the S structure common to π-stacked systems. The traditional methods of MO analysis employed in this study suggest that PD and TW conformations originate from a shift in the inter-ring bonding character resulting from the parallel-displacement and/or twisting of the rings. In analogy to qualitative MO theory, S conformations have an equal number of bonding and antibonding π-type MOs occupied leading to zero net stack bond order (SBO). Allowing the rings to slip and/or twist can convert one or more of the antibonding MOs to bonding, or possibly nonbonding, resulting in an nonzero SBO for the stack, which maximizes the inter-ring density and allows a closer contact between the rings. The net bonding inter-ring character also leads to increased penetration of the π densities. A zero SBO is predicted generally for all fully S structures of π-stacked homodimers. Therefore, we should never expect to observe a fully S homodimer of an aromatic compound (in analogy to the lack of a bond in He_2), and these π-stacks should always be found in some distortion from the S structure (PD, TW, or a non-stacked conformation) that increases the SBO. Further, our analysis of π–π interactions using orbital-based methods such as the SBO and the Walsh rule represents a change in perspective on these systems. Rather than viewing a π-stacked system as two interacting species, we consider the dimer as a single system for which the preferred geometry can be traced to the manner in which the MOs of the system mix.

Many discussions, including those in textbooks, assume that the inter-ring overlap is greatest at S, but these, often qualitative, discussions do not take into consideration the repulsions between filled antibonding MOs which force the rings apart, necessarily reducing the interaction of the monomer MOs. As a result and contrary to much conventional wisdom, the dispersion and other contributions to the interaction energy are maximized at the PD structure, where the greatest inter-ring density is found. More

importantly, the change in SBO due to parallel displacement and/or twisting is a general phenomenon independent of method, functional or basis set and is observable even using methods that do not adequately reproduce the dispersion component of the energy.

Discussions of π-stacking would benefit from a qualitative analysis of the overlap of the monomer densities, specifically the orbital interactions between individual π systems, in addition to highly accurate quantitative calculations of the interaction energies. Such analysis would provide a more intuitive picture of the interaction as well as how it could be enhanced and how it could compete with other noncovalent interactions. Further, as the trends in SBO, except the WBIs, are observed even with inaccurate functionals and limited basis sets, qualitative orbital analysis is a potential tool to aid intuitive design in crystal engineering, molecular recognition and drug design, molecular wires and other emerging fields where π-stacking interactions are important, but highly accurate methods are cost-prohibitive.

CHAPTER 5

USING STACKED BOND ORDER TO UNDERSTAND π-STACKING PREFERENCES

Introduction

Non-covalent π-π interactions stabilize DNA helices,[233,234] protein tertiary structures,[235] engineered organic crystals,[236] organic electronics,[237] biological recognition motifs,[238] and rational drug design,[185] and is important for researchers in diverse fields. X-ray crystallography shows that many aromatic molecules form a parallel displaced (PD) stacks,[179] with planes separated by distances of 3.3-3.6 Å.[239] Sandwiched (S) structures, where the rings are eclipsed over each other, are rare.[179] The two prominent explanations for the preferential PD geometry of π-stacked dimers are both electronic in nature. In the first explanation, Hunter and Sanders state that the PD geometry reduces π-π repulsion and increases the attraction between the positively charged σ framework and the π-electron cloud.[198] The second explanation is that PD π-stacked benzene dimers are more stable than S because of more favorable quadrupole-quadrupole interactions.[199, 240] The quadrupole-quadrupole explanation has recently been discarded in light of accurate calculations that show that quadrupole-quadrupole interaction in PD benzene to be slightly repulsive.[235, 241] For the benzene-hexafluorobenzene π-stacked dimer, the opposite signs of the quadrupole moments of the monomers are attractive at the S structure but become repulsive in the preferred PD structure.[235] In our previous study of small stacked dimers (Chapter 4), we showed that orbital interactions could explain why PD and twisted geometries (TW) are preferred over the S structure.[242] The stacked bond order (SBO) was introduced, which is the difference between the number of occupied in-phase, or bonding, and the out-of-phase, or antibonding, inter-ring character π-type molecular orbitals (MOs). SBO is analogous to qualitative MO theory that states when two closed shell molecules interact, the bonding and antibonding MOs cancel to give a bond order of zero and a repulsive interaction.[242-243] When identical aromatic rings are in the S conformation they form an equal number of bonding and antibonding π-type MOs, leading to a SBO of zero, which causes the rings to separate and not interact. When the rings are displaced or twisted, one or more of the π-type MOs convert from antibonding

to nonbonding or bonding inter-ring character, leading to a non-zero SBO and a favorable interaction.[242]

Our goal for this Chapter is to explore the use of qualitative SBO to understand the geometrical preference for TW and PD conformations in π-stacked dimers. We will study the following simple systems: dimers of benzene (Bz_2), pyridine (Pyr_2), pyrimidine (PY_2), 1,3,5-trifluorobenzene ($(F_3Bz)_2$), hexafluorobenzene ($(F_6Bz)_2$) and heterodimer benzene-hexafluorobenzene (Bz-F_6Bz), to derive general principles that can be used to rationalize the preferred geometries of a broad range of π-stacking interactions.

Theoretical methods

The inter-monomer distance (R_{vert}) and the PD distance (R_{slip}) were optimized using DFT and the meta-generalized gradient approximation functional M06-2X[209] of Zhao and Truhlar with the aug-cc-pVTZ[68] basis set, or the SVWN[57, 210] functional with Dunning's split-valence triple-ζ basis set augmented with polarization functions (TZVP)[101] using the Gaussian 09 software package.[97] The Gaussian 09 ultrafine grid was used in all calculations. The M06-2X functional with the aug-cc-pVTZ basis set was tested against CCSD(T) benchmarks for noncovalent interactions and was found to provide accurate results for the test cases with differences of a few tenths of a kcal/mol.[244] M06-2X implicitly models the effects of medium range dispersion interactions without the addition of empirical dispersion terms.[244]

Within the dimers, the monomer geometries were fixed at optimized geometries at the same level of theory as the dimers, and were constrained to be planar and parallel to each other. A Walsh diagram was constructed from the DFT(M06-2X)/aug-cc-pVTZ Kohn-Sham orbital energies as a function of R_{slip} for each of the dimers. A Löwdin bond order[245] (LBO) analysis on the SVWN/TZVP structures within the PQS software package[246] was used to quantify the interactions between monomers. The bond order B_{kl} in the Löwdin analysis is given by equation 46, where S, P, k and l are the overlap matrix, density matrix and fragments respectively.[247]

$$B_{kl} = \sum_{rk} \sum_{sl} (S^{1/2} \dot{P} S^{1/2})_{rksl} \qquad (46)$$

$$TLBO = \sum B_{kl} \quad (47)$$

The LBO first transforms the atomic orbital (AO) basis functions into an orthonormal set, then sums all the diagonal terms associated with the atom centered AOs.[46, 248] The total Löwdin bond order (TLBO) is the sum extended over all atom-atom pair wise interactions above the threshold of 0.002 (equation 47). LBOs have been used to quantify the bonding interaction between molecules in covalently bound atoms and weak non-covalent interactions, included π-stacking interactions.[249-251]

Results and Discussion

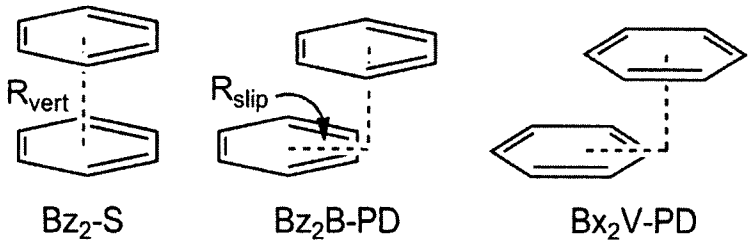

Benzene dimer

The three most studied configurations of the benzene (Bz_2) π-stacked dimer are S (Bz_2-S) and PD across the vertex (Bz_2V-PD) or the bond (Bz_2B-PD). The energy difference between the PD structures is small, and the interconversion between them should be easy. Nevertheless studying these geometries and how the π-π orbital interactions change along the potential energy surfaces is important for understanding π-stacking.[244] Lee finds the Bz_2V-PD conformation to be lower in energy than Bz_2B-PD,[194] but Sherrill finds them to be isoenergetic.[244] We found Bz_2V-PD to be slightly lower in energy than Bz_2B-PD with both the M06-2X and the SVWN DFT functionals consistent with Lee's study[194, 244] (Fig. 35a and Table 10).

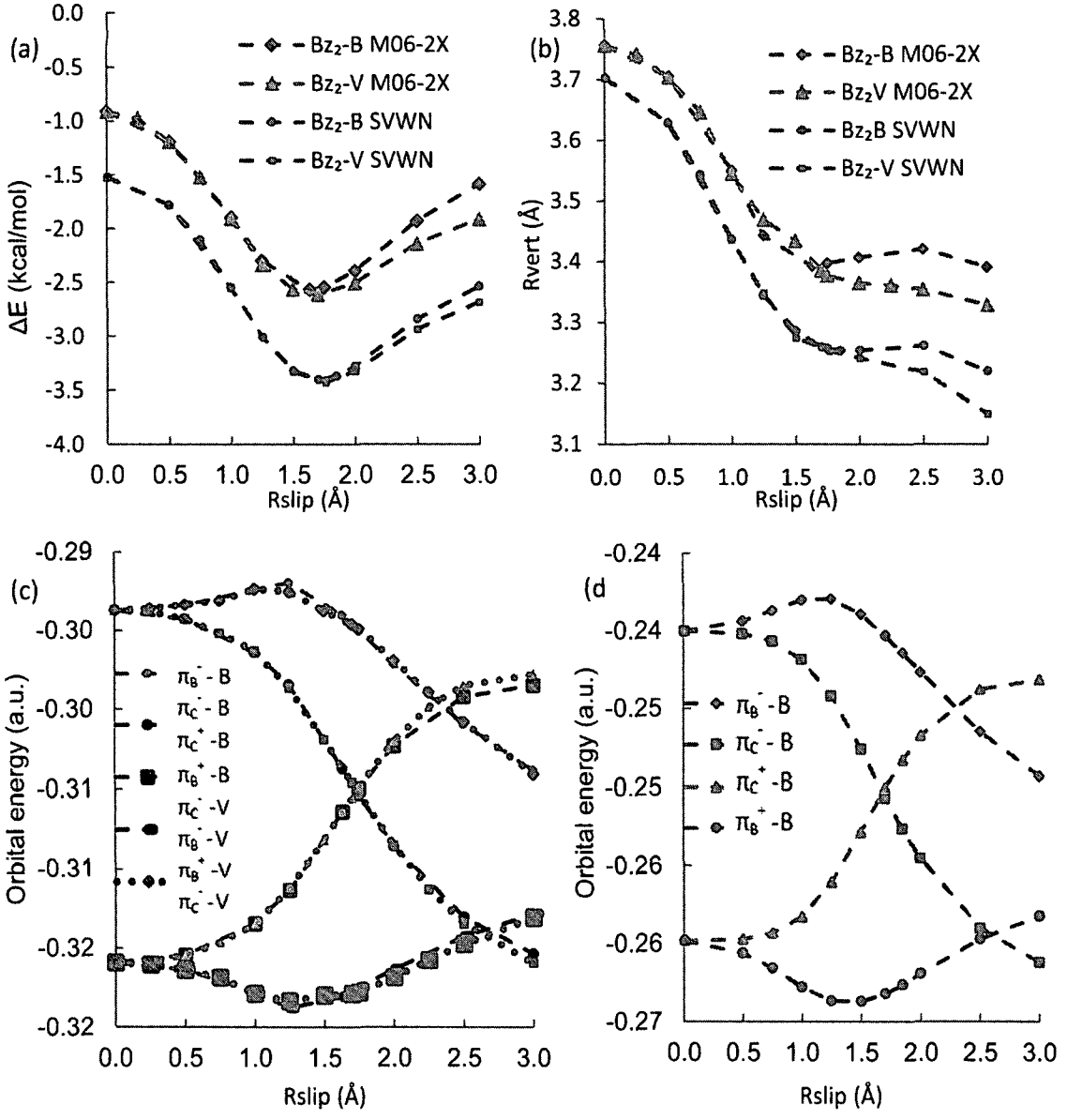

Figure 35. Potential energy curve, plot of inter-ring distance, and Walsh diagrm for Bz_2. (a) Potential energy curve for Bz_2B and Bz_2V calculated with M06-2X/aug-cc-pVTZ and SVWN/TZVP as a function of parallel displacement (R_{slip} in Å). (b) Plot of inter-ring distance R_{vert} as a function of R_{slip} in Å for both Bz_2B and Bz_2V. (c) Walsh diagram of the top four M06-2X/aug-cc-pVTZ molecular orbital energies of Bz_2B and Bz_2V as a function of R_{slip}. (d) The Walsh diagram of the top four SVWN/TZVP molecular orbital energies of Bz_2B as a function of R_{slip}.

Table 10. Interaction energies (kcal/mol) and structural parameters (Å) for Bz_2B and Bz_2V. [a][244] [b][194] [c][242]

Dimer	ΔE(kcal/mol)	Method	Basis set	R_{vert} (Å)	R_{slip} (Å)	SBO	Symmetry
Bz_2B[a]	-2.69	CCSD(T)	CBS(extrapolated)	3.50	1.70		
Bz_2V[a]	-2.69	CCSD(T)	CBS(extrapolated)	3.50	1.70		
Bz_2B[b]	-2.10	CCSD(T)	aug-cc-pVTZ				
Bz_2V[b]	-2.33	CCSD(T)	aug-cc-pVTZ	3.5(fixed)	1.80		
Bz_2-S	-0.91	MO6-2X	aug-cc-pVTZ	3.76	0.00	0	C_{2h}
Bz_2B	-2.57	MO6-2X	aug-cc-pVTZ	3.39	1.63	2	C_{2h}
Bz_2V[c]	-2.61	MO6-2X	aug-cc-pVTZ	3.39	1.70	2	C_{2h}
Bz_2S	-1.53	SVWN	TZVP	3.70	0.00	0	
Bz_2B	-3.40	SVWN	TZVP	3.26	1.70	2	C_{2h}
Bz_2V	-3.43	SVWN	TZVP	3.25	1.76	2	C_{2h}

a. Reference 244, b. reference 194, c. reference 242.

In Chapter 4, we studied the dimer MO interactions in Bz_2V-PD along the R_{slip} potential energy curve.[242] At the Bz_2-S geometry, the π-type Bz MOs (π_A, π_B, π_C) combine to form an equal number of bonding (π_A^+, π_B^+, π_C^+) and antibonding (π_A^-, π_B^-, π_C^-) dimer MOs, giving a SBO of zero, and an unfavorable interaction. We saw that π_B^-, the antibonding combination of π_B from each of the monomers, changed to bonding character at the optimal R_{slip} distance of 1.7 Å, giving an SBO of 2 and an attractive interaction.[242] Bz's MO π_B has a node that is perpendicular to the direction of the slip, and upon sliding, the same sign lobes overlap (Fig. 36). In the Bz_2B-PD structure, it is monomer MO π_C, which has a node perpendicular to the line of slip. Dimer MO π_C^-, the antibonding combination of π_C from each monomer, changes from antibonding to bonding character as it slides from the S to the optimal R_{slip} (1.6 Å), giving a SBO of 2. The bonding dimer MO π_C^+ changes to antibonding at R_{slip} of 3.00 to offset the bonding character of π_C^-, returning the stack to an SBO of zero. Therefore, the optimal R_{slip} distance should have the largest combination of bonding character in the dimer MOs. The other combinations of monomer MO, π_A and π_B, which have a node that is parallel to the line of slip, do not drastically change character from 0.00 to 3.00 Å. R_{vert} decreases as the monomers are slid past one another and the SBO increases (Fig 35b). The Pauli repulsion from the close contact of closed-shell MOs leads to large R_{vert} values for the S structure, but the conversion of π_C^- to bonding lessens the repulsion and allows the monomer MOs to move closer together as they approach the optimal R_{slip} distance. Past the optimal slip distance, R_{vert} continues to decrease, but because the monomers interact with each other less and less.

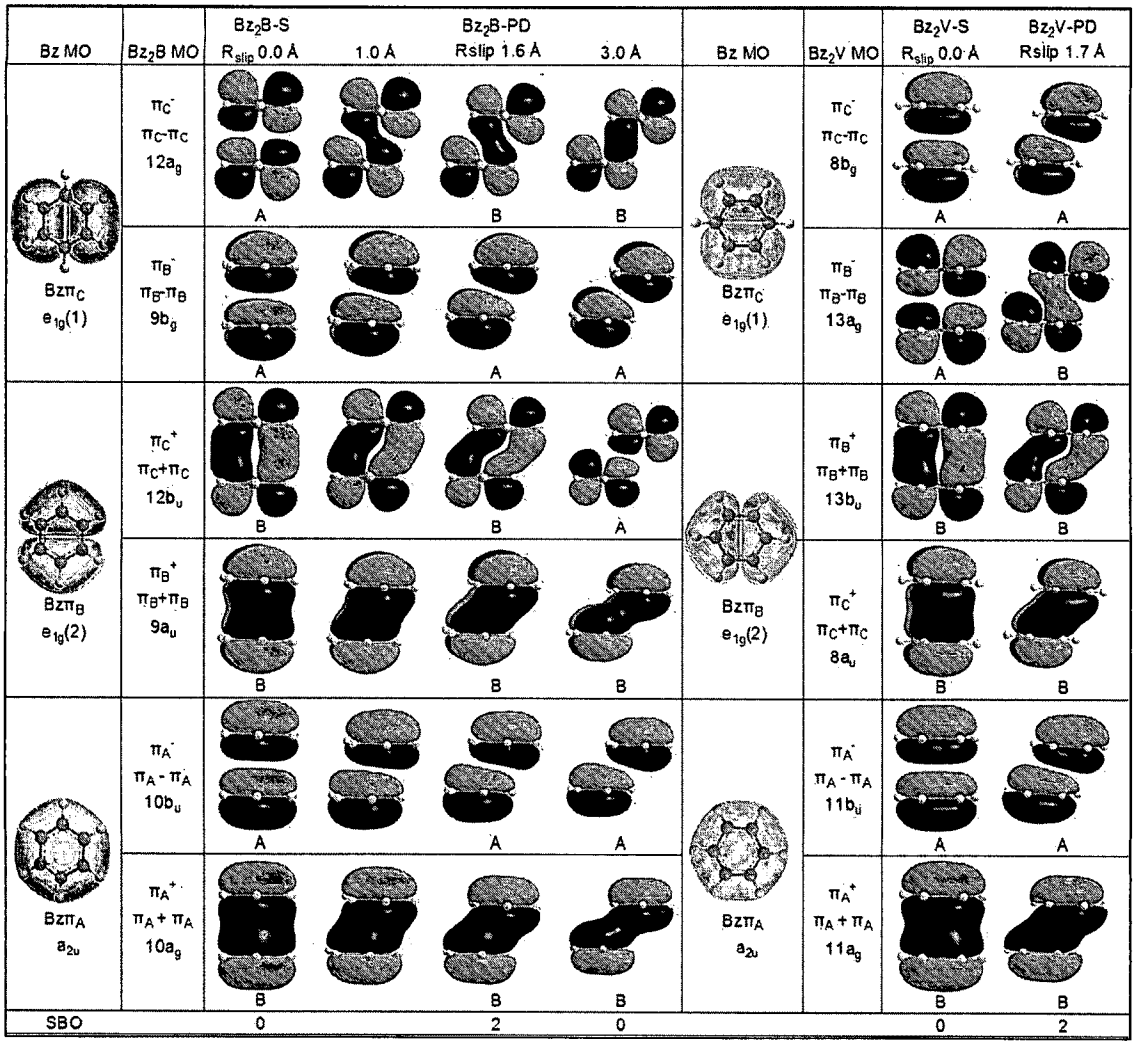

Figure 36. Representation of the six π-type dimer MOs (M06-2X/aug-cc-pVTZ, C_{2h} symmetry) of Bz_2B-PD and Bz_2V-PD as a function of R_{slip}. The isosurface value is 0.010.

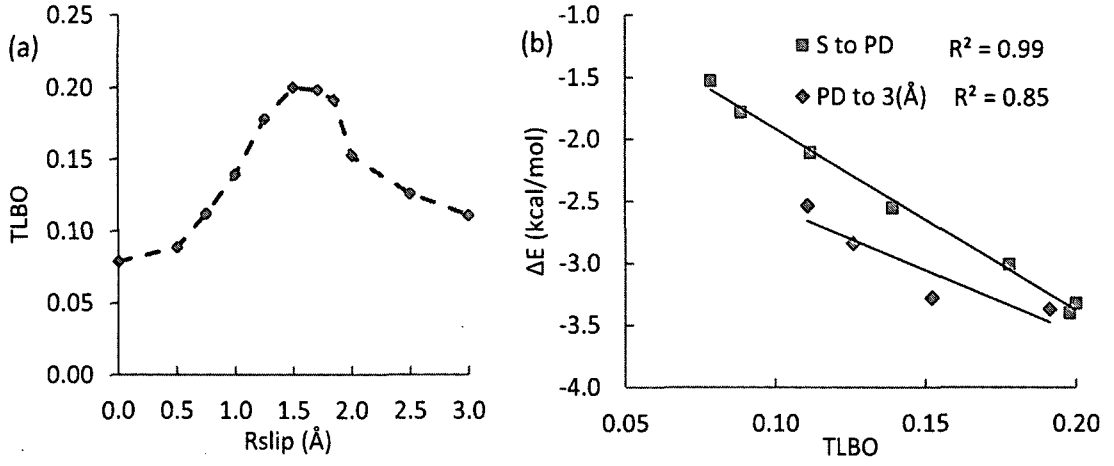

Figure 37. TLBO plots for Bz_2. (a) SVWN/TZVP Total Löwdin bond order for Bz_2B-PD as a function of R_{slip}. (b) SVWN/TZVP interaction energy for Bz_2B-PD as a function of the total Löwdin bond order.

The M06-2X/aug-cc-pVTZ Walsh diagrams for Bz_2B-PD and Bz_2V-PD show strong similarities (Fig. 35c). The dimer MOs, π_C^- and π_C^+ (Bz_2B-PD) and π_B^- and π_B^+ (Bz_2V-PD), are the MOs that change the most in energy as the monomers slip apart. Both π_C^- (Bz_2B-PD) and π_B^- (Bz_2V-PD) decrease in energy as the same sign nodes start to line up with each other, π_C^+ (Bz_2B-PD) and π_B^+ (Bz_2V-PD), increase in energy as the opposite sign nodes start to line up with each other. The energies of π_C^- and π_C^+ cross near the optimal slip distance (Bz_2B-PD), as do π_B^- and π_B^+ (Bz_2V-PD). Dimer MOs, π_B^- and π_B^+ (Bz_2B-PD) and π_C^- and π_C^+ (Bz_2V-PD), do not change significantly in energy from S to the optimized R_{slip}. Past the optimized slip they move towards each other in energy, as they will become degenerate when the monomers are no longer interacting. The SVWN/TZVP Walsh diagram (Fig. 35d) shows the same general trends as M06-2X. The Bz_2B-PD SVWN TLBOs for each geometry optimization along the slip from 0.0 to 3.0 Å is maximized near the optimal slip distance, suggesting that the optimal PD geometry is determined by the increase in inter-ring density (P_{KL} equation 46) (Fig. 37a). These results are consistent with the total Wiberg indices that were found to be maximized at the optimal Bz_2V-PD geometry in Chapter 4.[242] The high correlation between the TLBO and ΔE for Bz_2B-PD provide evidence that orbital interactions are responsible for the preference for the PD geometry. The difference in

slope before and after the optimal slip distance results from the differences in how the monomer MOs interact before and after the optimal R_{slip} distance. From the S structure to the optimal R_{slip}, the monomers have an increasing interaction, whereas past the optimal slip distance, the monomers are moving away from each other and interacting with each other less and less (Fig. 37b).

Pyridine dimer

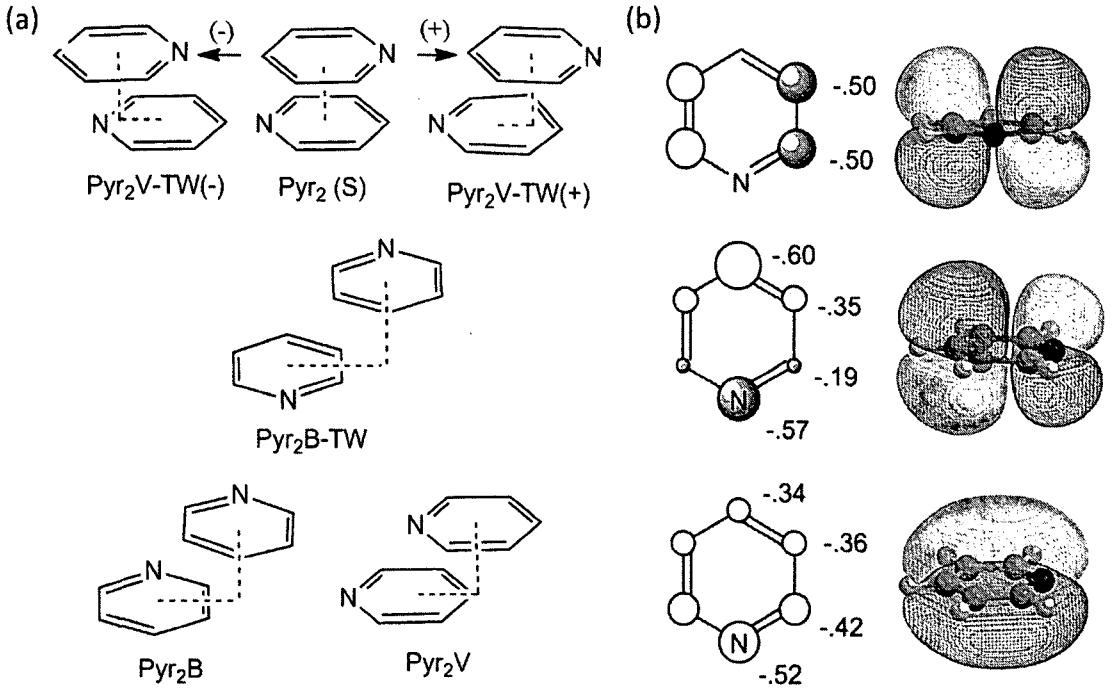

Figure 38. Pyr_2 geometries and orbital representation of Pyr. (a) Geometries for the pyridine dimer. (b) Schematic drawing of the molecular-orbital coefficients of pyridine including representation of the three π-type orbitals of pyridine (C_{2v} symmetry). In the ball-and-stick representation of the framework. The isosurface value is 0.01.

A similar analysis to Bz_2 was made for seven different geometries of Pyr_2 (Fig 38), to determine if the concepts of the SBO can be used to understand the energy and

preferred geometry of the Pyr_2 structures. Pyr_2 was examined because it and related systems are important compounds in biological systems,[252] and its binding energy is higher than that of benzene.[216, 253] The interaction energies for various orientations of the dimer are in agreement with previous results reported by Sherrill et al.[195] (Table 11, Fig. 39a and 39b) in which Pyr_2B-TW-PD was the most stable, followed by Pyr_2V-TW-PD(+), Pyr_2V-TW-PD(-), and Pyr_2V-TW-S. The non-twisted Pyr_2-S had the least favorable geometry.[195] A crystal structure analysis of pyridine stacking interactions in the Cambridge Structural Database (CSD) found 66 instances of parallel packing of pyridine dimers, with the most prevalent geometry (56 out of 66) of Pyr_2-TW-PD with r_{vert} values from 3.1 to 4.0 Å.[254]

In Chapter 4, the orbital interactions in Pyr_2B-TW-PD geometry were examined as the monomers, with opposing dipoles, were displaced across the bond. The dimer MO π_F^- of Pyr_2B-TW, composed of two monomer π_F MOs with a node perpendicular to the line of the displacement changed from antibonding to bonding character as it moved from the S conformation to the optimal R_{slip} geometry. The SBO of Pyr_2B-TW changed from 0 at the S geometry to 2 at PD, analogous to the MOs in Bz_2.[242] MO π_F has a node centered on N, with symmetrical lobes on either side.

Table 11. Interaction energies (kcal/mol) and structural parameters (Å) for Pyr_2. a[195]

Dimer	ΔE	Method	Basis set	Rvert	Rslip	SBO
Pyr_2TW-S	-2.1	M06-2X	aug-cc-pVTZ	3.66	0.00	0
Pry_2B-TW	-3.86	M06-2X	aug-cc-pVTZ	3.30	1.50	2
Pry_2V-TW(+)	-3.42	M06-2X	aug-cc-pVTZ	3.27	1.54	2
Pry_2V-TW(-)	-2.51	M06-2X	aug-cc-pVTZ	3.42	-1.69	2
Pyr_2 S	-0.67	M06-2X	aug-cc-pVTZ	3.73	0.00	0
Pyr_2V	-2.05	M06-2X	aug-cc-pVTZ	3.34	1.70	0
Pry_2B	-1.79	M06-2X	aug-cc-pVTZ	3.34	1.57	2
Pyr_2TW-S	-2.96	SVWN	TZVP	3.54	0.00	0
Pry_2B-TW	-4.74	SVWN	TZVP	3.17	1.51	2
Pry_2V-TW(+)	-4.57	SVWN	TZVP	3.25	1.37	2
Pry_2V-TW(-)	-3.60	SVWN	TZVP	3.17	-1.65	2
Pyr_2 S	-1.27	SVWN	TZVP	3.65	0.00	0
Pyr_2V	-3.04	SVWN	TZVP	3.20	1.70	0
Pry_2B	-3.10	SVWN	TZVP	3.22	1.64	2
Pyr_2TW-S[a]	-2.88	SCS-MP1	aug-cc-pVTZ	3.70	0.00	
Pyr_2B-TW[a]	-3.84	SCS-MP2	aug-cc-pVTZ	3.4(fixed)	1.60	
Pry_2V-TW(+)[a]	-3.23	SCS-MP2	aug-cc-pVTZ	3.5(fixed)	1.60	
Pry_2V-TW(-)[a]	-2.36	SCS-MP2	aug-cc-pVTZ	3.5(fixed)	-1.40	
Pyr_2 S[a]	-1.56	SCS-MP3	aug-cc-pVTZ	3.8	0.00	
Pyr_2V[a]	-2.24	SCS-MP2	aug-cc-pVTZ	3.5(fixed)	1.60	
Pyr_2B[a]	-2.54	SCS-MP2	aug-cc-pVTZ	3.5(fixed)	1.60	

a. Reference 195.

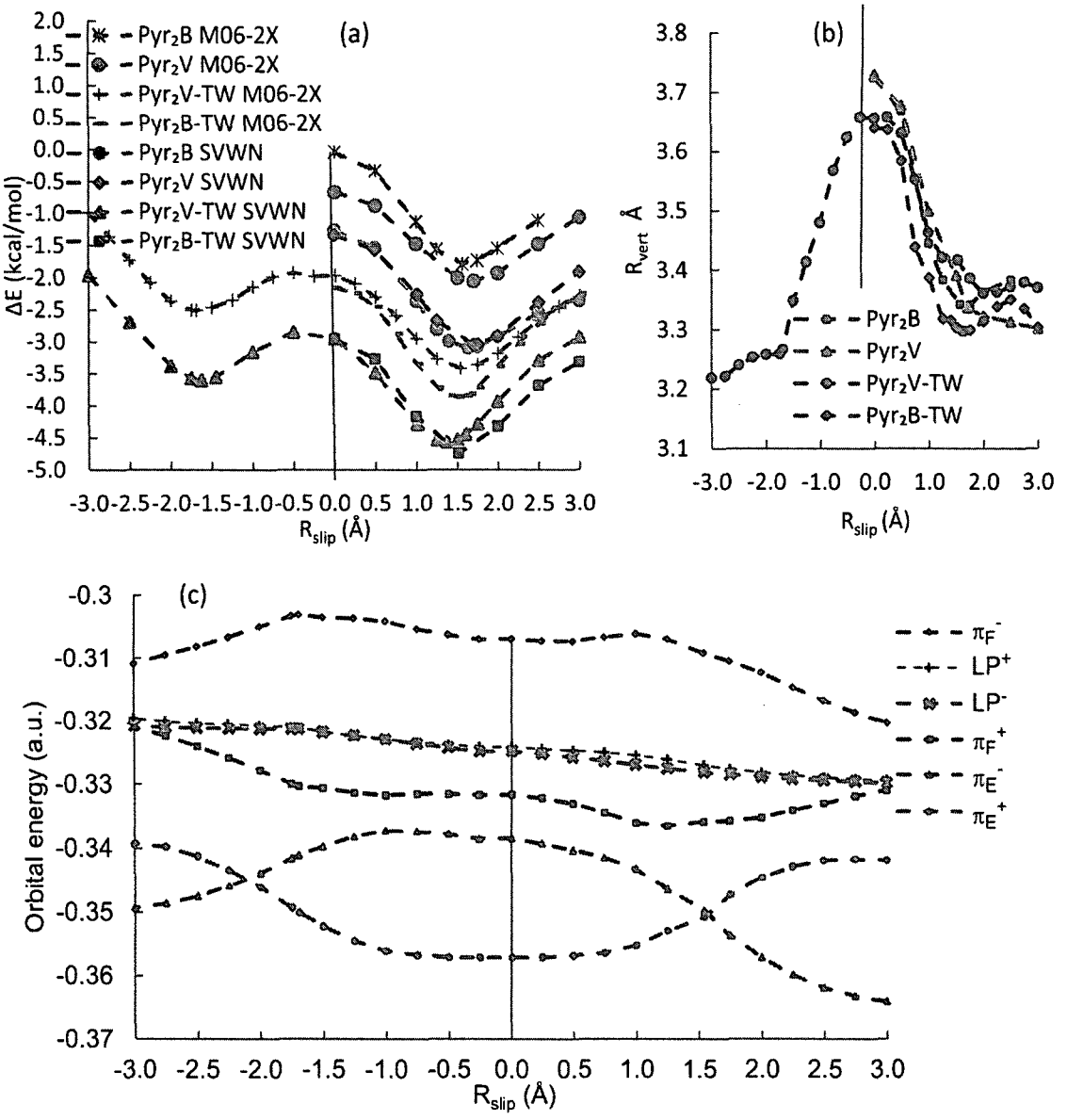

Figure 39. Potential energy curve and Walsh diagram for Pyr_2. (a) Potential energy curve for Pyr_2 calculated with DFT functional M06-2X and SVWN as a function of parallel displacement (R_{slip} in Å). (b) Plot of the M06-2X inter-ring distance (R_{vert}) as a function of R_{slip} in A for Pyr_2. (c) Walsh diagram of the four M06-2X π-type orbitals and two Pyr_2 lone pairs for PyrV-TW(+) and (-) as a function of R_{slip}.

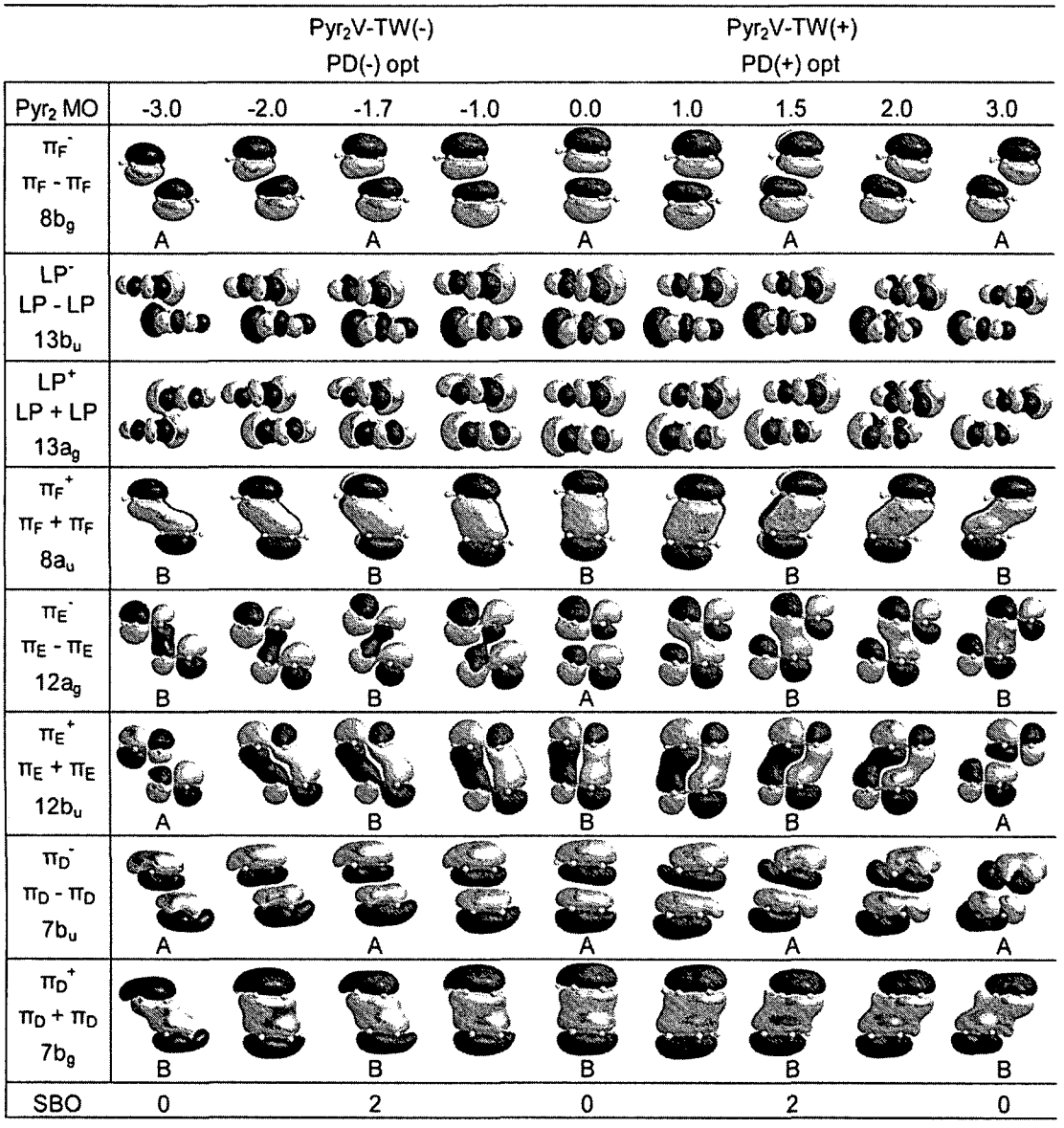

Figure 40. Representations of the four π-type orbitals and two Pyr_2 lone pairs. (C_{2h} symmetry) of Pyr_2V-TW as a function of R_{slip}. The isosurface value is 0.010.

The Pyr_2V-TW geometry, where the monomers with opposing dipoles, are slid across the vertices, was examined in both the (+) and (-) direction (Fig. 38a), since these are not symmetric with respect to horizontal displacement. The monomer MO π_E has a node perpendicular to the direction of the slip that will combine to make π_E^- and π_E^+. Note the asymmetry of the orbital distribution towards the all carbon lobe in the molecular orbital representation of π_E (Fig. 38b). When Pyr_2V-TW is slid in a direction that has the

larger carbon only nodes of π_E aligned, Pyr_2V-TW-PD(+), should be more stable than Pyr_2V-TW-PD(-) that has the smaller same sign nitrogen containing lobes overlapping. The orbital representations of Pyr_2V-TW-PD along R_{slip} (Fig. 40) show that the Pyr_2V-TW-S structure has equal numbers of bonding and antibonding dimer MO and has a SBO of zero. As the top monomer is slid in the positive direction, π_E^- changes from antibonding to bonding character, as the two carbon only, more electron rich, nodes of the same sign slide over each other. When the top monomer is slid in the negative direction, Pyr_2V-TW-PD(-), it is the electron poor nitrogen containing nodes that slide over each other. In the negative direction, the top node slides further to reach the optimal PD geometry. We suggest that the larger slip distance is required for the smaller lobes of the same sign to slide over each other and stabilize the dimer. Pyr_2V-TW-PD(+) is more stable (0.91 kcal/mol) than Pyr_2V-TW-PD(-) due to the better overlap of the larger carbon-only nodes in π_E^-. In the Walsh diagram for Pyr_2V-TW (Fig 39c), π_E^- and π_E^+, widely separated in S, decrease and increase in energy respectively and cross near the optimal R_{slip} for the (+) and past the optimal slip distance for the (-) slip direction. Dimer MOs π_E^- and π_E^+ cross at a lower orbital energy for the Pyr_2V-TW-PD(+), demonstrating that the MOs are more stable and are perhaps responsible for the increased stability of Pyr_2V-TW-PD(+).

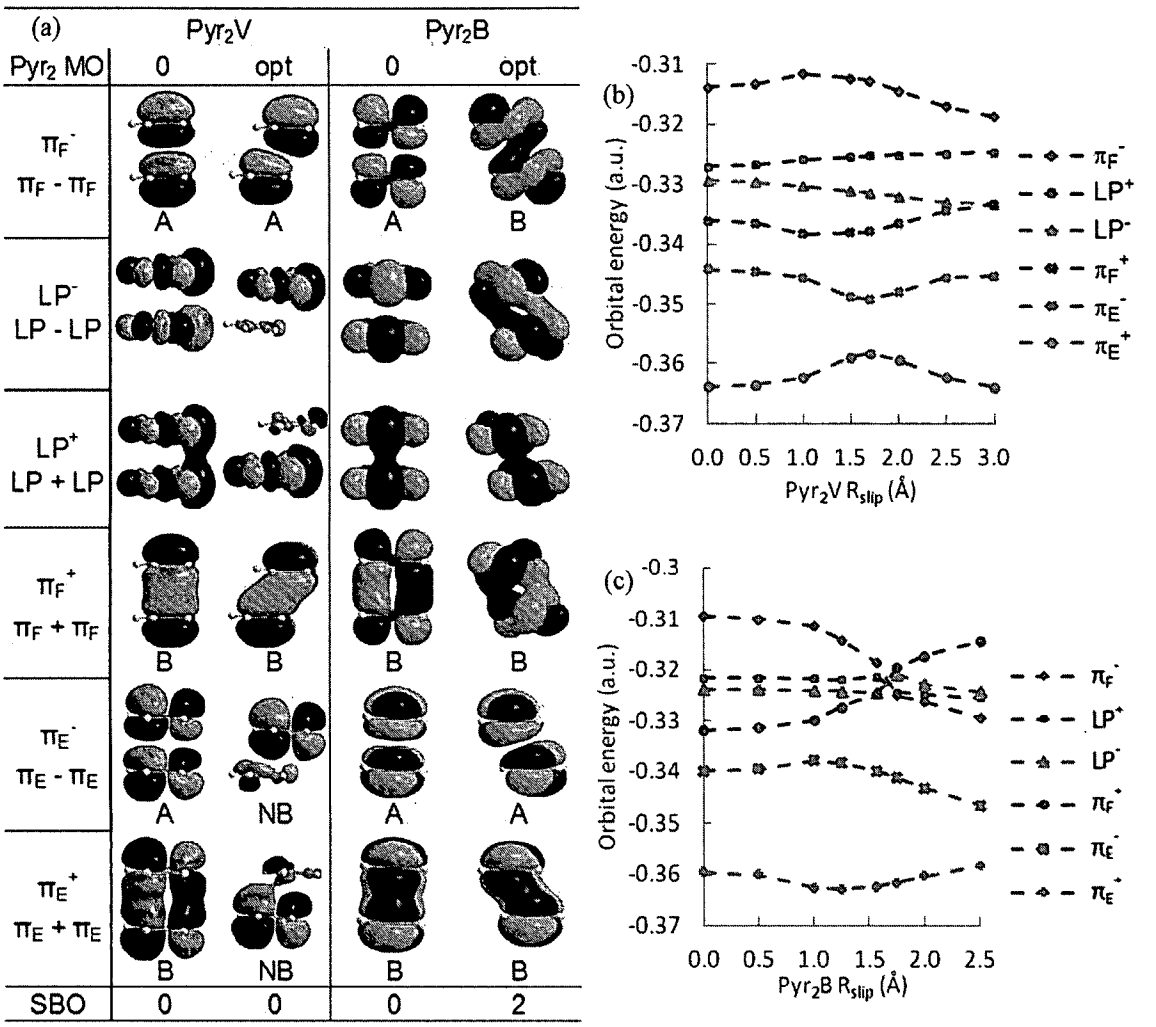

Figure 41. Orbital representations and Walsh diagrams for Pyr_2V and Pry_2B. (a) Representations of the top six dimer MOs of Pyr_2V and Pyr_2B at the sandwich and optimized parallel displaced geometry. The isosurface value is 0.010. (b) Walsh diagram for the top six dimer MO energies of Pyr_2V as a function of R_{slip}. (c) Walsh diagram for the top six dimer MO energies of Pyr_2B as a function of R_{slip}.

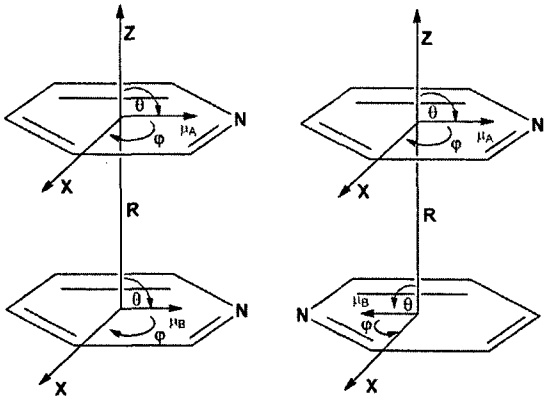

Figure 42. Diagram of Pyr_2-S and Pyr_2-TW-S showing the polar angles, θ, between the dipole vectors μ_A, μ_B, and the azimuthal angle ϕ of μ_A and μ_B with respect to the x axis.[255]

Pyr_2-S has an equal number of occupied bonding and antibonding π-type MO and an SBO of zero (Fig. 41a and 42b). The Walsh diagram for Pyr_2V-PD, with C_s symmetry, has an avoided crossing of π_E^- and π_E^+ at 1.7 Å, because they are of the same irreducible representation A'. As π_E^- and π_E^+ approach each other in energy, they mix producing two new orbitals that have non-bonding character and lead to an overall SBO of zero for Pyr_2V-PD.[218] Because this is not a favorable geometry and is not observed in crystal structures, we assume this geometry is not a valid π-stacking interaction. The trends in MO character for Pyr_2B-PD produce a similar pattern to Pyr_2B-TW, with MO π_F^-, containing a node perpendicular to the line of slip, changing from antibonding to bonding character at the optimal R_{slip} producing a SBO of 2. Dimer MOs π_F^- and π_F^+ decrease and increase in energy and cross near the optimal R_{slip} (Fig. 41a and 42c). The SBO of two for Pyr_2B-TW which is bound weaker than the optimal PD TW geometries of Pyr_2, which also had a SBO of two, indicates that the SBO is qualitative, and can only predict favorable geometries, but cannot conclude which of many geometries will be the lowest in energy.

Unlike Bz, Pyr has a permanent dipole toward the nitrogen atom of Pyr that will influence the π-stacking interaction. The dipole moment from our DFT/M06-2X calculations (2.25 D) is in agreement with the experimental value (2.22 D).[256] The dipole-dipole interaction can be calculated with equation 48, where θ_A *and* θ_B are the polar

angles between the dipole vectors μ_A, μ_B and the z-axis through the line connecting molecules A and B centers of mass

$$\Delta E = -\mu_A\mu_B(2cos\theta_A cos\theta_B - sin\theta_A sin\theta_B cos\varphi)/4\pi\epsilon_0 R^3 \quad (48)^{255}$$

The azimuthal angle ϕ is the difference between the azimuthal angle of μ_A and μ_B with respect to the x axis. For Pyr_2TW-S, θ_A *and* θ_B are both 90.0°, ϕ is equal to 180.0° and ΔE=-1.4 kcal/mol (Fig. 42). When the monomers are parallel displaced over the vertex, Pyr_2V-TW-PD, the stabilization from the dipole-dipole interaction decrease to -0.71 kcal/mol, demonstrating that although the dipole-dipole interaction contributes to the overall stacked energy, it is not the dominate driving force for the preferred PD structure. The over the bond structure loses less dipole-dipole stabilization upon displacement since θ_A *and* θ_B are still both 90.0° and ΔE=-1.4 kcal/mol, which may explain why the stacking energy for Pyr_2B-TW-PD is greater than for Pyr_2V-TW-PD. The S structure that has the dipoles aligned, Pyr2-S, θ_A *and* θ_B are both 90.0° and ϕ is equal to 0.0° and ΔE=1.4 kcal/mol. Sliding the aligned dipoles over the vertex Pyr_2V-PD will increase the dipole-dipole interaction to -0.52 kcal/mole whereas sliding it over the bond Pyr_2B-PD will not change the repulsive contribution from the dipole-dipole interaction. This result can explain why Pyr_2V-PD and Pyr_2B-PD both have low binding energies, while Pyr_2V-PD is less stable. The inter-ring TLBO is maximized for each of the Pyr_2 geometries (Fig. 43) at the optimal R_{slip}, implying that the change in character of the π-MO interactions to a SBO greater than zero is essential for π-stacking interactions.

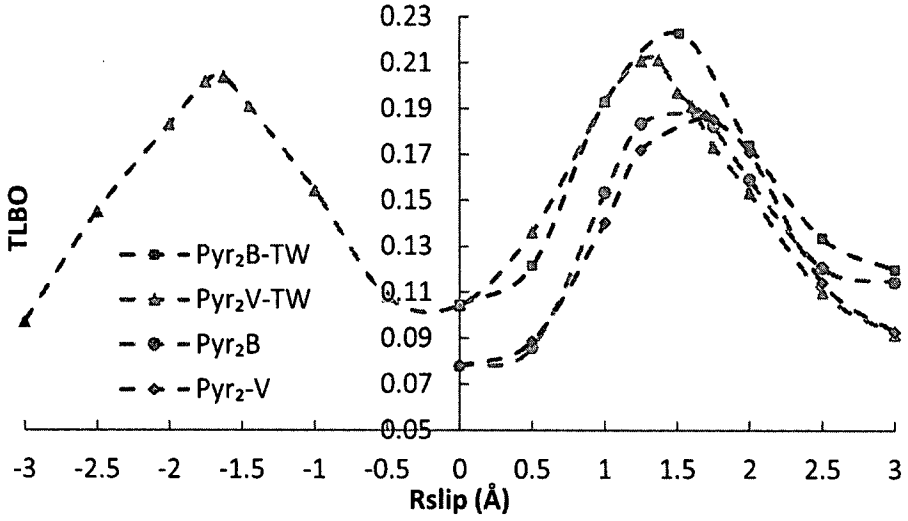

Figure 43. The total inter-ring SVWN/TZVP Löwdin bond orders as a function of R_{slip} for Pyr_2.

Pyrimidine dimer

An analysis similar to that of Pyr_2 was performed on the pyrimidine dimer (PY_2-TW) slid across the vertex. The binding energy was consistent with previous theoretical studies[197, 257] (Table 12, Fig. 43a and 43c). PY_2 is related to the smallest nucleic acid base pairs uracil and cytosine, and an investigation of PY_2 orbital interactions should help to explain π-stacking interaction in DNA bases. The PY monomer, unlike Pyr and Bz, does not have a node that is perpendicular to the slip direction. The two highest PY MOs π_I and π_H, have nodes that are approximately 45° below and above the line of displacement respectively (Fig. 45). Dimer MOs π_I^- and π_H^-, the antibonding combinations of π_I and π_H from each monomer, change character to nonbonding (π_I^-) and bonding (π_H^-) at the optimal R_{slip}, resulting in a SBO of three. Both π_I^- and π_H^-, as seen in the Walsh diagram, decrease in energy along the slip, while π_I^+ and π_H^+, increase in energy. MOs, π_H^- and π_H^+, cross closer to the optimal R_{slip} than, π_I^- and π_I^+, suggesting that the change of π_H^- to bonding character contributes more to the overall bonding energy than the change of π_I^- to nonbonding character. The SBO of three for PY_2V-TW-PD could partially explain why it is more stable than the lowest energy Pyr_2 dimer (Fig. 44b). The inter-ring TLBO is maximized at the optimal R_{slip} distance, giving further evidence that orbital interactions are responsible for the preferred PD geometry (Fig. 44d).

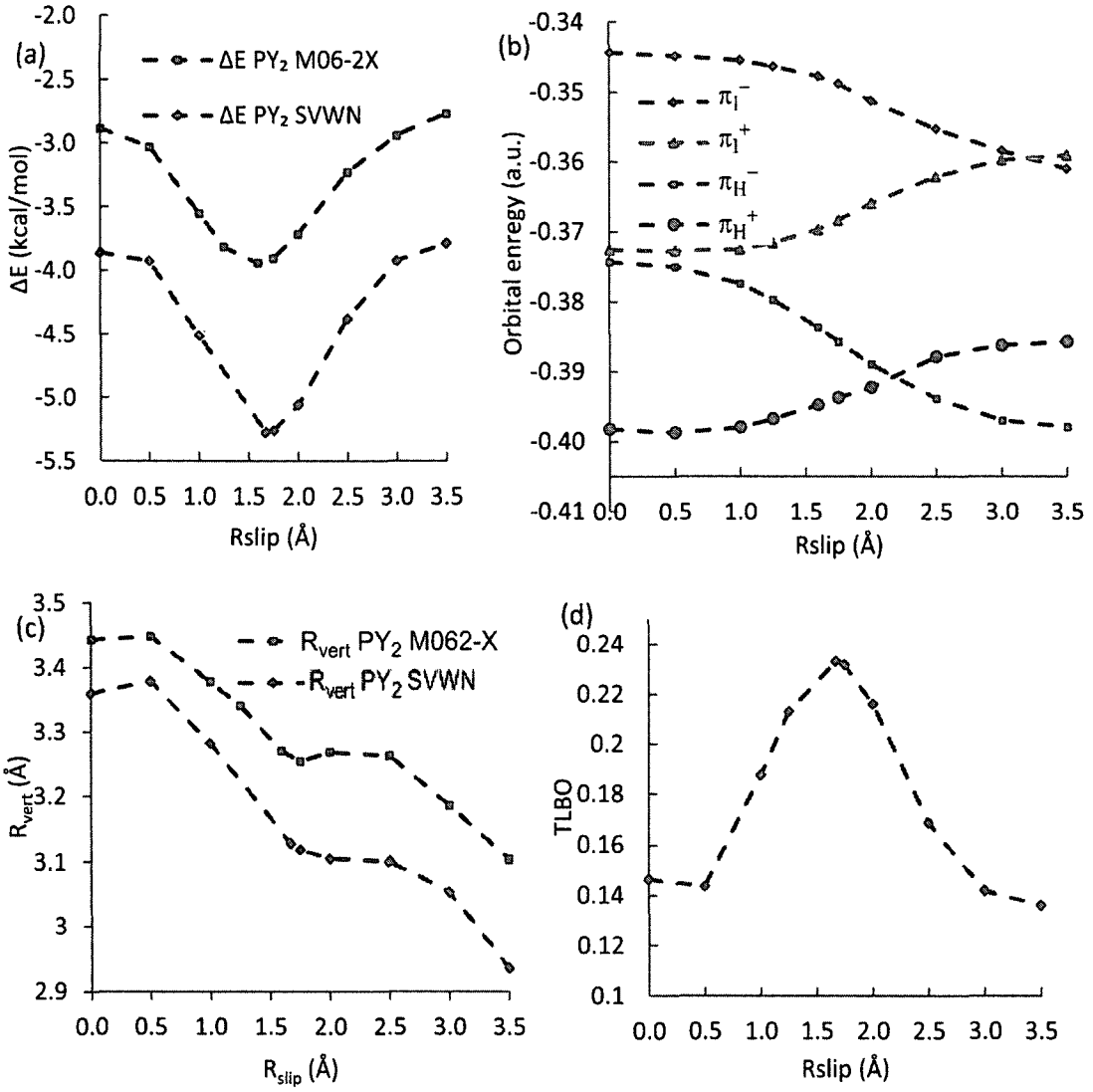

Figure 44. Potential energy curve, Walsh diagram and TLBO for PY_2. (a) Potential energy curve for PY_2 calculated with DFT functional M06-2X and SVWN as a function of parallel displacement (R_{slip} in Å). (b) Plot of the M06-2X and SVWN inter-ring distance (R_{vert}) as a function of R_{slip} in A for PY_2. (c) Walsh diagram of the six M06-2X π-type orbitals for PY_2V-TW as a function of R_{slip}. (d) The total inter-ring SVWN/TZVP Löwdin bond orders as a function of R_{slip} for PY_2.

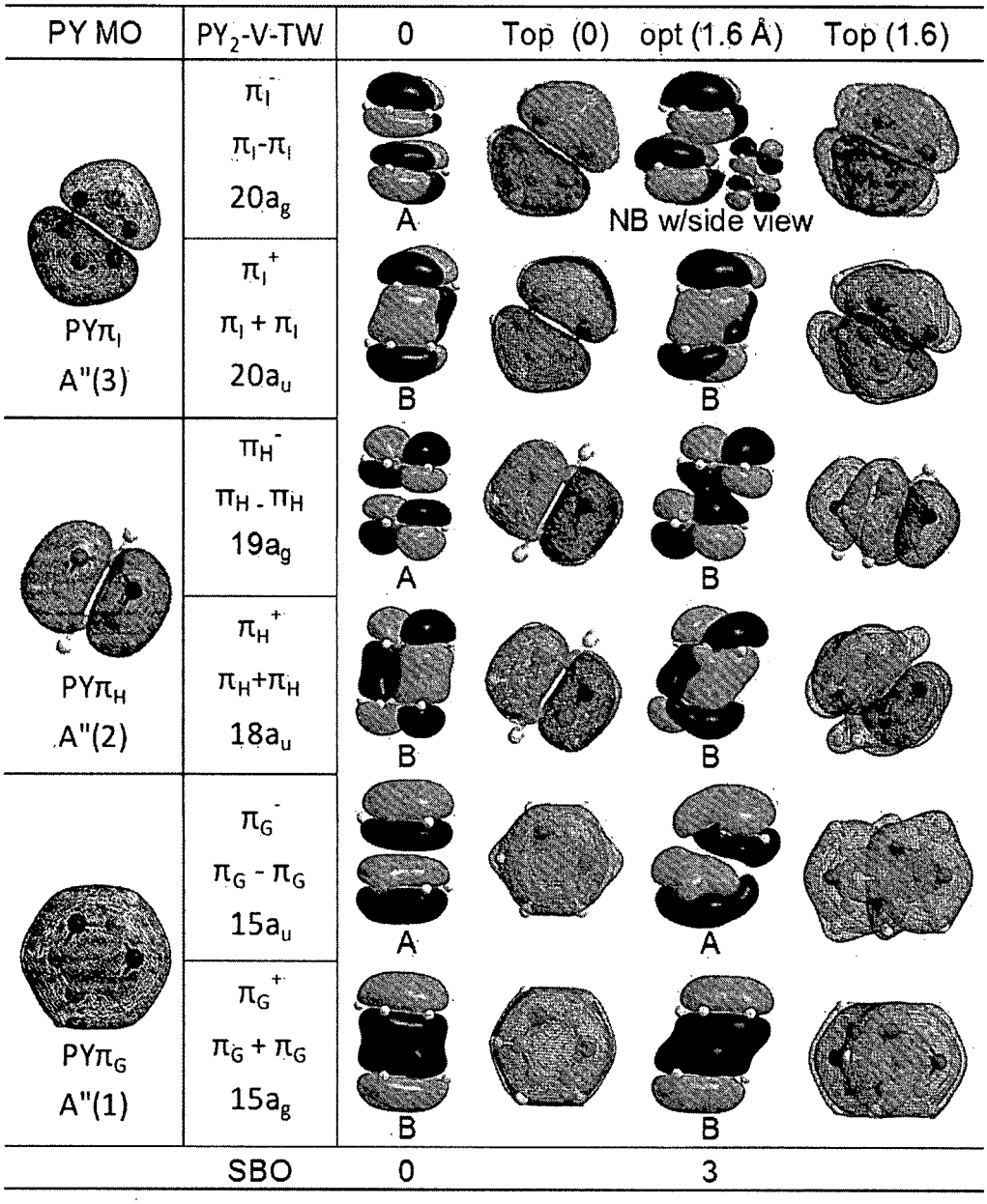

Figure 45. Representations of the top six dimer MOs of PY_2V at the sandwich and optimized R_{slip}. (Isosurface = 0.010)

Table 12. Interaction energies (kcal/mol) and structural parameters (Å) for PY_2V-TW. (a)[197] (b)[257]

Dimer	ΔE	Method	Basis set	r_{vert} (Å)	r_{slip} (Å)	SBO
PY_2-S	-2.89	M06-2X	aug-cc-pVTZ	3.44	0.00	0
PY_2V-TW	-3.94	M06-2X	aug-cc-pVTZ	3.27	1.60	3
PY_2-S	-3.86	SVWN	TZVP	3.36	0.00	0
PY_2V-TW	-5.28	SVWN	TZVP	3.13	1.67	3
PY_2V-TW[a]	-3.40	MP2	CBS(extrapolated)	3.3 (fixed)	0.00	
PY_2V-TW[b]	-3.90	LMP2	CC-pVTZ(f)	3.40	PD	

a. Reference 197, b. Reference 257.

1,3,5-trifluorobenzene dimer

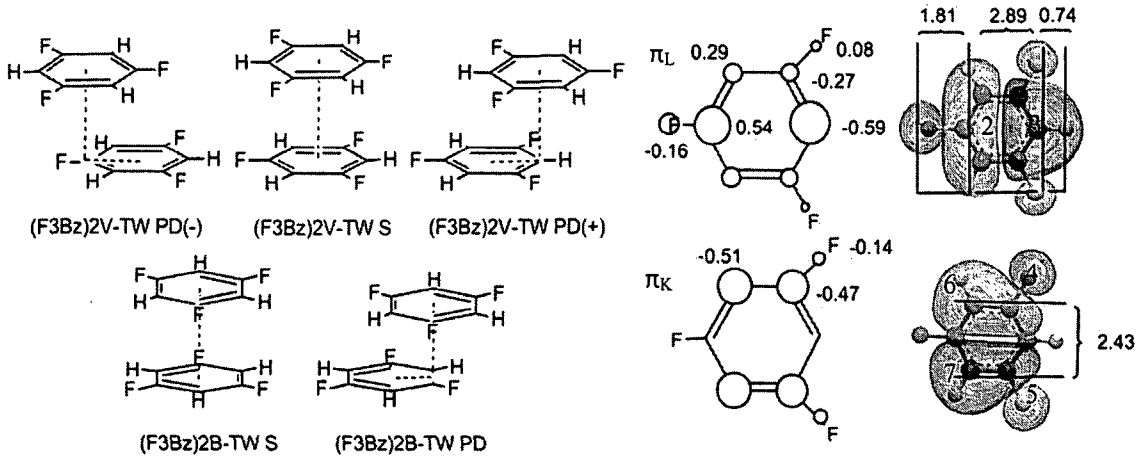

Figure 46. 1,3,5-trifluorobenzene dimer geometries and orbitals. Schematic drawing of the molecular orbital coefficients of trifluorobenzene including representation of the top two π-type orbitals of trifluorobenzene.

In light of our previous results from Bz_2, Pyr_2 and PY_2, we were interested in examining the orbital interactions in the 1,3,5 trifluorobenzene dimer ($(F_3Bz)_2$) since quadrupole-quadrupole interactions have been used to explain the parallel displaced structures of benzene, hexafluorobenzene, and benzene-hexafluorobenzene dimers,[258]

whose monomers have large quadrupole moments.[200] $(F_3Bz)_2$, with a very weak quadrupole moment, also has stable dimers with a TW-PD stacked orientation from melting point, 267 K, to boiling point 349 K.[200, 259] $(F_3Bz)_2$ also exists in the gas phase with a parallel arrangement.[260 259] We investigate $(F_3Bz)_2$-TW both over the bond and over the vertex (Fig. 46). We found $(F_3Bz)_2$V-TW(+) to have the strongest π-stacking energy followed by $(F_3Bz)_2$B-TW, and $(F_3Bz)_2$V-TW(-) with the S structure having the lowest (Table 13, Fig. 46 and 47a). Our π-stacking energy results are in reasonable agreement with previous theoretical studies.[200] The F_3Bz MO π_L has five sets of lobes, the lobe sets along the line of slip are numbered 1-3, with lobe (1), the fluorine centered lobe, having a coefficient that is only 14% as large as carbon centered lobe sets 2 and 3. We will call node set 1 from the top monomer, 1a, and the bottom monomer lobe set 1b (Fig. 46). If our hypothesis is correct π_L^- which has two nodes perpendicular to the line of slip will change from antibonding to bonding character in both the positive and negative slip direction. $(F_3Bz)_2$V-TW-S has an even number of bonding and antibonding MOs and has a SBO of zero, even thought the tri-substituted benzene monomers are not symmetrical with respect to the twist. At the optimal R_{slip}(+), π_L^- has lobe 3a line up with same-sign lobe 3b, increasing the SBO to 2 (Fig. 48). The Walsh diagram for $(F_3Bz)_2$V-TW(+) shows that both π_L^- and π_K^- decrease in energy along r_{slip} while only π_L^- and π_L^+ cross near the optimal R_{slip} (Fig. 47c). MO π_K^- is somewhat stabilized by the overlap of node sets, 4a and 5a, with same sign, 6b and 7b. The extra stabilization from π_K^- may explain the higher π-stacking energy for $(F_3Bz)_2$V-TW(+). When π_L^- is slid in the negative direction, lobe 3a need only slide 0.74Å for the center of node 3a to be over the center of node 1b (SBO = 2). We propose that the short slip distance required for π_L^- to change from antibonding to bonding character is responsible for the unusually short optimal R_{slip} (-0.88 Å) for $(F_3Bz)_2$V-TW(-). The Walsh diagram for the negative slip shows that π_L^- and π_L^+ cross near the optimal Rslip. After π_L^- and π_L^+ cross they again go up and down in energy and are well separated at -2.0 Å (SBO=0), past -2.0 Å they go up and down in energy to cross the second time near -3.5Å. The M06-2X potential energy curve for $(F_3Bz)_2$V-TW(-) reveals a local minimum around -3.0 Å (Fig. 47a). The local minimum may be accounted for by the overlap of lobe set (1a

and 2a) with (2b and 1b) at -3.0 Å, where π_L^+ which has antibonding character at -2.0 Å, changes to nonbonding at -3.0 Å, resulting in a SBO of 1. The $(F_3Bz)_2B$-TW Walsh diagram shows both π_L^- and π_K^- decreasing in energy with π_L^- decreasing faster than π_K^-. (Fig. 47b). This was surprising as we expected only π_K^- which should have had a node perpendicular to the line of slip to decrease in energy as it changed from antibonding to bonding at the optimal R_{slip}. When the MO of $(F_3Bz)_2B$-TW were examined we found that π_L^- and π_K^- had nodes that are approximately 45° above and below the line of displacement similar to what we saw in PY_2V-TW (Fig. 48). Since $(F_3Bz)_2B$-TW has several identical bonds to cross over, sliding over a different bond was tested to see if it would change the MO picture. Regardless of the bond or the DFT method the MO picture was the same. It is MO π_L^- that changes from antibonding to bonding character at optimal R_{slip}, whereas π_K^- decreases in energy but stays antibonding in character, to give a SBO of 2. The plot of the TLBO versus R_{slip} (Fig. 49a) parallels the potential energy curve with the optimal R_{slip} distances having the largest TLBO. The high correlation of TLBO to interaction energy gives credence to our hypothesis that orbital interactions determine the preferred geometry (Fig. 49b).

Table 13. Interaction energies (kcal/mol) and structural parameters (Å) for $(F_3Bz)_2$. (a)[200]

Dimer	ΔE	Method	Basis set	R_{vert}	R_{slip}	SBO
$(F_3Bz)_2V$-TW S	-4.14	M06-2X	aug-cc-pVTZ	3.46	0.00	0.00
$(F_3Bz)_2V$-TW PD(+)	-5.56	M06-2X	aug-cc-pVTZ	3.21	1.40	2.00
$(F_3Bz)_2V$-TW PD(-)	-4.50	M06-2X	aug-cc-pVTZ	3.38	-0.88	2.00
$(F_3Bz)_2B$-TW S	-4.14	M06-2X	aug-cc-pVTZ	3.46	0.00	0.00
$(F_3Bz)_2B$-TW PD	-4.87	M06-2X	aug-cc-pVTZ	3.33	1.13	2.00
$(F_3Bz)_2V$-TW S	-4.95	SVWN	TZVP	3.37	0.00	0.00
$(F_3Bz)_2V$-TW PD(+)	-6.67	SVWN	TZVP	3.09	1.41	2.00
$(F_3Bz)_2V$-TW PD(-)	-5.39	SVWN	TZVP	3.25	-1.02	2.00
$(F_3Bz)_2B$-TW S	-4.96	SVWN	TZVP	3.37	0.00	0.00
$(F_3Bz)_2B$-TW PD	-5.82	SVWN	TZVP	3.18	1.22	2.00
$(F_3Bz)_2$TW PD[a]	-5.38	PIXEL		3.4 fixed		

a. Reference 200.

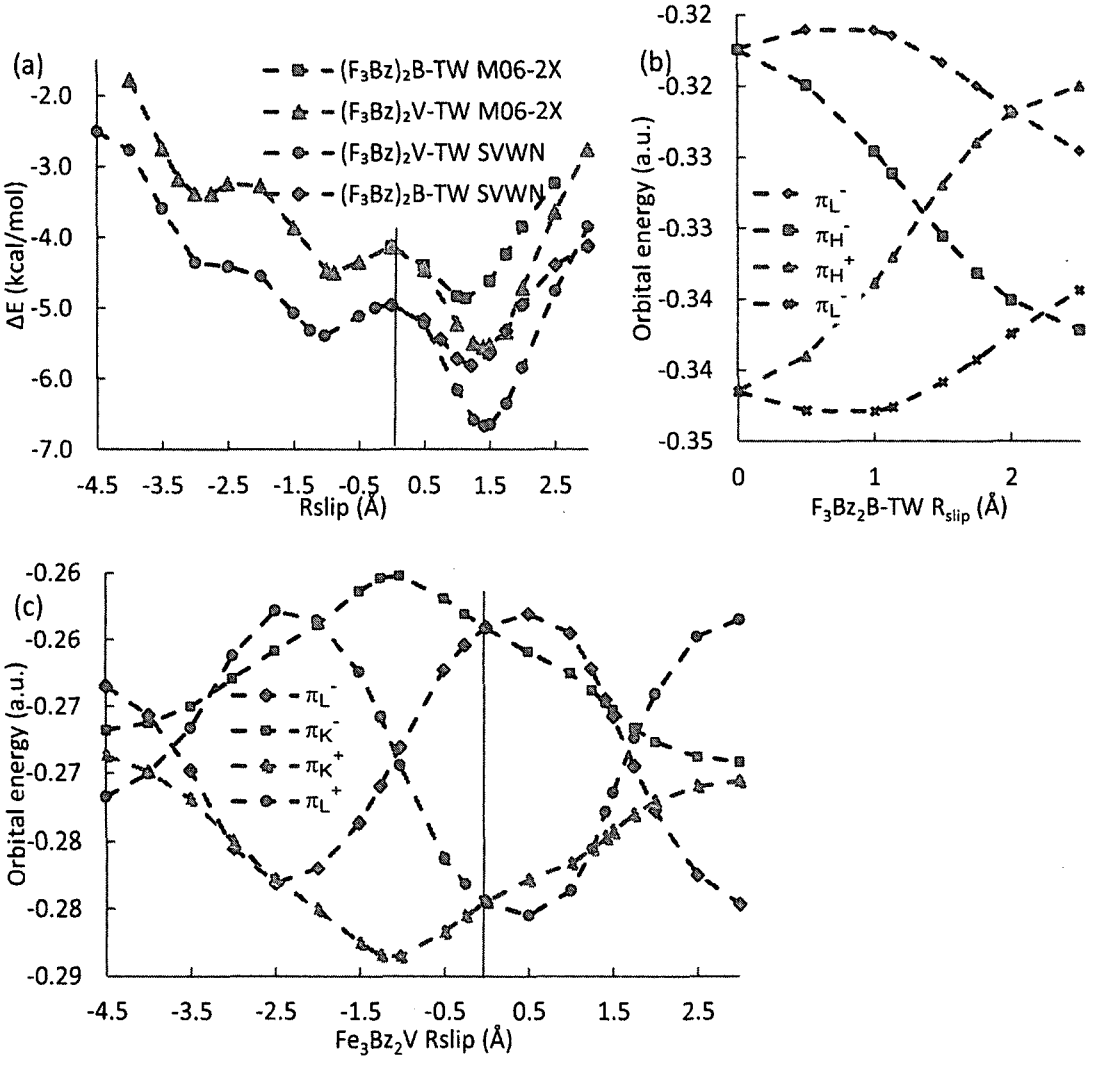

Figure 47. Potential energy curve and Walsh diagram for F_3Bz_2 (a) Potential energy curve for $(F_3Bz)_2$ as a function of parallel displacement (R_{slip} in Å) (b) Walsh diagram of the four M06-2X π-type orbitals for F_3Bz_2B-TW as a function of R_{slip}. (c) Walsh diagram of the four M06-2X π-type orbitals for F_3Bz_2V-TW as a function of R_{slip}.

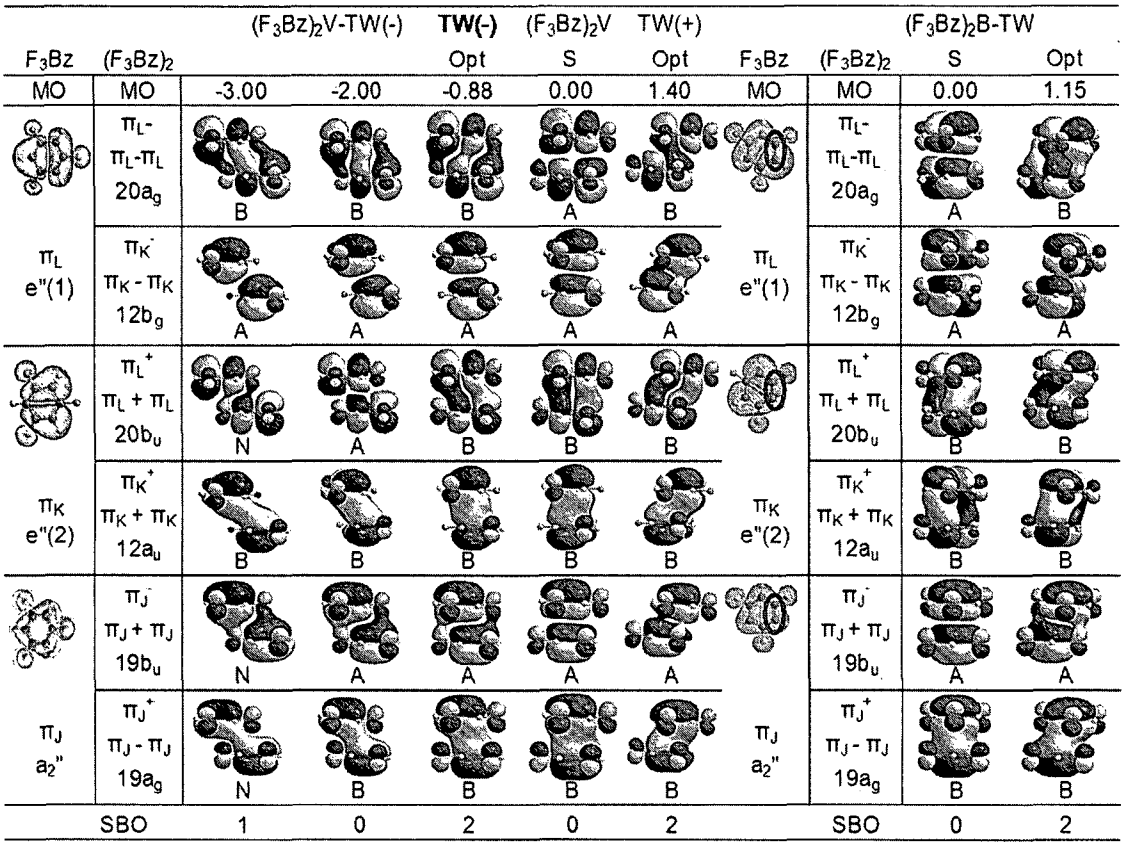

Figure 48. Representation of the six π-type orbitals of $(F_3Bz)_2V$-TW and $(F_3Bz)_2B$-TW as a function of R_{slip}. The isosurface is 0.010

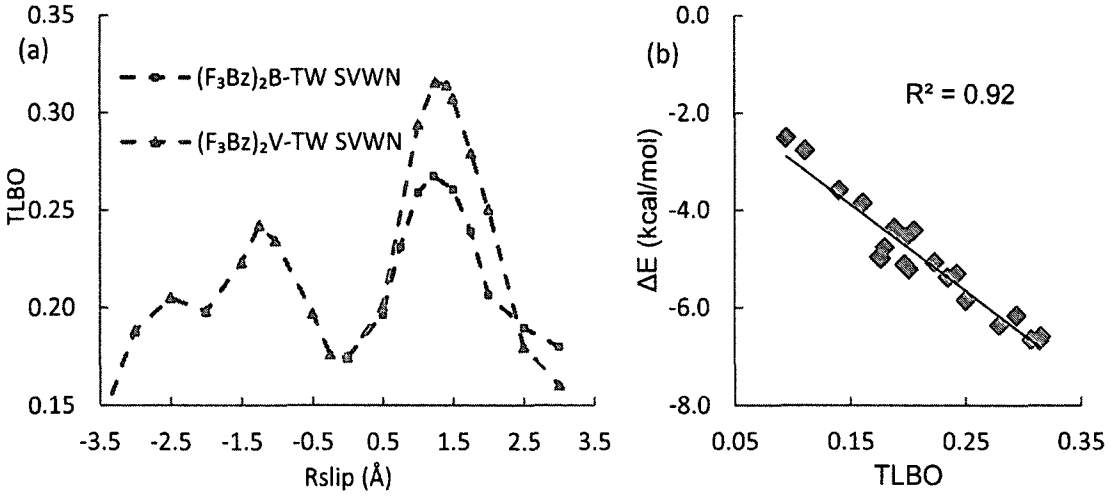

Figure 49. TLBO plots for $(F_3Bz_3)_2$. (a) The total inter-ring SVWN/TZVP Löwdin bond orders as a function of $R_{slip\ for}$ $(F_3Bz_3)_2$. (b) Plot of ΔE (kcal/mole) for both $(F_3Bz)_2B$-TW and $(F_3Bz)_2V$-TW

Hexafluorobenzene dimer

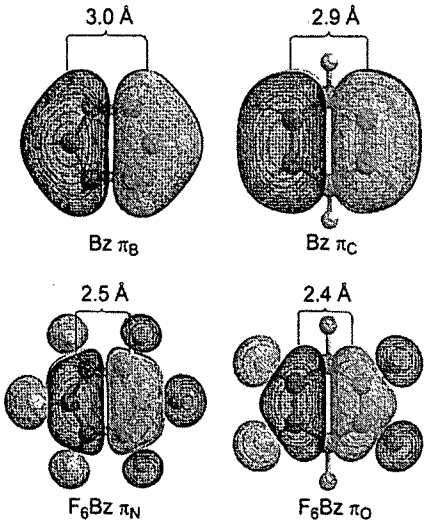

Figure 50. Comparison of orbitals from Bz and F_6Bz.

After examining the MO interactions in $(F_3Bz)_2$ we wanted to see if the same type of interactions were taking place in the hexafluorobenzene dimer $(F_6Bz)_2$ (Fig. 50). The structure of liquid hexafluorobenzene from liquid to super critical fluid was studied with neutron diffraction, and found that the liquid and to somewhat lesser extent, at the super critical region, had ordered structure with predominantly parallel structures but also had T-shaped structures.[261] The orbital representations, the Walsh diagram and the potential energy curve of $(F_6Bz)_2$ are similar to those of Bz_2 (Fig. 51a, 51c ,Fig 52 and Table 14). The similarities stem from Bz and F_6Bz monomers and dimers belonging to the same point group, D_{6h} (monomers) and C_{2h} (dimers). F_6Bz MO, π_O and π_N, are analogous to Bz MO π_C and π_B. Although they are similar, the differences between the Bz_2 and $(F_6Bz)_2$ dimers can be rationalized by the additional fluorine centered lobes that are on π_O and π_N. MO π_N^- of $(F_6Bz)_2V$ and π_O^- of $(F_6Bz)_2B$ have nodes perpendicular to the line of slip, and change from antibonding to bonding character along the slip, with an optimal R_{slip} of 1.31 Å, for $(F_6Bz)_2V$ and 1.28 Å for $(F_6Bz)_2B$, which is an average of 0.36 Å less than of Bz_2. We propose that the shorter optimal R_{slip} for $(F_6Bz)_2$ is a consequence of the shorter distance between the centers of the carbon containing lobes on MO π_N, π_O compared to Bz's π_B and π_C (Fig. 50).

The shorter distance means that the monomers will not have as far to travel for the like sign lobes to overlap. The potential energy curve of Both $(F_6Bz)_2$ geometries have distinct shoulders around R_{slip} of 3.0 Å, more so with $(F_6Bz)_2V$ than $(F_6Bz)_2B$, which is not seen in Bz_2 (Fig. 51a). We suggest the shoulders are the result of further weak in-phase orbital interactions past the optimal R_{slip} because of the additional fluorine centered lobes. The plot of the TLBO as a functions of R_{slip}, reveals a small increase of inter-ring electron density near 3.0 Å for $(F_6Bz)_2B$ and $(F_6Bz)_2V$. The TLBO plot gives further evidence of orbital interaction directing the optimal R_{slip} (Fig. 51b and 51d).

Table 14. Interaction energies (kcal/mol) and structural parameters (Å) for $(F_6Bz)_2$.

Dimer	ΔE	Method	Basis set	R_{vert}	R_{slip}	SBO
$(F_6Bz)_2$TW-S	-3.31	M06-2X	aug-cc-pVTZ	3.45	0.00	0
$(F_6Bz)_2$V-TW	-5.73	M06-2X	aug-cc-pVTZ	3.17	1.31	2
$(F_6Bz)_2$B-TW	-5.65	M06-2X	aug-cc-pVTZ	3.17	1.28	2
$(F_6Bz)_2$TW-S	-4.31	SVWN	TZVP	3.34	0.00	0
$(F_6Bz)_2$V-TW	-7.97	SVWN	TZVP	3.01	1.33	2
$(F_6Bz)_2$B-TW	-7.63	SVWN	TZVP	3.02	1.27	2

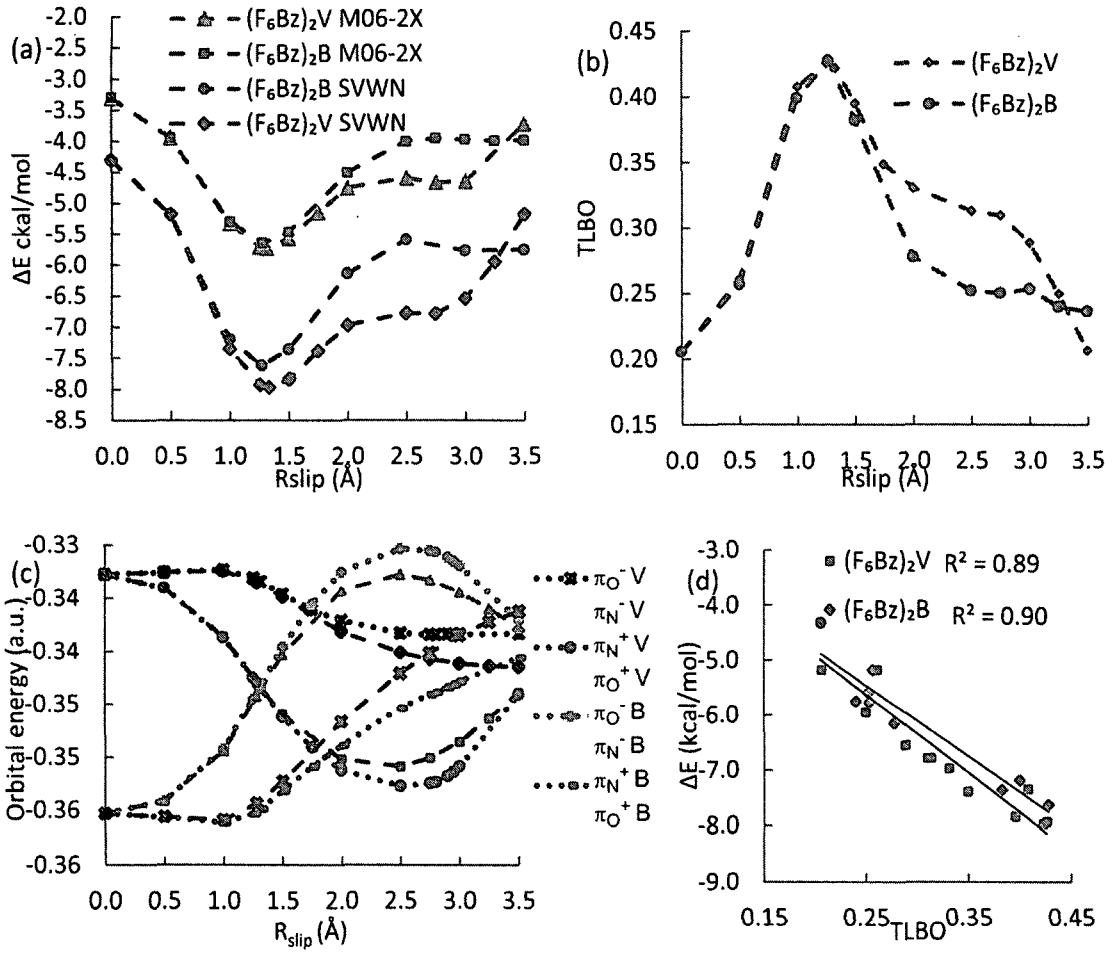

Figure 51. Potential energy curve, Walsh diagram and TLBO for $(F_6Bz_3)_2$. (a) Potential energy curve for $(F_6Bz)_2$ (M06-2X and SVWN) as a function of R_{slip}. (b) The SVWN/TZVP TLBO as a function of R_{slip} for $(F_6Bz_3)_2$. (c) Walsh diagram of the four π-type orbitals for F_6Bz_2 as a function of R_{slip}. (d) Plot of ΔE (kcal/mole) for both $(F_6Bz)_2B$ and $(F_6Bz)_2V$.

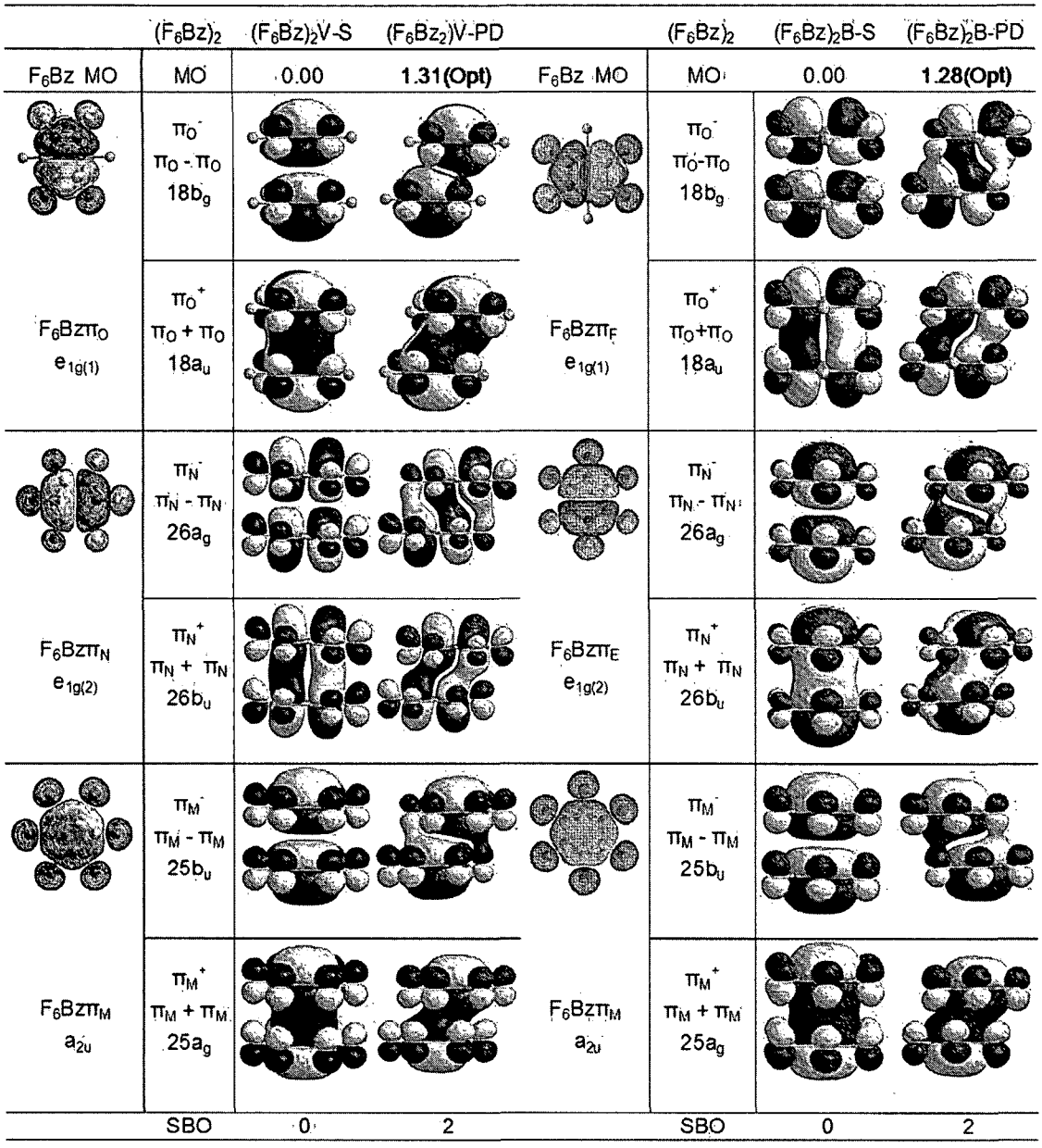

Figure 52. Representation of the six π-type orbitals of $(F_6Bz)_2V$ and $(F_6Bz)_2B$ as a function of R_{slip}. The isosurface is 0.010.

Benzene-hexafluorobenzene dimer

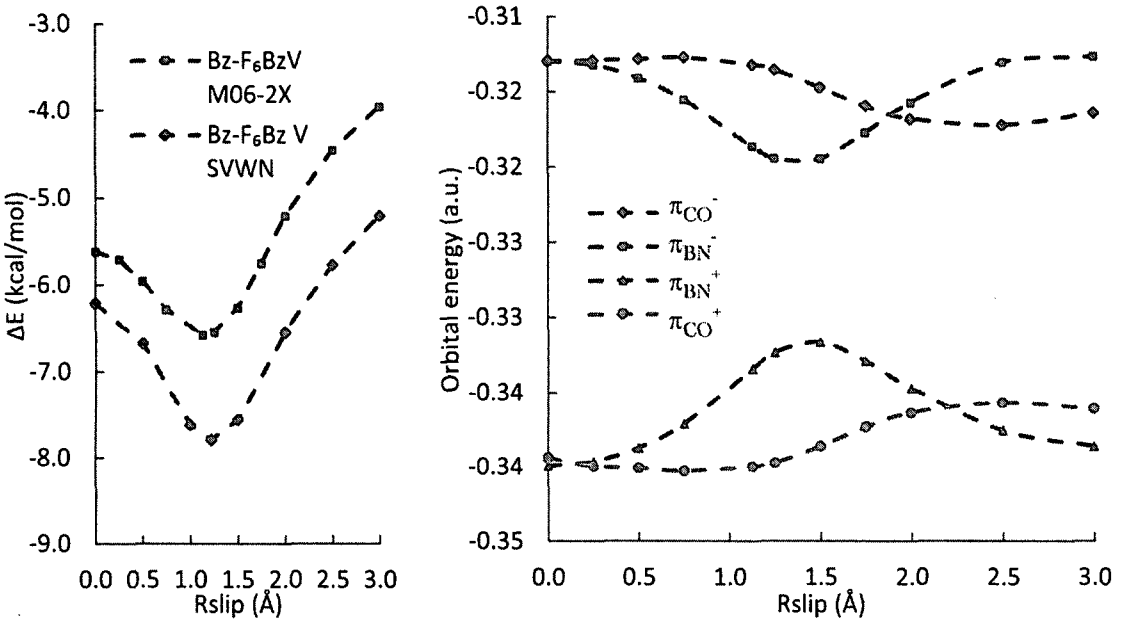

Figure 53. Potential energy curve and Walsh diagram for Bz-F_6BzV.

Table 15. Interaction energies (kcal/mol) and structural parameters (Å) for Bz-F_6Bz. a[262], b[263]

Dimer	ΔE (kcal/mol)	Method	Basis set	R_{vert} (Å)	R_{slip} (Å)	SBO
Bz-F_6Bz(S)	-5.62	M06-2X	aug-cc-pVTZ	3.44	0.00	0
Bz-F_6BzV	-6.58	M06-2X	aug-cc-pVTZ	3.26	1.13	2
Bz-F_6BzB	-6.56	M06-2X	aug-cc-pVTZ	3.28	1.12	2
Bz-F_6Bz (S)	-6.22	SVWN	TZVP	3.35	0.00	0
Bz-F_6BzV[a]	-5.38	CCSD(T)	basis set limit	3.50	1.00	
Bz-F_6BzV[b]	-7.42	MP2	631-+G**	3.40	1.00	

a. Reference 262, b. Reference 263.

The benzene-hexafluorobenzene dimer (Bz-F_6Bz) was examined in order to determine if the trends in orbital analysis could also be found in heterodimers. Mixing liquid Bz and F_6Bz forms a solid whose melting point is higher than either component,[264] and it is experimentally found to have a parallel geometry.[260] Bz has a large negative quadrupole moment -29.0 x 10^{-40} Cm^2 while F_6Bz has a large and positive value of 31.7 x 10^{-40} Cm^2.[258] Gung and Amicangelo's study suggests that if the quadrupole moment is the driving force for the geometry of the dimer, then S should be the lowest energy structure.[263] We found the Bz-F_6Bz-PD to be the lowest in energy, in agreement with other experimental and theoretical studies (Table 15 and Fig. 53).[262-263, 265-266] The S structure had a equal number of bonding and antibonding π-type MOs with a SBO of zero (Fig. 54). Although the monomers Bz and F_6Bz belong to the same point group, D_{6h}, the dimer is of C_S symmetry unlike the Bz_2 and $(F_6Bz)_2$ point group, C_{2h}. Point group C_{2h} has four symmetry operations so that the top four dimer MOs of Bz and F_6Bz each have a different reducible representation, but C_s only has two, identity and a horizontal mirror plane. The monomer MOs that have nodes perpendicular to the line of displacement π_N from F_6Bz and π_B from Bz combine to form π_{BN}^- and π_{BN}^+ Bz-F_6Bz dimer MOs, which belong to the same irreducible representation and therefore have an avoided crossing (Fig. 53 and 54). As π_{BN}^- and π_{BN}^+ approach each other in energy, they appear to repel each other as they mix together to form two new orbitals, one higher and one lower in energy, than the two that mixed. The maximum mixing appears to be at R_{slip} of 1.5 Å, producing two orbitals with non-bonding character and a SBO of zero. The optimal R_{slip} is 1.1 Å and a SBO of 2. The orbital interactions in Bz-F_6BzB were nearly identical to Bz-F_6BzV with π_{CO}^- and π_{CO}^+ experiencing an avoided crossing. The TLBO for Bz-F_6BzV along the slip is also optimized at 1.1 Å, leading to the conclusion that the short optimal R_{slip} for Bz-F_6BzV is a consequence of the non-bonding character of π_{BN}^- and π_{BN}^+ near the avoided crossing (Fig. 55a). The high correlation of the TLBO with respect to the interaction energy reveals the benefits of using the qualitative SBO to determine geometrical preferences (Fig. 55b).

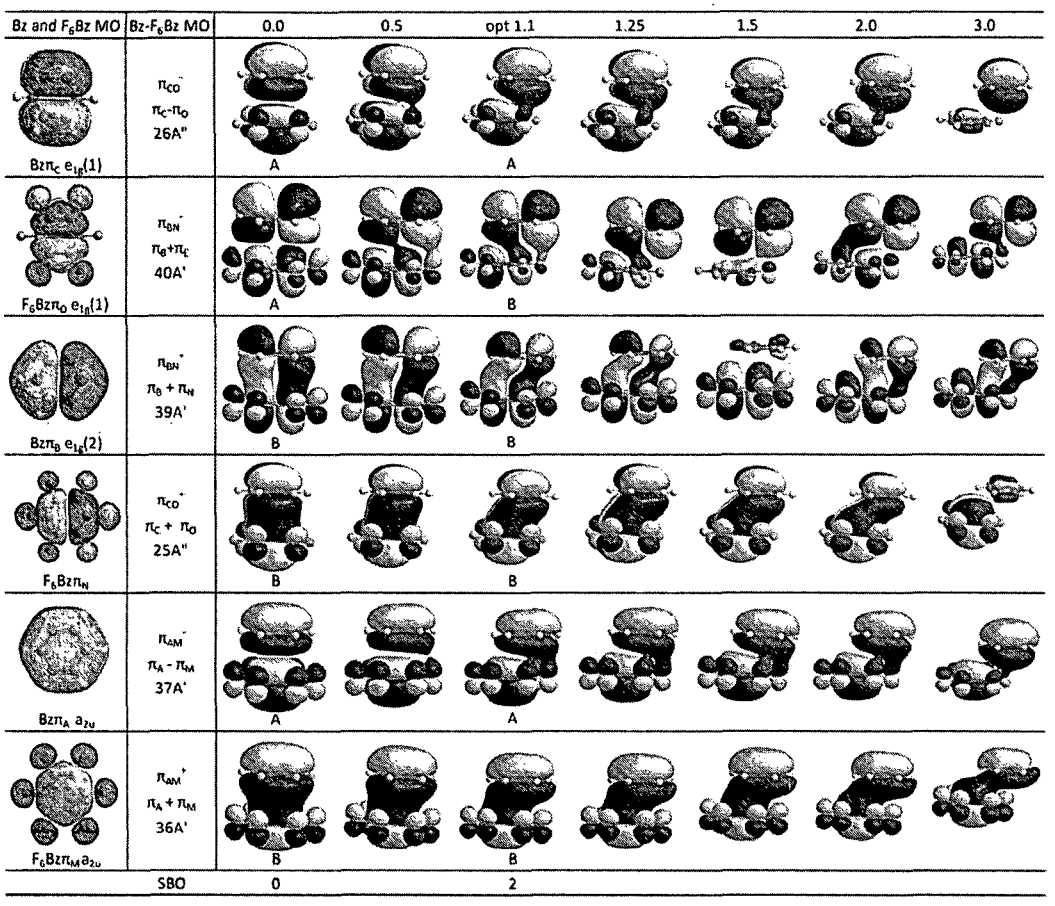

Figure 54. Representations of the top six dimer MOs of Bz-F_6Bz as a function of R_{slip}.

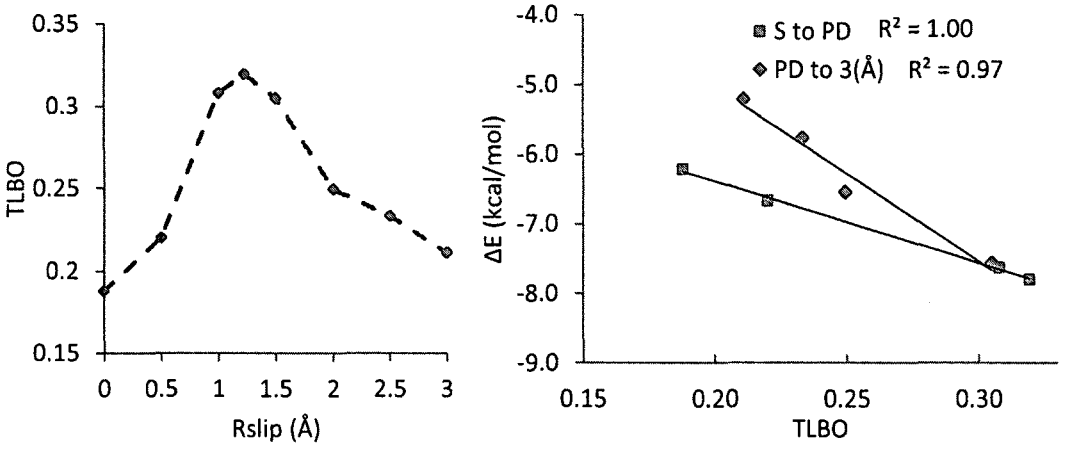

Figure 55. TLBO analysis for BzF_6Bz. (a) The total inter-ring SVWN/TZVP Löwdin bond orders as a function of $R_{slip\ for}$ Bz-F_6Bz. (b) Plot of ΔE (kcal/mole) for both Bz-F_6Bz.

Conclusion

In conclusion, our study extending the ideas of Chapter 4 to additional small dimers supports our hypothesis that orbital interactions determine their preferred geometry. From the results of this chapter, we propose the following general principles of π-stacking derived from orbital analysis:

(1) Stacked homo-dimers with an equal number of bonding and antibonding dimer MO's and a SBO of 0 will not form a π-stacking interaction.

(2) A dimer will slip to maximize overlap between monomers MOs with a node perpendicular to the line of slip. The dimer MO that is the antibonding combination of that monomer MO will change from antibonding to bonding character and increase the SBO at the optimal slip distance.

(3) The optimal R_{slip} distance is proportional to the distance between monomer lobes perpendicular to the line of slip. Rings will slip to maximize overlap between the largest lobes.

In the past, orbital interactions have been dismissed as a contribution to π-stacking because the interactions are so small. While the orbital interactions, so are the stacking energies themselves. The results of this study should encourage researchers that are studying systems involving π-stacking interactions to consider SBO and orbital interactions as part of their investigation. Visualizing the MO of monomers that will be involved in a π-stacked dimer gives qualitative insight into the preferred geometry of the dimer. Further development of these ideas and the extension to additional heterodimers could lead to a set of rules to predict favorable geometries in a wide variety of π-stacked systems.

CHAPTER 6

CONCLUSION

The large number of ZFs in cellular structures, as well as in viral and cancer cells, has caused there to be much interest in employing the reactivity of Zn/S sites and the effects of the released Zn^{2+} for therapeutic purposes. Zn^{2+}, the most common metal incorporated in proteins, is present in both catalytic and structural sites. The structural sites, called ZFs, are important as transcription factors that bind DNA and RNA. ZFs include motifs with three main types of binding domains, which include at least two cysteine, with an additional two cysteine or histidine, ligands. The concentration of Zn^{2+} in the cell and proteins is highly regulated, as it can be toxic in higher concentrations. The redox activity of the zinc bound thiolates in ZFs and in MT, regulate the concentration of Zn^{+2} by acting as zinc switches. Cys ligands can be oxidized with Zn^{+2} release and then reduced with restored binding. The release or binding of Zn^{2+} controls transcription recognition and other intercellular zinc signals. When Zn^{2+} is released the protein exists as random coils with no secondary or tertiary structure, and is no longer able to bind DNA or RNA.

The deactivation of ZF proteins through the oxidative release of the Zn^{2+} ion is an important theme for therapeutic intervention in cancer and viral illnesses. Our results using DFT calculations of r-S/Se compounds with three models of ZF proteins show that increasing the number of thiolate ligands coordinated to Zn^{2+} leads to stronger interactions with r-S/Se compounds due to the increase in the energy of the ZF HOMO. The high correlation between the LUMO energy of the r-S/Se compound and an increase in interaction energy, suggests that the LUMO energy of a potential drug could be used to test its ability to oxidize a ZF protein. Although the National Cancer Institute's drug screening program identified disulfide-substituted benzamides and benzisothiazolones as ZF reactive compounds, we found that Se derivatives of those compounds had stronger interactions with ZF proteins. Se compounds have been tested as chemopreventatives but have not been tested against the many viruses that contain ZF proteins. From the results of this study, the use of r-Se compounds as antivirals should be explored. Although

much was learned from the study of r-S/Se compounds with ZF models, the models were limited since they were constructed to represent only the coordinating residues. For future work, r-S/Se compounds would be modeled with the entire ZF protein, with a mixed quantum mechanics/molecular dynamics (QM/MM) program. We would also model the two CCCH ZFs in NCp7 since they have the same coordinating residues, but have different reactivities. The increased activity of the C terminal ZF could be caused by electronics or steric interactions. The largest problem with ZF reactive compounds is their lack specificity. The r-S/Se electrophilic compounds are not selective enough yet to be used as human oral antiviral and anticancer drugs. However, there does seem to be promise for r-S/Se compounds to be used as topical virucides that could inactivate the virus, or in the preparation of whole killed virus vaccines.

In an effort to produce compounds that can selectively inhibit ZF proteins, we targeted the binding site of the CCCH ZF NCp7 to DNA. We hypothesized that compounds that have stronger π-stacking interactions than DNA's Gau, to NCp7's Trp will block the ZF/Gua interaction and terminate the ZFs function. The increased molecular recognition of methylated nucleobases is attributed to the lowering of the base's LUMO energy which causes enhanced π-stacking interaction with Trp. Lowering the LUMO further with a $(NH_3)_3Pt/Pd$ group caused it to have an enhanced π-stacking interaction to MeInd/Trp. In our small model study of the interaction of methylated and metalated MeGua π-stacked with MeInd, we found there was a good correlation between the LUMO energy of the modified nucleobase and the π-stacking interaction energy. Because there also was a good correlation between the π-stacking energy and the experimental K_π value, we suggest that the LUMO energy of a modified nucleobase can give a quick estimate of its π-stacking potential. Because a strongest π-stacking energy was found for the interaction of $Pt(NH_3)_3(Xan)^{2+}$ with MeInd, additional purine derivatives should be tested, with a quick screening of their LUMO energies to find the most favorable derivative. For future work, the methylated and metalated MeGau and Xan would be placed in a full NCp7 protein using QM/MM. Additionally a molecular dynamics docking study could also be used to

see if the modified MeGua π-stacks with W in the binding site.

The π-stacking interactions in the binding site of the NCp7-DNA interaction prompted us to investing the orbital interactions involved those interactions. We were especially interested in why the S structure, which should maximize dispersion, is not the preferred geometry. By investigating the orbitals interactions in the benzene dimer, we found at the S structure there was an equal number of in-phase or bonding type MOs and out-of-phase or antibonding type MOs leading to a stacked bond order (SBO) of zero and an unfavorable interaction. We found that as the benzene monomers were slid away from each other one of the MOs with antibonding character changed to bonding character at the preferred optimal slip distance, changing the SBO to 2. The changing from antibonding to bonding character found at the optimal R_{slip} distance maximizes the inter-ring electron density as measured by both the intermolecular Wiberg indices (WBIs) and total Löwdin bond order (TLBO). In general a SBO=0 reflect a non-π-stacking interaction and a SBO > 0 reflects a stacking interaction. Upon further investigation of the orbital interactions in the pyridine, cytosine, and the polycyclic aromatic hydrocarbon dimers, naphthalene, anthracene and tetracene, we found trends similar to those of the benzene dimer. As described in Chapter 5, we used SBO to study the geometrical preferences for additional dimers, and were able to develop several general principles that can be used to rationalize the preferred geometries of a broad range of π-stacking interactions. We found the S structures of dimers have an equal number of bonding and antibonding dimer MO's and a SBO of 0, with an unfavorable π-stacking interaction. TW-S structures, with orbitals symmetrical to the twist, also have a SBO of 0. We conclude that the qualitative ideas of SBO can provide an intuitive tool for applications to engineered organic crystals, organic electronics, biological recognition motifs and other fields where non-covalent π-stacking interactions are important.

The use of DFT to investigate the intermolecular interactions involving donor acceptor compounds and π-stacking interactions of r-S/Se with ZF thiolates and methylated and metalated MeGua with MeInd, led to meaningful conclusions about the use of frontier orbital energies for predicting interaction strength. We were able to set

forth criteria for choosing the best compounds for maximizing interaction strength. We found that r-S/Se compounds with the lowest LUMOs had the strongest interactions with model ZF and, thus, may be potential targets for inhibiting ZF proteins for therapeutic purposes. We also found that the modified MeGua compound with the lowest LUMO had the strongest donor acceptor interaction with MeInd for give a quick estimate of interaction strength to help guide experimentalists in choosing promising compounds to test. Careful tuning of the LUMO energy by adding functional groups would be a preferred method of drug exploration over the method of testing whole libraries of compounds. The exploration of orbital interactions in π-stacked dimers led to a set of qualitative guideline for predicting preferred geometries for π-stacked compounds. The use of DFT, which is more cost efficient than post HF methods, to describe and interpret known chemistry and inquire into new chemistry, gave insight into the problems we were investigating that could not have be found experimentally.

REFERENCES

1. Cser, M. A.; Lasszlo, I. S.; Etienne, J.-C.; Maymard, Y.; Centeno, J. A.; Khassanova, L.; Collery, P. *Metal Ions in Biology and Medicine*. John Libbey Eurotext: Bastia, 2004; Vol. 8.

2. Shi, W.; Zhan, C.; Ignatov, A.; Manjasetty, B. A.; Marinkovic, N.; Sullivan, M.; Huang, R.; Chance, M. R. *Structure* **2005,** *13*, 1473-1486.

3. McCance, R. A.; Widdowson, E. M. *Biochem. J.* **1942,** *36*, 692-696.

4. Schwabe, J. W. R.; Klung, A. *J. Struct. Biol.* **1994,** *1*, 354-349.

5. Berg, J. M.; Shi, Y. *Science* **1996,** *271*, 1081-1085.

6. Permyakov, E. *Metalloproteomics*. John Wiley and Sons, Inc: Hoboken, 2009.

7. Reddi, A. R.; Guzman, T. R.; Breece, R. M.; Tierney, D. L.; Gibney, B. R. *J. Am. Chem. Soc.* **2007,** *129*, 12815-12827.

8. Klug, A.; Rhodes, D. *Cold Spring Harb. Symp. Quant. Biol.* **1987** *52*, 473-482.

9. Lippard, S. J.; Berg, J. M. *Principles of Bioinorganic Chemistry*. University Science Books: Mill Valley, 1994.

10. Klug, A.; Schwabe, J. W. *FASEB J.* **1995,** *9*, 597-604.

11. Iuchi, S.; Kuldell, N. *Zinc Finger Proteins: From Atomic Contact to Cellular Function*. Kluwer Academic/ Plenum Publishers: New York, 2005.

12. Maret, W. *Biochemistry* **2004,** *43*, 3301-3309.

13. Krishna, S. D.; Majumdar, I.; Grishin, N. V. *Nucleic Acids Res.* **2003,** *31*, 532-550.

14. Lee, Y.-M.; Lim, C. *J. Am. Chem. Soc.* **2011,** *133*, 8691-8703.

15. Maret, W. *J. Nutr.* **2000,** *130*, 1455S-1458S.

16. Anzellotti, A. I.; Farrell, N. P. *Chem. Soc. Rev.* **2008,** *37*, 1629-1651.

17. Simons, T. J. B. *J. Membr. Biol.* **1991,** *123*, 63-71.

18. Maret, W.; Vallee, B. L. *Proc. Natl. Acad. Sci. USA* **1998,** *95*, 3478-3482.

19. Bayse, C. A.; Whitty, S. M.; Antony, S. *Curr. Chem. Biol.* **2013,** *7*, 57-64.

20. Maret, W. *Antioxid. Redox Signaling* **2006,** *8*, 1419-1441.

21. Webster, K.; Prentice, H.; Bishopric, N. *Antioxid. Redox Signaling* **2001,** *3*, 535-548.

22. Haase, H.; Rink, L. *Annu. Rev. Nutr.* **2009,** *29*, 133–152.

23. Kröncke, K.-D.; Klotz, L.-O. *Antioxid. Redox Signaling* **2009,** *11*, 1015-1027.

24. Ott, D. E.; Hewes, S. M.; Alvord, W. G.; Henderson, L. E.; Arthur, L. O. *Virology* **1998,** *243*, 283-292.

25. Boukhvalova, M.; Prince, G.; Blanco, J. *Virol. J.* **2010,** *7*, 20-1 - 20-10.

26. Beerheide, W.; Bernard, H.-U.; Tan, Y.-J.; Ganesan, A.; Rice, W.; Ting, A. *J. Natl. Cancer Inst.* **1999,** *91*, 1211-1220.

27. Blessing, H.; Kraus, S.; Heindl, P.; Bal, W.; Hartwig, A. *Eur. J. Biochem.* **2004,** *271*, 3190-3199.

28. Chabner, B. A.; Longo, D. L. *Cancer Chemotherapy and Biotherapy: Principles and Practice*. Lippincott-Raven Publishers: Frederick, Maryland, 1996.

29. Wilkinson, D.; Tholandi, M.; Ramjee, G.; Rutherford, G. W. *Lancet Infect. Dis.* **2002,** 613-617.

30. Turpin, J. A.; Schito, M. L.; Miller Jenkins, L. M.; Inman, J. K.; Appella, E. *Adv. Pharmacol.* **2008,** *56*, 229-256.

31. Rice, W.; Supko, J.; Malspeis, L.; Buckheit, R.; Clanton, D.; Bu, M.; Graham, L.; Schaeffer, C.; Turpin, J.; Domagala, J. *Science* **1995,** *270*, 1194 - 1197.

32. Maynard, A. T.; Huang, M.; Rice, W. G.; Covell, D. G. *Proc. Natl. Acad. Sci. U.S.A* **1998,** *95*, 11578-11583.

33. Domagala, J. M.; Bader, J. P.; Gogliotti, R. D.; Sanchez, J. P.; Stier, M. A.; Song, Y.; Vara Prasad, J. V. N.; Tummino, P. J.; Scholten, J.; Harvey, P.; Holler, T.; Gracheck, S.; Hupe, D.; Rice, W. G.; Schultz, R. *Bioorg. Med. Chem.* **1997,** *5*, 569-579.

34. Loo, J. A.; Holler, T. P.; Sanchez, J.; Gogliotti, R.; Maloney, L.; Reily, M. D. *J. Med. Chem.* **1996,** *39*, 4313-4320.

35. El-Bayoumy, K.; Das, A.; Narayanan, B.; Narayanan, N.; Fiala, E. S.; Desai, D.; Rao, C. V.; Amin, S.; Sinha, R. *Carcinogenesis* **2006,** *27*, 1369-1376.

36. El-Bayoumy, K.; Sinha, R. *Mutat. Res-Fund. Mol. M.* **2004,** *551*, 181-197.

37. Garcia, C. C.; Damonte, E. B. *Infect. Disord. Drug Targets* **2007,** *7*, 204-212.

38. Witkiewicz-Kucharczyk, A.; Bal, W. *Toxicol. Lett.* **2006,** *162*, 29-42.

39. Hisahiro, K.; Mariko, T.; Mitsunobo, D.; Toshimasa, I. *FEBS Lett.* **1995,** *370*, 193-196.

40. Anzellotti, A. I.; Ma, E. S.; Farrell, N. *Inorg. Chem.* **2005,** *44*, 483-485.

41. Anzellotti, A. I.; Sabat, M.; Farrell, N. *Inorg. Chem.* **2006,** *45*, 1638-1645.

42. Anzellotti, A. I.; Liu, Q.; Bloemink, M. J.; Scarsdale, J. N.; Farrell, N. *Chem. Biol.* **2006,** *13*, 539-548.

43. Szabo, A.; Ostlund, N. S. *Modern Quantum Chemistry*. Dover Publications, Inc.: New York, 1989.

44. Levine, I. N. *Quantum Chemistry*. 6th ed.; Pearson Education, Inc.: Upper Saddle River, 2009.

45. McQuarrie, D. A. *Quantum Chemistry*. 2nd ed.; University Science Books: Sausalito, California, 2008.

46. Cramer, C. J. *Essentials of Computational Chemistry Theories and Models*. John Wiley & Sons Ltd.: Hoboken, 2004.

47. Foresman, J. B.; Frisch, Æ. *Exploring Chemistry with Electronic Structure Methods*. 2nd ed.; Gaussian, Inc.: Pittsburgh, 1996.

48. Bultinck, P.; Winter, H. D.; Langenaeker, W.; Tollenaere, J. P. *Computational Medicinal Chemistry for Drug Discovery*. Marcel Dekker, Inc.: New York, 2004.

49. Møller, C.; Plesset, M. S. *Phys. Rev. 46*, 618-622.

50. Maurice, D.; Head-Gordon, M. *Mol. Phys.* **1999,** *96*, 1533-1541.

51. Purvis, G. D.; Bartlett, R. J. *J.Chem. Phys.* **1982,** *76*, 1910-1918.

52. Lewars, E. *Computational Chemistry Introduction to the Theory and Applications of Molecular and Quantum Mechanics*. Kluwer Academic Publishers: Boston, 2003.

53. Koch, W.; Holthausen, M. C. *A Chemist's Guide to Density Functional Theory*. Second Edition ed.; Wiley-VCH: New York, 2001.

54. Kohn, P. H. a. W. *Phys. Rev.* **1964,** *136*, B864-B871.

55. Kohn, W.; Sham, L. J. *Phys. Rev.* **1965,** *140*, A1133–A1138.

56. Parr, R.; Yang, W. *Density-Functional Theory of Atoms and Molecules*. Oxford University Press: New York, 1989.

57. Vosko, S. H.; Wilk, L.; Nusair, M. *Can. J. Phys.* **1980,** *58*, 1200-1211.

58. Perdew, J. P.; Burke, K.; Ernzerhof, M. *Phys. Rev. Lett.* **1996,** *77*, 3865-3868.

59. Perdew, J. P.; Chevary, J. A.; Vosko, S. H.; Jackson, K. A.; Pederson, M. R.; Singh, D. J.; Fiolhais, C. *Phys. Rev. B* **1992,** *46*, 6671-6687.

60. Becke, A. D. *Phys. Rev. A* **1988,** *38*, 3098-3100.

61. Lee, C.; Yang, W.; Parr, R. G. *Phys. Rev. B* **1988,** *37*, 785-789.

62. Becke, A. D. *J. Chem. Phys.* **1996,** *104*, 1040-1046.

63. Becke, A. D. *J. Chem. Phys.* **1993,** *98*, 5648-5653.

64. Becke, A. D. *J. Chem. Phys.* **1997,** *107*, 8554-8560.

65. Jensen, F. *Introduction to Computational Chemistry*. John Wiley & Sons: New York, 1999.

66. Boys, S. F. *Proc. R. Soc. A* **1950,** *200*, 542-554.

67. Ditchfield, R.; Hehre, W. J.; Pople, J. A. *J. Chem. Phys.* **1971,** *54*, 724-729.

68. Woon, D. E.; Dunning, J., T. H. , *J. Chem. Phys.* **1993,** *98*, 1358-1371.

69. Schäfer, A.; Horn, H.; Ahlrichs, R. *J. Chem. Phys.* **1992,** *97*, 2571-2577.

70. Bourlès, E.; Isaac, M.; Lebrun, C.; Latour, J.-M.; Sénèque, O. *Chem. Eur. J.* **2011,** *17*, 13762-13772.

71. Ciofani, R.; Makrlík, L. *Zinc Fingers Structure, Properties and Applications*. Nova Science Publishers, Inc.: New York, 2012.

72. Leon, O.; Roth, M. *Biol. Res.* **2000,** *33*, 21-30.

73. Stillman, M. J.; Shaw, C. F.; Suzuki, K. T. *Metallothionein: Synthesis, Structure, and Properties of Metallothioneins, Phytochelatins, and Metal-Thiolate Complexes*. VCH Publishers: New York, 1992.

74. Dillon, P. F. *Biophysics: A Physiological Approach*. Cambridge University Press: New York, 2012.

75. Oka, S.; Shiraishi, Y.; Yoshida, T.; Ohkubo, T.; Sugiura, Y.; Kobayashi, Y. *Biochemistry* **2004,** *43*, 16027-16035.

76. Ikegami, T.; Kuraoka, I.; Saijo, M.; Kodo, N.; Kyogoku, Y.; Morikawa, K.; Tanaka, K.; Shirakawa, M. *Nat. Struct. Biol.* **1998,** *5*, 701-706.

77. Bampi, C.; Jacquenet, S.; Lener, D.; Décimo, D.; Darlix, J.-L. *Int. J. Biochem. Cell Biol.* **2004,** *36*, 1668-1686.

78. Dorfman, T.; Luban, J.; Goff, S. P.; Haseltine, W. A.; Göttlinger, H. G. *J. Virol.* **1993,** *67*, 6159-6169.

79. Freed, E. O. *Virology* **1998,** *251*, 1-15.

80. Reeves, J. D.; Piefer, A. J. *Drugs* **2005,** *65*, 1747-1766.

81. Hartman, T. L.; Buckheit Jr, R. W. *Mol. Biol. Int.* **2012**, 1-17.

82. Engelman, A.; Cherepanov, P. *Nat. Rev. Micro.* **2012,** *10*, 279-290.

83. Topol, I. A.; McGrath, C.; Chertova, E.; Dasenbrock, C.; Lacourse, W. R.; Eissenstat, M. A.; Burt, S. K.; Henderson, L. E.; Casas-Finel, J. R. *Prot. Sci.* **2001,** *10*, 1434-1445.

84. Jacob, C.; Maret, W.; Vallee, B. L. *Biochem. Biophys. Res. Comm.* **1998,** *248*, 569-573.

85. McDonnell, N. B.; De Guzman, R. N.; Rice, W. G.; Turpin, J. A.; Summers, M. F. *J. Med. Chem.* **1997,** *40*, 1969-1976.

86. Jacob, C.; Maret, W.; Vallee, B. L. *Proc. Natl. Acad. Sci. U.S.A* **1999,** *96*, 1910-1914.

87. Tummino, P. J.; Harvey, P. J.; McQuade, T.; Domagala, J.; Gogliotti, R.; Sanchez, J.; Song, Y.; Hupe, D. *Antimicrob. Agents* **1997,** *41*, 394-400.

88. Huang, M.; Maynard, A.; Turpin, J. A.; Graham, L.; Janini, G. M.; Covell, D. G.; Rice, W. G. *J. Med. Chem.* **1998,** *41*, 1371-1381.

89. Barone, V.; Bencini, A.; Fantucci, P. Recent Advances in Density Functional Methods Part III. In *Recent Advances in Computational Chemistry*, Chong, D. P., Ed. World Scientific Publishing Co. Pte. Ltd.: River Edge, 2002; Vol. 1, pp 325-338.

90. Chertova, E.; Crise, B. J.; Morcock, D. R.; Bess, J. W.; Henderson, L. E.; Lifson, J. D. *Curr. Mol. Med.* **2003,** *3*, 265-272.

91. Riedmann, E. M. *Hum. Vaccin. Immunother.* **2013,** *9*, 7-10.

92. García, C. C.; Djavani, M.; Topisirovic, I.; Borden, K. L. B.; Salvato, M. S.; Damonte, E. B. *J. Gen. Virol.* **2006,** *87*, 1217-1228.

93. Larabee, J. L.; Hocker, J. R.; Hanas, R. J.; Kahn, F. M.; Hanas, J. S. *Biochem. Pharm.* **2002,** *64*, 1757-1765.

94. Woo Youn, B.; Fiala, E. S.; Soon Sohn, O. *Nutr. Cancer* **2001,** *40*, 28-33.

95. Facompre, N. D.; El-Bayoumy, K.; Sun, Y.-W.; Pinto, J. T.; Sinha, R. *Cancer Prev. Res.* **2010,** *3*, 975-984.

96. Chen, Y.; Maret, W. *Antioxid. Redox Signaling* **2001,** *3*, 651-656.

97. Frisch, M. J.; Trucks, G. W.; Schlegel, H. B.; Scuseria, G. E.; Robb, M. A.; Cheeseman, J. R.; Scalmani, G.; Barone, V.; Mennucci, B.; Petersson, G. A.; Nakatsuji, H.; Caricato, M.; Li, X. H., H. P.; Izmaylov, A. F.; Bloino, J.; Zheng, G.; Sonnenberg, J. L.; Hada, M. E., M.; Toyota, K. F., R.; Hasegawa, J.; Ishida, M.; Nakajima, T.; Honda, Y.; Kitao, O. N., H.; Vreven, T.; Montgomery, J. A., Jr.; Peralta, J. E.; Ogliaro, F.; Bearpark, M.; Heyd, J. J.; Brothers, E.; Kudin, K. N.; Staroverov, V. N.; Kobayashi, R.; Normand, J.; Raghavachari, K.; Rendell, A.; Burant, J. C.; Iyengar, S. S.; Tomasi, J.; Cossi, M.; Rega, N.; Millam, N. J.; Klene, M.; Knox, J. E.; Cross, J. B.; Bakken, V.; Adamo, C.; Jaramillo, J.; Gomperts, R.; Stratmann, R. E.; Yazyev, O.; Austin, A. J.; Cammi, R. P., C.; Ochterski, J. W.; Martin, R. L.; Morokuma, K.; Zakrzewski, V. G.; Voth, G. A.; Salvador, P.; Dannenberg, J. J.; Dapprich, S.; Daniels, A. D.; Farkas, Ö.; Foresman, J. B.; Ortiz, J. V.; Cioslowski, J.; Fox, D. J. *Gaussian 09, Revision D.01,*, Gaussian 09: Gaussian, Inc., Wallingford CT, 2009.

98. Perdew, J. P. *Electronic Structure of Solids*. Akademie Verlag: Berlin, 1991; Vol. 11.

99. Tao, J. M.; Perdew, J. P.; Staroverov, V. N.; Scuseria, G. E. *Phys. Rev. Lett.* **2003,** *91*, 146401-146405.

100. Remya, K.; Suresh, C. H. *J. Comput. Chem.* **2013,** *34*, 1341-1353.

101. Dunning, T. H. *J. Chem. Phys.* **1971,** *55*, 716-723.

102. Hurley, M. M.; Pacios, L. F.; Christiansen, P. A.; Ross, R. B.; Ermler, W. C. *J. Chem. Phys.* **1986,** *84*, 6840-6853.

103. Wadt, W. R.; Hay, P. J. *J. Chem. Phys.* **1985,** *82*, 284-298.

104. Glendening, A. E.; Reed, J. E.; Carpenter; Weinhold., F. *NBO Version 3.1*, Madison, 1980.

105. Wiberg, K. B. *Tetrahedron* **1968,** *24*, 1083-1096.

106. Znamenskyi, V. S.; Green, M. E. *J. Chem. Theory Comput.* **2007,** *3*, 103-114.

107. Parr, R. G.; Pearson, R. G. *J. Am. Chem. Soc.* **1983,** *105*, 7512-7516.

108. Parr, R. G.; Donnelly, R. A.; Levy, M.; Palke, W. E. *J. Chem. Phys.* **1978,** *68*, 3801-3807.

109. Almbladh, C. O.; von Barth, U. *Phys. Rev. B* **1985,** *31*, 3231-3244.

110. Zhan, C.-G.; Nichols, J. A.; Dixon, D. A. *J. Phys. Chem. A* **2003,** *107*, 4184-4195.

111. Bayse, C. A.; Pavlou, A. *Org. Biomol. Chem.* **2011,** *9*, 8006-8015.

112. Barton, D. H. R.; Hall, M. B.; Lin, Z.; Parekh, S. I.; Reibenspies, J. *J. Am. Chem. Soc.* **1993,** *115*, 5056-5059.

113. Mukherjee, A. J.; Zade, S. S.; Singh, H. B.; Sunoj, R. B. *Chem. Rev.* **2010,** *110*, 4357-4416.

114. Fleming, I. *Molecular Orbitals and Organic Chemical Reactions*. John Wiley and Sons, Ltd: Chichester, 2010.

115. Jones, R. A. Y. *Physical and Mechanistic Organic Chemistry*. Cambridge University Press: New York, 1979.

116. Bayse, C. A.; Baker, R. A.; Ortwine, K. N. *Inorg. Chim. Acta* **2005,** *358*, 3849-3854.

117. Rauk, A. *Orbital Interaction Theory of Organic Chemistry*. 2nd ed.; Wiley-Interscience: New York, 2001.

118. Topol, I. A.; Casas-Finet, J. R.; Gussio, R.; Burt, S. K.; Erickson, J. W. *J. Mol. Struct.* **1998,** *423*, 13-28.

119. Alberts, I. L.; Nadassy, K.; Wodak, S. J. *Prot. Sci.* **1998,** *7*, 1700-1716.

120. Dabrowiak, J. C. *Metals in medicine*. Wiley: Hoboken, , 2009.

121. Roe, R. R.; Pang, Y.-P. *J. Mol. Model.* **1999,** *5*, 134-140.

122. Moggach, S. A.; Allan, D. R.; Parsons, S.; Sawyer, L.; Warren, J. E. *J. Synchrotron Radiat.* **2005,** *12*, 598-607.

123. Dahaoui, S.; Pichon-Pesme, V.; Howard, J. A. K.; Lecomte, C. *J. Phys. Chem. A* **1999,** *103*, 6240-6250.

124. Hagen, A. P. *Reactions Catalyzed by Inorganic Compounds.* Weinheim: Deerfield Beach, 1993; Vol. 16.

125. Antony, S.; Bayse, C. A. *Inorg. Chem.* **2013,** *52*, 13803-13805.

126. Parnham, M. J.; Sies, H. *Biochem. Pharm.* **2013,** *86*, 1248-1253.

127. Meotti, F. C.; Borges, V. C.; Zeni, G.; Rocha, J. B. T.; Nogueira, C. W. *Toxicol. Lett.* **2003,** *143*, 9-16.

128. Sies, H. *Free Radic. Bio. Med.* **1993,** *14*, 313-323.

129. Antony, S.; Bayse, C. A. *Inorg. Chem.* **2011,** *50*, 12075-12084.

130. Topol, I. A.; Nemukhin, A. V.; Chao, M.; Iyer, L. K.; Tawa, G. J.; Burt, S. K. *J. Am. Chem. Soc.* **2000,** *122*, 7087-7094.

131. Larabee, J. L.; Hocker, J. R.; Hanas, J. S. *J. Inorg. Biochem.* **2009,** *103*, 419-426.

132. Coffin, J. M. *Science* **1995,** *267*, 483-489.

133. Whiteside, A. *HIV/AIDS: a Very Short Introduction*. Oxford University Press: New York, 2008.

134. Fan, H.; Conner, R. F.; Villarreal, L. P. *AIDS: Science and Society*. Jones & Bartlett Learning: Burlington, 2014.

135. Das, K.; Arnold, E.; Hughes, S. Nonnucleoside Reverse Transcriptase Inhibitors (NNRTIs). In *Human Immunodeficiency Virus Reverse Transcriptase*, LeGrice, S.; Gotte, M., Eds. Springer New York: 2013; pp 123-139.

136. Heider, D.; Senge, R.; Cheng, W.; Hüllermeier, E. *Bioinformatics* **2013,** *29*, 1946-1952.

137. Neamati *Wiley Series in Drug Discovery and Development : HIV-1 Integrase : Mechanism and Inhibitor Design*. Wiley: Somerset, 2011.

138. Robinson, H. L. *Nat. Rev. Immunol.* **2002,** *2*, 239-250.

139. Barklis, E. Virus Assembly as a Target for Antiretroviral Therapy. In *Advances in HIV-1 Assembly and Release*, Freed, E. O., Ed. Springer New York: 2013; pp 185-214.

140. Musah, R. A. *Curr. Top. Med. Chem.* **2004,** *4*, 1605-1622.

141. Summers, M. F.; Henderson, L. E.; Chance, M. R.; South, T. L.; Blake, P. R.; Perez-Alvarado, G.; Bess, J. W.; Sowder, R. C.; Arthur, L. O.; Sagi, I.; Hare, D. R. *Prot. Sci.* **1992,** *1*, 563-574.

142. Tanchou, V.; Gabus, C.; Rogemond, V.; Luc Darlix, J. *J. Mol. Biol.* **1995,** *252*, 563-571.

143. Darlix, J.-L.; Lapadat-Tapolsky, M.; de Rocquigny, H.; Roques, B. P. *J. Mol. Biol.* **1995,** *254*, 523-537.

144. Demene, H.; Dong, C. Z.; Ottmann, M.; Rouyez, M. C.; Jullian, N.; Morellet, N.; Mely, Y.; Darlix, J. L.; Fournie-Zaluski, M. C. *Biochemistry* **1994,** *33*, 11707-11716.

145. Gorelick, R. J.; Fu, W.; Gagliardi, T. D.; Bosche, W. J.; Rein, A.; Henderson, L. E.; Arthur, L. O. *J. Virol.* **1999,** *73*, 8185-8195.

146. Gorelick, R. J.; Nigida, S. M.; Bess, J. W.; Arthur, L. O.; Henderson, L. E.; Rein, A. *J. Virol.* **1990,** *64*, 3207-3211.

147. Topol, I. A.; Nemukhin, A. V.; Dobrogorskaya, Y. I.; Burt, S. K. *J. Phys. Chem. B* **2001,** *105*, 11341-11350.

148. Huang, Y.; Khorchid, A.; Wang, J.; Parniak, M. A.; Darlix, J. L.; Wainberg, M. A.; Kleiman, L. *J. Virol.* **1997,** *71*, 4378-84.

149. Lapadat-Tapolsky, M.; Rocquigny, H. D.; Gent, D. V.; Roques, B.; Plasterk, R.; Darlix, J.-L. *Nucleic Acids Res.* **1993,** *21*, 831-839.

150. Morellet, N.; Déméné, H.; Teilleux, V.; Huynh-Dinh, T.; de Rocquigny, H.; Fournié-Zaluski, M.-C.; Roques, B. P. *J. Mol. Biol.* **1998,** *283*, 419-434.

151. Morellet, N.; de Rocquigny, H.; Mély, Y.; Jullian, N.; Déméné, H.; Ottmann, M.; Gérard, D.; Darlix, J. L.; Fournie-Zaluski, M. C.; Roques, B. P. *J. Mol. Biol.* **1994,** *235*, 287-301.

152. Vuilleumier, C.; Bombarda, E.; Morellet, N.; Gérard, D.; Roques, B. P.; Mély, Y. *Biochemistry* **1999,** *38*, 16816-16825.

153. Mori, M.; Dietrich, U.; Manetti, F.; Botta, M. *J. Chem. Inf. Model.* **2010,** *50*, 638-650.

154. Mely, Y.; deRocquigny, H.; Shvadchak, V.; Avilov, S.; Dietrich, C. Z. D.; Darlix, J.-L. *Mini-Rev. Med. Chem.* **2008,** *8*, 24-35.

155. Yamagata, Y.; Kato, M.; Odawara, K.; Tokuno, Y.; Nakashima, Y.; Matsushima, N.; Yasumura, K.; Tomita, K.-I.; Ihara, K.; Fujii, Y.; Nakabeppu, Y.; Sekiguchi, M.; Fujii, S. *Cell* **1996,** *86*, 311-319.

156. Labahn, J.; Schärer, O. D.; Long, A.; Ezaz-Nikpay, K.; Verdine, G. L.; Ellenberger, T. E. *Cell* **1996,** *86*, 321-329.

157. Hodel, A. E.; Gershon, P. D.; Shi, X.; Wang, S.-M.; Quiocho, F. A. *Nat. Struct. Biol.* **1997,** *4*, 350-354.

158. Marcotrigiano, J.; Ging, A.-C.; Sonenberg, N.; Burley, S. K. *Cell* **1997,** *89*, 951-961.

159. Ishida, T.; Katsuta, M.; Inoue, M.; Yamagata, Y.; Tomita, K.-i. *Biochem. Biophys. Res. Comm.* **1983,** *115*, 849-854.

160. Pullman, B.; Pullman, A. *Proc. Natl. Acad. Sci. U.S.A* **1958,** *44*, 1197-1202.

161. Kamiichi, K.; Doi, M.; Nabae, M.; Ishida, T.; Inoue, M. *J. Chem. Soc. Perkin Trans. 2* **1987**, 1739-1745.

162. Hisahiro, K.; Mariko, T.; Mitsunobo, D.; Toshimasa, I. *FEBS Letters* **1995,** *370*, 193-196.

163. Sherman, S. E.; Lippard, S. J. *Chem. Rev.* **1987,** *87*, 1153-1181.

164. Rochon, F. D.; Kong, P. C.; Coulombe, B.; Melanson, R. *Can. J. Chem.* **1980,** *58*, 381-386.

165. Ishida, T.; Doi, M.; Ueda, H.; Inoue, M.; Scheldrick, G. M. *J. Am. Chem. Soc.* **1988,** *110*, 2286-2294.

166. Grimme, S. *J. Comput. Chem.* **2006,** *27*, 1787-1799.

167. Vázquez-Mayagoitia, Á.; Sherrill, C. D.; Aprà, E.; Sumpter, B. G. *J. Chem. Theory Comput.* **2010,** *6*, 727-734.

168. Antony, J.; Grimme, S. *Phys. Chem. Chem. Phys.* **2006,** *8*, 5287-5293.

169. Hay, P. J.; Wadt, W. R. *J. Chem. Phys.* **1985,** *82*, 270-285.

170. Lu, T.; Chen, F. *J. Comput. Chem.* **2012,** *33*, 580-592.

171. Dapprich, S.; Frenking, G. *J. Phys. Chem.* **1995,** *99*, 9352-9362.

172. Dapprich, S.; Komáromi, I.; Byun, K. S.; Morokuma, K.; Frisch, M. J. *J. Mol. Struc. THEOCHEM* **1999,** *461–462*, 1-21.

173. York, D. M.; Lee, T.-S. *Multi-Scale Quantum Models for Biocatalysis: Modern Techniques and Applications* Springer: Heidelberg, 2009.

174. Stewart, J. P. *J. Mol. Model.* **2007,** *13*, 1173-1213.

175. Reed, A. E.; Curtiss, L.; Weinhold, F. *Chem.Rev.* **1988,** *88*, 899-926.

176. Bourbigot, S.; Ramalanjaona, N.; Boudier, C.; Salgado, G. F. J.; Roques, B. P.; Mély, Y.; Bouaziz, S.; Morellet, N. *J. Mol. Biol.* **2008,** *383*, 1112-1128.

177. Anzellotti, A. I.; Bayse, C. A.; Farrell, N. P. *Inorg. Chem.* **2008,** *47*, 10425-10431.

178. Fukui, K. *Angew. Chem. Int. Ed.* **1982,** *21*, 801-876.

179. Janiak, C. *J.Chem. Soc. Dalton Trans.* **2000**, 3885-3896.

180. Rutledge, L. R.; Campbell-Verduyn, L. S.; Hunter, K. C.; Wetmore, S. D. *J. Phys. Chem. B* **2006,** *110*, 19652-19663.

181. Tsipis, A. C.; Stalikas, A. V. *Inorg. Chem.* **2012,** *51*, 2541-2559.

182. Lehn, J.-M. *Supramolecular Chemistry Concepts and Perspectives*. Weinheim: New York, 1995.

183. Sponer, J.; Riley, K. E.; Hobza, P. *Phys. Chem. Chem. Phys.* **2008,** *10*, 2595-2610.

184. McGaughey, G. B.; Gagne, M.; Rappe, A. K. *J. Biol. Chem.* **1998,** *273*, 15458-15463.

185. Meyer, E. A.; Castellano, R. K.; Diederich, F. *Angew. Chem. Int. Ed.* **2003,** *42*, 1210-1250.

186. Hobza, P.; Sponer, J. *Chem. Rev.* **1999,** *99*, 3247-3276.

187. Claessens, C. G.; Stoddart, J. F. *J. Phys. Org. Chem.* **1997,** *10*, 254-272.

188. Schneider, H.-J. *Angew. Chem. Int. Ed.* **2009,** *48*, 3924-3977.

189. Anthony, J. E. *Chem. Rev.* **2006,** *106*, 5028-5048.

190. Pitoňák, M.; Neogrády, P.; Řezáč, J.; Jurečka, P.; Urban, M.; Hobza, P. *J. Chem. Theory Comput.* **2008,** *4*, 1829-1834.

191. Sinnokrot, M. O.; Sherrill, C. D. *J. Phys. Chem. A* **2006,** *110*, 10656 -10668.

192. Tsuzuki, S.; Honda, K.; Uchimaru, T.; Mikami, M.; Tanabe, K. *J. Am. Chem. Soc.* **2001,** *124*, 104-112.

193. Sinnokrot, M. O.; Valeev, E. F.; Sherill, C. D. *J. Am. Chem. Soc.* **2002,** *124*, 10887-10893.

194. Park, Y. C.; Lee, J. S. *J. Phys. Chem. A* **2006,** *110*, 5091-5095.

195. Hohenstein, E.; Sherrill, C. D. *J. Phys. Chem. A* **2009,** *113*, 878-886.

196. Czyżnikowska, Ż.; Zaleśny, R. *Biophys. Chem.* **2008,** *139*, 137-143.

197. Hobza, P.; Sponer, J. *J. Am. Chem. Soc.* **2002,** *124*, 11802-11808.

198. Hunter, C. A.; Saunders, j. K. M. *J. Am. Chem. Soc.* **1990**, 5525-5534.

199. Müller-Dethlefs, K.; Hobza, P. *Chem. Rev.* **2000,** *100*, 143-167.

200. Dunitz, J. D. *ChemBioChem* **2004,** *5*, 614-621.

201. Hobza, P.; Sponer, J.; Polasek, M. *J. Am. Chem. Soc.* **1995,** *117*, 792-798.

202. Hill, G.; Forde, G.; Hill, N.; Jr., W. A. L.; Sokalski, W. A.; Leszczynski, J. *Chem. Phys. Lett.* **2003,** *381*, 729-732.

203. Nakatani, K.; Matsuno, T.; Adachi, K.; Hagihara, S.; Saito, I. *J. Am. Chem. Soc.* **2001,** *123*, 5695-5702.

204. Kurita, Y.; Takayama, C.; Tanaka, S. *J. Comput. Chem.* **1994,** *15*, 1013-1018.

205. Schmidt, A.; Lindner, A.; Nieger, M.; Ruiz-Delgado, M. d. C.; Ramirez, F. J. *Org. Biomol. Chem.* **2006,** *4*, 3056-3066.

206. Kumar, N. S. S.; Gujrati, M. D.; Wilson, J. N. *Chem. Commun.* **2010,** *46*, 5464-5466.

207. Sini, G.; Sears, J. S.; Brédas, J.-L. *J. Chem. Theory Comput.* **2011,** *7*, 602-609.

208. Grimme, S. *Angew. Chem. Int. Ed.* **2008,** *47*, 3430-3434.

209. Zhao, Y.; Truhlar, D. *Theor. Chem. Acc.* **2008,** *120*, 215-241.

210. Hohenberg, P.; Kohn, W. *Phys. Rev. B.* **1964,** *136*, 864 - 871.

211. Heßelmann, A.; Jansen, G.; Schutz, M. *J. Chem. Phys.* **2005,** *122*, 014103-1 - 014103-17.

212. Werner, H.-J.; Knowles, P. J.; Knizia, G.; Manby, F. R.; Schütz, M.; Celani, P.; Korona, T.; Lindh, R.; Mitrushenkov, A.; Rauhut, G.; Shamasundar, K. R.; Adler, T. B.; Amos, R. D.; Bernhardsson, A.; Berning, A.; Cooper, D. L.; Deegan, M. J. O.; Dobbyn, A. J.; Eckert, F.; Goll, E.; Hampel, C.; Hesselmann, A.; Hetzer, G.; Hrenar, T.; Jansen, G.; Köppl, C.; Y. Liu; Lloyd, A. W.; Mata, R. A.; May, A. J.; McNicholas, S. J.; Meyer, W.; Mura, M. E.; Nicklaß, A.; O'Neill, D. P.; Palmieri, P.; Peng, D.; Pflüger, K.; Pitzer, R.; Reiher, M.; Shiozaki, T.; Stoll, H.; Stone, A. J.; Tarroni, R.; Thorsteinsson, T.; Wang, M. *MOLPRO, version 2010.1*, Cardiff, 2010.

213. Müller-Dethlefs, K.; Hobza, P. *Chem. Rev.* **1999,** *100*, 143-167.

214. Grover, R. J.; Walters, E. A.; Hui, E. T. *J. Phy. Chem.* **1987,** *91*, 3233-3237.

215. Krause, H.; Ernstberger, B.; Neusser, H. J. *Chem. Phys. Lett.* **1991,** *184*, 411-417.

216. Lee, E. C.; Kim, D.; Jurecka, P.; Hobza, P. T.; Kim, K. S. *J. Phys. Chem. A* **2007,** *111*, 3446-3457.

217. Arnstein, S. A.; Sherrill, C. D. *Phys. Chem. Chem. Phys.* **2008,** *10*, 2646-2655.

218. Albright, T. A.; Burdett, J. K.; Whangbo, M.-H. *Orbital Interactions in Chemistry.* John Wiley & Sons: Hoboken, 2013.

219. Parthasarathi, R.; Subramanian, V. *Struct. Chem.* **2005,** *16*, 243-255.

220. Johnson, E. R.; Keinan, S.; Mori-Sánchez, P.; Contreras-García, J.; Cohen, A. J.; Yang, W. *J. Am. Chem. Soc.* **2010,** *132*, 6498-6506.

221. Riley, K. E.; Pitoňák, M.; Jurečka, P.; Hobza, P. *Chem. Rev.* **2010,** *110*, 5023-5063.

222. Chalasinski, G.; Szczesniak, M. M. *Chem. Rev.* **1994,** *94*, 1723-1765.

223. Krishtal, A.; Vyboishchikov, S. F.; Van Alsenoy, C. *J. Chem. Theory Comput.* **2011,** *7*, 2049-2058.

224. Hobza, P.; Šponer, J. *J. Am. Chem. Soc.* **2002,** *124*, 11802-11808.

225. Sponer, J.; Leszczynski, J.; Hobza, P. *J. Phys. Chem.* **1996,** *100*, 5590-5596.

226. Amutha, R.; Subramanian, V.; Nair, B. U. *Theor. Chem. Acc.* **2002,** *107*, 343-350.

227. Di Felice, R.; Calzolari, A.; Molinari, E.; Garbesi, A. *Phys. Rev. B* **2001,** *65*, 045104-1 - 045104-10.

228. Lee, N. K.; Park, S.; Kim, S. K. *J. Chem. Phys.* **2002,** *116*, 7910-7917.

229. Tsuzuki, S. *Intermolecular Forces and Clusters* Springer Heidelberg, 2005; Vol. 115.

230. Tsuzuki, S.; Honda, K.; Uchimaru, T.; Mikami, M. *J. Chem. Phys.* **2004,** *120*, 647-659.

231. Yurtsever, E. *J. Phys. Chem. A* **2009,** *113*, 924-930.

232. Hohenstein, E. G.; Sherrill, C. D. *J. Chem. Phys.* **2010,** *132*, 184111-1 - 184111-10.

233. Kool, E. T.; Morales, J. C.; Guckian, K. M. *Angew. Chem. Int. Ed.* **2000,** *39*, 990-1009.

234. Hunter, C.; Lawson, K. R.; Perkins, J.; Urch, C. J. *J. Chem. Soc., Perkin Trans.* **2001,** *2*, 651-669.

235. Riley, K. E.; Hobza, P. *Acc. Chem. Res.* **2012,** *46*, 927-936.

236. Tiekink, E. R. T.; Zukerman-Schpector, J. *The Importance of Pi-Interactions in Crystal Engineering*. Wiley: Hoboken, 2012.

237. Kang, Y. K.; Iovine, P. M.; Therien, M. J. *Coord. Chem. Rev.* **2011,** *255*, 804-824.

238. Tewari, A. K.; Dubey, R. *Bioorg. Med. Chem.* **2008,** *16*, 126-143.

239. Dahl, T. *Acta Chem. Scand.* **1994,** *48*, 95-106.

240. Hobza, P.; Müller-Dethlefs, K. *Non-Covalent Interactions Theory and Experiment*. The Royal Society of Chemistry: Cambridge, 2010.

241. Podeszwa, R.; Bukowski, R.; Szalewicz, K. *J. Phys. Chem. A* **2006,** *110*, 10345-10354.

242. Lutz, P. B.; Bayse, C. A. *Phys. Chem. Chem. Phys.* **2013,** *15*, 9397-9406.

243. Berashevich, J.; Chakraborty, T. *Phys. Rev. B* **2011,** *84*, 033403-1 - 033403-4.

244. Sherrill, C. D.; Takatani, T.; Hohenstein, E. G. *J. Phys. Chem. A* **2009,** *113*, 10146-10159.

245. Lowdin, P.-O. *Adv. Quantum Chem.* **1970,** *5*, 185-199.

246. Pulay, P.; Baker, J.; Wolinski, K. *PQS version 3.3;* , Parallel Quantum Solutions; Fayetteville, 2007.

247. Lipkowitz, K. B.; Boyd, D. B. *Reviews in Computational Chemistry, Volume 5*. VCH Publishers Inc.: New York, 1994.

248. Lipkowitz, K. B.; Boyd, D. B. *Reviews In Computational Chemistry*. VCH Publishers, Inc: New York, 1994; Vol. 5.

249. Sanchez, G.; Espinosa, A.; Curiel, D.; Tarraga, A.; Molina, P. *J. Org. Chem.* **2013,** *78*, 9725-9737.

250. Weber, M.; Klein, J. E. M. N.; Miehlich, B.; Frey, W.; Peters, R. *Organometallics* **2013,** *32*, 5810-5817.

251. Jalbout, A. F.; Fernandez, S. *J. Mol. Struct.* **2002,** *584*, 169-182.

252. Everse, J. A. B. Y. K.-s. *The Pyridine Nucleotide Coenzymes*. Academic Press: New York, 1982.

253. Choudhury, R. R.; Chitra, R. *CrystEngComm.* **2010,** *12*, 2113-2121.

254. Ninković, D. B.; Andrić, J. M.; Zarić, S. D. *ChemPhysChem* **2013,** *14*, 237-243.

255. Stone, A. J. *The Theory of Intermolecular Forces*. Oxford University Press Inc.: New York, 1996.

256. Lide, D. R. *CRC Handbook of Chemistry and Physics*. 85 ed.; CRC press: Boca Raton, 2005.

257. Reyes, A.; Tlenkopatchev, M. A.; Fomina, L.; Guadarrama, P.; Fomine, S. *J. Phys. Chem. A* **2003,** *107*, 7027-7031.

258. Williams, J. H. *Acc. Chem. Res.* **1993,** *26*, 593-598.

259. Cabaço, M. I.; Tassaing, T.; Danten, Y.; Besnard, M. *Chem. Phys. Lett.* **2000,** *325*, 163-170.

260. Steed, J. M.; Dixon, T. A.; Klemperer, W. *J. Chem. Phys.* **1979,** *70*, 4940-4946.

261. Danten, Y.; Cabaço, M. I.; Tassaing, T.; Besnard, M. *J. Chem. Phys.* **2001,** *115*, 4239-4248.

262. Tsuzuki, S.; Uchimaru, T.; Mikami, M. *J. Phys. Chem. A* **2006,** *110*, 2027-2033.

263. Gung, B. W.; Amicangelo, J. C. *J. Org. Chem.* **2006,** *71*, 9261-9270.

264. Cabaço, M. I.; Danten, Y.; Besnard, M.; Guissani, Y.; Guillot, B. *J. Phys. Chem. B* **1998,** *102*, 10712-10723.

265. Reichenbacher, K.; Suss, H. I.; Hulliger, J. *Chem. Soc. Rev.* **2005,** *34*, 22-30.

266. Overell, J. S. W.; Pawley, G. S. *Acta Crystallogr. B* **1982,** *38*, 1966-1972.

VITA

PATRICIA LUTZ

EDUCATION

Ph.D., Old Dominion University, Chemistry & Biochemistry Department, 4541 Hampton Blvd. Norfolk, VA. 23529, Aug. 2014

B. S., Virginia Polytechnic Institute and State University, Blacksburg VA, May, 1977

PROFESSIONAL CHRONOLOGY

Chemistry 122 and 124 Lecture Teaching Assistant. (ODU) 08/2012 - Present

Chemistry 122 and 124 Laboratory Teaching Assistant. (ODU) 08/2009 - 08/2012

Honors Chemistry, AP Chemistry, Honors Physics, Atlantic Shores Christian School (ASCS). Chesapeake, VA. 08/2000 - 06/2009

AWARDS

Outstanding Teaching Assistant. (ODU) 2011-2012

Teacher of the Year awards (ASCS) 2001 - 2002 and 2005 - 2006

PUBLICATIONS

Lutz, P.B. and C.A. Bayse, Orbital-based insights into parallel-displaced and twisted conformations in π-π interactions. Phys. Chem. Chem. Phys., 2013. 15(23): p. 9397-9406.

Li, F.; Lutz, P. B.; Pepelyayeva, Y.; Arnér, E. S. J.; Bayse, C. A.; Rozovsky, S. Redox active motifs in selenoproteins *Proc. Natl. Acad. Sci. U.S.A* 2014. 111(19): p. 6976-6981.

POSTERS

"The role of orbital interaction in the geometric dependence of pi-pi stacking" Patricia Lutz and Craig Bayse, Research Symposium, William and Mary, March 25 (2011)

"DFT study on the pi-pi interactions between metalated guanine and the tryptophan of NCp7" P. B. Lutz and C. A. Bayse, Regional Meeting of ACS, Richmond, VA, Oct.(2011)

"Models of the inhibition of zinc-finger transcription factors by reducible organoselenium compounds" Patricia B. Lutz and Craig A. Bayse, The 244th ACS National Meeting, Philadelphia, PA, Aug. (2012)